

**ADVISORY GROUP FOR AEROSPACE RESEARCH & DEVELOPMENT**  
7 RUE ANCELLE, 92200 NEUILLY-SUR-SEINE, FRANCE

---

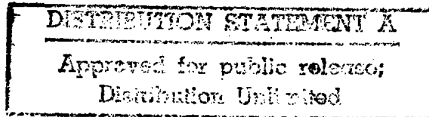
**AGARD ADVISORY REPORT 355**

**CFD Validation for Propulsion System  
Components**

(la Validation CFD des organes des propulseurs)

edited by

J. Dunham



19980715 034

Report of the Propulsion and Energetics Panel Working Group 26.

This Advisory Report was prepared at the request of the Propulsion and Energetics Panel of AGARD.



North Atlantic Treaty Organization  
*Organisation du Traité de l'Atlantique Nord*

---

# The Mission of AGARD\*

According to its Charter, the mission of AGARD is to bring together the leading personalities of the NATO nations in the fields of science and technology relating to aerospace for the following purposes:

- Recommending effective ways for the member nations to use their research and development capabilities for the common benefit of the NATO community;
- Providing scientific and technical advice and assistance to the Military Committee in the field of aerospace research and development (with particular regard to its military application);
- Continuously stimulating advances in the aerospace sciences relevant to strengthening the common defence posture;
- Improving the co-operation among member nations in aerospace research and development;
- Exchange of scientific and technical information;
- Providing assistance to member nations for the purpose of increasing their scientific and technical potential;
- Rendering scientific and technical assistance, as requested, to other NATO bodies and to member nations in connection with research and development problems in the aerospace field.

The highest authority within AGARD is the National Delegates Board consisting of officially appointed senior representatives from each member nation. The mission of AGARD is carried out through the Panels which are composed of experts appointed by the National Delegates, the Consultant and Exchange Programme and the Aerospace Applications Studies Programme. The results of AGARD work are reported to the member nations and the NATO Authorities through the AGARD series of publications of which this is one.

Participation in AGARD activities is by invitation only and is normally limited to citizens of the NATO nations.

\* AGARD merged with the Defence Research Group of NATO (DRG) on 1 January 1998 to form the Research and Technology Organization (RTO) of NATO. However, both AGARD and DRG will continue to issue publications under their own names in respect of work performed in 1997.

The content of this publication has been reproduced  
directly from material supplied by AGARD or the authors.



*Printed on recycled paper*

Published May 1998

Copyright © AGARD 1998  
All Rights Reserved

ISBN 92-836-1075-X



*Printed by Canada Communication Group Inc.  
(A St. Joseph Corporation Company)  
45 Sacré-Cœur Blvd., Hull (Québec), Canada K1A 0S7*

---

# **CFD Validation for Propulsion System Components**

## **(AGARD AR-355)**

### **Executive Summary**

The high performance of aircraft turbine engines - mainly oriented towards economy in civil engines and towards performance, economy and off-design reliability in military applications - depends on the correct design of gas flows in the engine. Today, this is mainly done by numerical computer simulation instead of the much more costly experimentation with hardware. The working group undertook to analyse the quality of computer codes in use and to show ways for improvement. Many discrepancies between codes were detected and it was recognized that even the researchers actively working in this field were unaware of the full scale of this phenomenon. The military will gain from the newly designed engines as well as from possible improvement in upgrades. It should be noted that this kind of down-to-earth analysis, despite its merits, has not been undertaken on an international basis outside AGARD/RTO.

# **La validation CFD des organes des propulseurs**

## **(AGARD AR-355)**

### **Synthèse**

La recherche de hautes performances des turbomoteurs, motivée, pour les moteurs civils, principalement par la recherche d'économies, et pour les moteurs militaires par l'amélioration des performances, les économies et la fiabilité dans des conditions hors tolérances, passe par une connaissance précise de la conception des écoulements dans le moteur.

Aujourd'hui, dans ce domaine il est fait appel en général, à la simulation numérique par ordinateur, de préférence à l'expérimentation réelle, beaucoup plus coûteuse. Le groupe de travail No. 26 s'est donné pour tâche d'analyser la qualité des codes machine utilisés et de faire des recommandations concernant d'éventuelles améliorations. Un nombre élevé de divergences entre les différents codes a été constaté et il a été admis que même les chercheurs impliqués activement dans ce domaine ignoraient la véritable ampleur du phénomène.

Les militaires pourront tirer profit des moteurs de nouvelle génération, ainsi que des améliorations possibles apportées par les remises à niveau. Il est à noter que malgré son mérite évident, ce type d'analyse pragmatique n'a pas été entrepris au niveau international en dehors de l'AGARD/RTO.

# Contents

	<b>Page</b>
<b>Executive Summary</b>	iii
<b>Synthèse</b>	iv
<b>Preface</b>	vi
<b>Abstract</b>	vii
<b>Recent publications of the Propulsion and Energetics Panel</b>	viii
<b>Introduction</b>	<b>1</b>
<b>1. Review of Turbomachinery CFD</b>	<b>3</b>
1.1    Introduction	3
1.2    Navier-Stokes equations for a rotating system	3
1.3    Mesh generation	3
1.4    Numerical schemes	4
1.5    Turbulence modelling	6
1.6    Code validation	9
<b>2. The Test Cases</b>	<b>11</b>
2.1    NASA Rotor 37	11
2.2    DLR cascade	16
<b>3. The Computations</b>	<b>27</b>
3.1    Introduction	27
3.2    The results for Rotor 37	27
3.3    The results for the DLR cascade	49
3.4    Analysis of the computational grids	58
3.5    Analysis of the algorithms	64
3.6    Analysis of the turbulence models	64
3.7    Convergence criteria	71
<b>4. Conclusions and recommendations</b>	<b>75</b>
4.1    Conclusions	75
4.2    Recommendations for research	77
4.3    Recommendations to PEP	77
<b>Appendix List of Working Group members and contributors</b>	<b>79</b>
<b>References</b>	<b>81</b>

## Preface

Computer codes which solve the Reynolds-averaged Navier-Stokes (RANS) equations are widely used by gas turbine and steam turbine manufacturers to analyse the aerodynamic performance of existing compressors and turbines and to design new ones. A wide range of computational fluid dynamics (CFD) approaches and turbulence models have been developed, and each code user validates his code using some relevant test cases. But the degree of validity of any code for application to a wider range of turbomachinery configurations than those initial test cases remains open to question. Experts in the field recognise the importance of using a "good" computational grid and a "good" turbulence model, but there is no consensus among them about which grids and which turbulence models are "good" enough to provide a reliable basis for design decisions.

The Propulsion and Energetics Panel set up Working Group 26 to help the international research community to clarify some of these issues, by comparing predictions (using as wide a range of methods as possible) of two representative but difficult test cases. The Group comprised experts in this field, both Panel members and non-members. Predictions were obtained from leading code developers and users, including some of the Group members, and compared with measurements of the two test cases in some detail by all of the members. The Group held meetings during 1994-6, and its members made additional contributions to the Technical Editor during 1997. This is its Report.

The Panel greatly appreciates the careful work of all those code developers and the Working Group members.

Dr J. Dunham  
Technical Editor

Dr G. Meauzé  
Chairman  
Propulsion and Energetics Panel  
Working Group 26

## **Summary**

Computer codes which solve the Reynolds-averaged Navier-Stokes equations are now used by manufacturers to design turbomachines, but there is no consensus about which grids and which turbulence models are good enough to provide a reliable basis for design decisions. The AGARD Propulsion and Energetics Panel set up Working Group 26 to help to clarify these issues, by analysing predictions (using as wide a range of codes as possible) of two representative but difficult single blade row test cases: NASA Rotor 37 and an annular turbine cascade tested by DLR. This report presents the Group's results and conclusions.

The predicted performance of both test cases fell short of the accuracy engine designers need. NASA discovered that the corner stall observed at the hub of Rotor 37 was affected by the presence of a small axial gap in the hub annulus line just upstream of the rotor, not modelled by the codes. The flow in the tip region also proved too difficult for most codes, which tended to overestimate the pressure losses there. The predicted pressure loss of the DLR cascade was up to 40% in error, and some codes were unable to predict correctly the highly three-dimensional secondary flow.

Recommendations are made about the type and density of grid, which depend on many factors. Mixing-length turbulence models are unsuitable for turbomachines with their complex endwall flows; some kind of turbulent transport model is essential. No turbulence model was found which always gave good loss predictions.

# **Recent Publications of the Propulsion and Energetics Panel**

## **CONFERENCE PROCEEDINGS (CP)**

**Advanced Instrumentation for Aero Engine Components**  
AGARD CP 399, November 1986

**Engine Response to Distorted Inflow Conditions**  
AGARD CP 400, March 1987

**Transonic and Supersonic Phenomena in Turbomachines**  
AGARD CP 401, March 1987

**Advanced Technology for Aero Engine Components**  
AGARD CP 421, September 1987

**Combustion and Fuels in Gas Turbine Engines**  
AGARD CP 422, June 1988

**Engine Condition Monitoring — Technology and Experience**  
AGARD CP 448, October 1988

**Application of Advanced Material for Turbomachinery and Rocket Propulsion**  
AGARD CP 449, March 1989

**Combustion Instabilities in Liquid-Fuelled Propulsion Systems**  
AGARD CP 450, April 1989

**Aircraft Fire Safety**  
AGARD CP 467, October 1989

**Unsteady Aerodynamic Phenomena in Turbomachines**  
AGARD CP 468, February 1990

**Secondary Flows in Turbomachines**  
AGARD CP 469, February 1990

**Hypersonic Combined Cycle Propulsion**  
AGARD CP 479, December 1990

**Low Temperature Environment Operations of Turboengines (Design and User's Problems)**  
AGARD CP 480, May 1991

**CFD Techniques for Propulsion Applications**  
AGARD CP 510, February 1992

**Insensitive Munitions**  
AGARD CP 511, July 1992

**Combat Aircraft Noise**  
AGARD CP 512, April 1992

**Airbreathing Propulsion for Missiles and Projectiles**  
AGARD CP 526, September 1992

**Heat Transfer and Cooling in Gas Turbines**  
AGARD CP 527, February 1993

**Fuels and Combustion Technology for Advanced Aircraft Engines**  
AGARD CP 536, September 1993

**Technology Requirements for Small Gas Turbines**  
AGARD CP 537, March 1994

**Erosion, Corrosion and Foreign Object Damage Effects in Gas Turbines**  
AGARD CP 558, February 1995

**Environmental Aspects of Rocket and Gun Propulsion**  
AGARD CP 559, February 1995

**Loss Mechanisms and Unsteady Flows in Turbomachines**  
AGARD CP 571, January 1996

**Advanced Aero-Engine Concepts and Controls**  
AGARD CP 572, June 1996

**Service Life of Solid Rocket Propellants**  
AGARD CP 586, May 1997

**Aircraft Fire Safety**  
AGARD CP 587, September 1997

**Future Aerospace Technology in the Service of the Alliance — Sustained Hypersonic Flight**  
AGARD CP 600, Volume 3, December 1997

## **ADVISORY REPORTS (AR)**

**Recommended Practices for Measurement of Gas Path Pressures and Temperatures for Performance Assessment of Aircraft Turbine Engines and Components (Results of Working Group 19)**  
AGARD AR 245, June 1990

**The Uniform Engine Test Programme (Results of Working Group 15)**  
AGARD AR 248, February 1990

**Test Cases for Computation of Internal Flows in Aero Engine Components (Results of Working Group 18)**  
AGARD AR 275, July 1990

**Test Cases for Engine Life Assessment Technology (Results of Working Group 20)**  
AGARD AR 308, September 1992

**Terminology and Assessment Methods of Solid Propellant Rocket Exhaust Signatures (Results of Working Group 21)**  
AGARD AR 287, February 1993

**Guide to the Measurement of the Transient Performance of Aircraft Turbine Engines and Components (Results of Working Group 23)**  
AGARD AR 320, March 1994

**Experimental and Analytical Methods for the Determination of Connected — Pipe Ramjet and Ducted Rocket Internal Performance (Results of Working Group 22)**  
AGARD AR 323, July 1994

**Recommended Practices for the Assessment of the Effects of Atmospheric Water Ingestion on the Performance and Operability of Gas Turbine Engines (Results of Working Group 24)**  
AGARD AR 332, September 1995

**Structural Assessment of Solid Propellant Grains (Results of Working Group 25)**  
AGARD AR 350, December 1997

## **LECTURE SERIES (LS)**

**Design Methods Used in Solid Rocket Motors**  
AGARD LS 150, April 1987  
AGARD LS 150 (Revised), April 1988

**Blading Design for Axial Turbomachines**  
AGARD LS 167, June 1989

**Comparative Engine Performance Measurements**  
AGARD LS 169, May 1990

**Combustion of Solid Propellants**  
AGARD LS 180, July 1991

**Steady and Transient Performance Prediction of Gas Turbine Engines**  
AGARD LS 183, May 1992

**Rocket Motor Plume Technology**  
AGARD LS 188, June 1993

**Research and Development of Ram/Scramjets and Turboramjets in Russia**  
AGARD LS 194, December 1993

**Turbomachinery Design Using CFD**  
AGARD LS 195, May 1994

**Mathematical Models of Gas Turbine Engines and their Components**  
AGARD LS 198, December 1994

## **AGARDOGRAPHS (AG)**

**Measurement Uncertainty within the Uniform Engine Test Programme**  
AGARD AG 307, May 1989

**Hazard Studies for Solid Propellant Rocket Motors**  
AGARD AG 316, September 1990

**Advanced Methods for Cascade Testing**  
AGARD AG 328, August 1993

## **REPORTS (R)**

**Application of Modified Loss and Deviation Correlations to Transonic Axial Compressors**  
AGARD R 745, June 1990

**Rotorcraft Drivetrain Life Safety and Reliability**  
AGARD R 775, June 1990

**Propulsion and Energy Issues for the 21st Century**  
AGARD R 824, March 1997

**Impact Study on the use of JET A Fuel in Military Aircraft during Operations in Europe**  
AGARD R 801, January 1997

**The Single Fuel Concept and Operation Desert Shield/Storm**  
AGARD R 810, January 1997 (*NATO Unclassified*)

## INTRODUCTION

Computational methods for the design and analysis of turbomachine flows have been developed and brought into use progressively over the last fifty years. The coming of large modern computers in recent years has allowed the practical development of codes which solve the Reynolds-averaged Navier-Stokes (RANS) equations in three dimensions. Such codes are already used by the large engine manufacturers for the advanced design of some engine components like compressors, turbines, air intakes, nozzles, and combustion chambers. Notable improvements have already been obtained; nevertheless the physical representation of real phenomena is not yet completely satisfactory, and only comparative predictions can be seriously considered.

Different computational fluid dynamics (CFD) approaches and turbulence models exist, and it seems essential today to establish their degree of validity for application to typical configurations in turbomachinery. Obviously, the different CFD code users make their own evaluation, but that remains limited. To make a real improvement in knowledge of the influence of the different elements of a CFD code (numerical algorithm, type and density of mesh, turbulence model, ...) on the results it is necessary to compare computations from different codes. This very important work can only be done in an international field; it fits AGARD's objectives perfectly.

PEP has regularly organised meetings, Lecture Series, or Working Groups on turbomachinery flow prediction methods. In 1976, Lecture Series 83 was held (Serovy, 1976), and also a Specialist Meeting in which predictions for a set of test cases were invited (AGARD, 1976). Subsequently, PEP-WG 12 was set up to review through-flow calculation methods, which reported in 1981 (Hirsch and Denton, 1981); it also employed test cases. In 1985, a Lecture Series on the emerging three-dimensional flow computation methods applied to turbomachines was presented (G.Meauzé, 1985). Following that, PEP-WG 18 was set up to assemble another new group of test cases, published in 1990 (Fottner, 1990). A Symposium on CFD techniques for propulsion applications was held by the Propulsion and Energetics Panel in Spring 1991 (AGARD, 1991). In his Technical Evaluation Report, Dr L.A.Povinelli recommended that a new activity should be started aimed at code validation. Other similar recommendations had also been made to the Panel, and following discussions, it was agreed to form Working Group 26: "CFD validation for propulsion system components". This was approved by the National Delegates' Board in Fall 1993, for starting in 1994. The topic falls within the specific recommendations of AGARD concerning improved engine design (flexibility), improved affordability, and improved hardware and software reliability.

A Lecture Series on turbomachinery CFD was held in 1994 (Hirsch, 1994).

Meanwhile, several experts had been consulted, and detailed plans about the Working Group discussed informally. Due to the scope of the work foreseen, it was agreed to limit the range of investigation to viscous three-dimensional steady and non-reacting flow configurations. Two representative turbomachinery configurations were chosen as test cases for the principal studies. Particular attention was given to the accuracy of the experimental results. In 1993, the Turbomachinery Committee of the International Gas Turbine Institute of the American Society of Mechanical Engineers (ASME) had issued an open invitation to predict the flow details of an isolated

transonic fan rotor, NASA Rotor 37. This proved a challenging case, so the WG decided to select it as one of the two cases; the other was an annular turbine cascade tested by the German Research Establishment DLR.

The objectives of the Working Group were to obtain CFD calculations of the specified flows, to evaluate the results and the methods used, for the purpose of advancing the technology. It was intended to study the effectiveness of the methods used in the various CFD codes, including grid geometry and type and the turbulence model, and to make recommendations for the guidance of code developers, and for future research.

Most of the test case activities have been led by experts from Government agencies and Universities. Codes are widely used by gas turbine and steam turbine manufacturers, but most aero engine firms have usually regarded their proprietary methods as too commercially sensitive to publish their predictions of test cases. In selecting which code to use, organisations have to consider several factors:

- (1) experience within the organisation of using the code;
- (2) how easy it is to use and how robust it is;
- (3) how well-supported it is by its originators or by in-house experts;
- (4) what computing facilities are needed and how long it takes to run; and
- (5) how accurately it predicts the aerodynamic performance of the turbomachine.

It is logical to expect that a balance must be found between these factors, depending on the particular circumstances of the organisation at the time. In this report, information about the computing requirements and time (factor 4) has been tabulated for the codes used, but not analysed; the focus is entirely on accuracy. So it was not intended to attempt to rank the specific codes in order of merit or to recommend to manufacturers a "best" code; indeed such a recommendation would probably be out-of-date by the time this report was printed.

The report has been written following detailed discussions by the Group. Each section was then drafted by one or two members, listed in an Appendix, but the final report represents the work and conclusions of all the members.

### **Acknowledgements**

The descriptions of the test cases in Chapter 2 and the experimental data from them were contributed for NASA by Dr A.J.Strazisar, and for DLR by Ms C.Langowsky.

In the text of the report, published papers are cited in the conventional way, as for example (Serovy, 1976), while specific contributions made for the Working Group by members or other research workers are cited without a date, as for example (Kang and Hirsch).

Grateful acknowledgement is made to the American Society of Mechanical Engineers for permission to reproduce the figures cited from ASME publications.

## Chapter 1

### REVIEW OF TURBOMACHINERY CFD

#### 1.1 INTRODUCTION

The development of numerical methods and computing facilities has led to the use of Computational Fluid Dynamics (CFD) as a current tool for designing components of turbine engines. Even if the experimental process still remains the final way to calibrate and validate an engine, CFD simulations allow a small number of configurations to be selected for all or part of the turbomachine in the design process. Different stages have been reached in the use of CFD: 3D steady turbulent calculations are performed daily, even if the physical models used today cannot reproduce faithfully all aspects of the real flow. Despite the differences which still exist between numerical simulations and reality, it is possible to predict many of the flow properties and the losses due to the non-isentropic features of the flow (shocks, viscous layers, tip clearance effects, passage vortices,...).

This chapter is a short presentation of the state-of-the-art of numerical methods used for solving compressible Navier-Stokes equations in turbomachinery applications. This review addresses specific features, as seen from the standpoint of turbomachinery flows, such as robustness and efficiency, space accuracy and time accuracy, grid density and grid regularity, numerical dissipation, turbulence model (including transition). This chapter is far from exhaustive, and the reader is referred to Hirsch (1994) for detailed presentations concerning turbomachinery design with CFD, and to Couaillier (1995) and to AGARD (1991) for a presentation of various CFD applications to turbomachinery flows. Other more recent references will be indicated as appropriate.

#### 1.2 NAVIER-STOKES EQUATIONS FOR A ROTATING SYSTEM

This section is devoted to the formulation of the Reynolds Averaged Navier-Stokes equations applied to turbomachinery flow calculations, the full 3D system written in a rotating frame of reference (see also Veuillot, 1990).

In order to formulate the equations in a rotating frame of reference, the definition of the relative time derivative is introduced. Considering a scalar function in space and time  $\Phi(M, t)$ , if the point M is fixed in a rotating wheel with a steady speed of rotation  $\bar{\Omega}$ , the following relationship exists between the absolute and relative time derivatives :

$$\left(\frac{\partial \Phi}{\partial t}\right)_A = \left(\frac{\partial \Phi}{\partial t}\right)_R - (\bar{\Omega} \cdot \vec{V}) \quad (1)$$

The relative time derivative  $(\partial / \partial t)_R$  is equal to zero for any time-steady scalar field in the rotating frame of reference. Consider now the time derivative of a vector expressed in the relative frame of reference. Denoting by  $q_\eta$  the coordinates of  $Q$  in the orthonormal rotating system of reference  $(e_\eta)$ , the following equation is obtained :

$$\left(\frac{\partial \vec{Q}}{\partial t}\right)_A = \left(\frac{\partial q_\eta}{\partial t}\right)_R \vec{e}_\eta - \vec{e}_\eta (\bar{\Omega} \cdot \vec{V}) q_\eta + \vec{u} \times \vec{Q} \quad (2)$$

The relative time derivative  $(\partial / \partial t)_R$  representing the first term on the right-hand-side of this equation is equal to zero for any stationary vector field in the rotating system of reference.

By using the relative time derivative definitions and by recalling that the absolute velocity  $\vec{V}$  and the relative velocity  $\vec{W}$  are related by:  $\vec{V} = \vec{W} + \bar{\Omega} \times \vec{r}$ ,  $\vec{r}$  being the radius, the Navier-Stokes equations can be written in a different form. In a first approach the governing equations for mass, momentum, and energy are written by using the relative time derivatives of the absolute variables :

$$\begin{aligned} \left(\frac{\partial p}{\partial t}\right)_R + \vec{V} [\rho \vec{V} \otimes \vec{W} - \bar{\sigma} - \bar{\tau}_t] &= 0 \\ \left(\frac{\partial \rho \vec{V}}{\partial t}\right)_R + \vec{V} [\rho \vec{V} \otimes \vec{W} - \bar{\sigma} - \bar{\tau}_t] &= -\rho (\bar{\Omega} \times \vec{V}) \quad (3) \\ \left(\frac{\partial \rho E}{\partial t}\right)_R + \vec{V} [\rho E \vec{W} - (\bar{\sigma} + \bar{\tau}_t) \cdot \vec{V} - \vec{q} - \vec{q}_t] &= 0 \end{aligned}$$

Another approach is to write the governing equations by using the relative time derivatives of the relative variables :

$$\begin{aligned} \left(\frac{\partial p}{\partial t}\right)_R + \vec{V} [\rho \vec{W} \otimes \vec{W} - \bar{\sigma} - \bar{\tau}_t] &= 0 \\ \left(\frac{\partial \rho \vec{W}}{\partial t}\right)_R + \vec{V} [\rho \vec{W} \otimes \vec{W} - \bar{\sigma} - \bar{\tau}_t] &= \rho (\bar{\Omega}^2 \vec{r} - 2 \bar{\Omega} \times \vec{W}) \quad (4) \\ \left(\frac{\partial \rho E_R}{\partial t}\right)_R + \vec{V} [\rho E_R \vec{W} + (\bar{\sigma} + \bar{\tau}_t) \cdot \vec{W} - \vec{q} - \vec{q}_t] &= \rho \bar{\Omega}^2 \vec{r} \cdot \vec{W} \end{aligned}$$

The stress tensor  $\bar{\sigma} = -p \bar{I} + \bar{\tau}$ , where  $\bar{\tau}$  is the shear stress tensor and  $p$  the static pressure, is not affected by the rotation (which is a solid body motion). In system (4), as opposed to system (3), the fluxes are formally identical to those of the Navier-Stokes equations written in an absolute frame of reference. Nevertheless the discretisation of the source terms in system (4) introduces more approximation errors than the discretisation of the source terms in system (3).

The expression of the relative specific energy conservation in system (4), obtained from system (3) by combining the energy equation with the continuity equation and the momentum equation, can also be written in the following conservative form :

$$\left(\frac{\partial \rho E^*}{\partial t}\right)_R + \text{div} [\rho I \vec{W} - (\bar{\tau} + \bar{\tau}_t) \cdot \vec{W} - \vec{q} - \vec{q}_t] = 0 \quad (5)$$

In equation (5), where the quantity  $E^*$  is equal to  $E_R - 1/2 (\bar{\Omega} \times \vec{r})^2$ ,  $E_R$  being the relative energy ( $C_v T_t$ ), it is seen that the rothalpy  $I$  is constant along a streamline of an inviscid rotating steady flow.

#### 1.3 MESH GENERATION

The generation of the computational mesh is certainly today one of the most important requirements to obtain reliable numerical solutions for turbomachinery configurations. It is necessary to deal with various geometries: axial or centrifugal machines, blades with thick leading or trailing edges, highly cambered turbines, tip clearance representation, rotor/stator interaction, etc. The improvements in this area over the last ten years since the beginning of 3D calculations are very important. A large variety of mesh choices have been proposed, from a simple mono-block C-grid around the blade

to a complex hybrid multidomain mesh. Nevertheless, it has to be noted that generally the 3D meshes are built from a stacking of 2D blade-to-blade meshes. Moreover, due to complex geometries and also to sophisticated turbulence models, an increasing number of mesh strategies take into account adaptive refinement. This variety of approaches corresponds to different levels of mesh generation, and also to different levels of numerical methods in terms of data structure management. By considering some typical examples, a short review of the main mesh generation strategies is presented now.

### 1.3.1 Monodomain structured meshes

With a mono-domain approach, three types of grid can be considered. An H-grid is well suited to applied far-field and periodicity conditions and is generally easy to set up, but is often highly skewed near the leading and trailing edges of the blades. A C-grid provides a good resolution around the leading edge and in the wake, but becomes skewed at the inflow and at the periodic boundaries. An O-grid allows good resolution of both leading and trailing edges, but induces skewness at inflow, outflow and periodic boundaries.

### 1.3.2 Multidomain structured meshes

A first approach used to remove the drawbacks at the periodic boundary consists of using non-periodic grids (see for instance Veuillot (1985) and Arnone (1993)). A more general technique is based on a structured multidomain approach, which keeps the advantages and removes the drawbacks of the single grids. A large number of solvers use such a technique today, with the capability to use overlapping meshes. However, care must be taken to ensure that the grids are smooth across the block interfaces.

The five-domain mesh presented by Heider (1993) for a highly cambered turbine with a tip clearance gap shows the advantages of such an approach: for each blade-to-blade section an O-mesh is used around the blade and H-meshes are used upstream and downstream of the blade, providing a good quality of mesh everywhere. In the clearance an H-O decomposition allows a good regularity to be achieved in the radial direction. Choi (1993) and Fougères (1994) used a multidomain technique with or without overlapping for meshing the holes in a film cooling configuration. This type of approach allows a good discretisation of the viscous layer and of the hole too, in order to capture accurately the flow interaction. Madavan et al (1993) use multidomain overlapping grids for a turbine rotor-stator interaction.

### 1.3.3 Unstructured meshes

The use of an unstructured tetrahedra approach leads to a greater flexibility in the mesh generation process. Moreover, even if a multidomain approach with overlapping grids or/and chimera grids allows local refinement, unstructured methods seem to be more appropriate. Nevertheless, unstructured solvers are still today less efficient in CPU time than structured solvers, and the implementation of algebraic turbulence models leads to serious difficulties. 2D Euler cascade flows (Bassi, 1991) and 3D Euler rotor/stator interactions (Trépanier, 1993) have been performed with adaptative unstructured meshes (see also Kwon (1993) for 3D unstructured Euler calculations on turbine blades). Dawes (1992, 1993) presents complex 3D turbulent calculations for different turbomachinery configurations with adaptative mesh refinement. In particular, a very accurate shock/boundary layer interaction can be represented after different levels of refinement starting from a coarse grid. However, tetrahedral

meshes are less tolerant of the high cell aspect ratios which generally occur near solid boundaries.

### 1.3.4 Hybrid structured/unstructured meshes

The hybrid approach, which combines structured and unstructured meshes (and solvers) is a way to make the best of both approaches. For example, hybrid calculations have been used by Nakahashi (1987) for 2D and 3D Navier-Stokes turbine cascade simulations, and also by Mathur (1993) for 2D unsteady Navier-Stokes rotor/stator interaction. In both cases, the authors use a structured approach around the blade to get a regular and orthogonal mesh in the boundary layer, and an unstructured mesh in the outer part which allows a good mesh quality to be generated in the far field and near the periodic boundary. Care must again be taken at the interfaces.

## 1.4 NUMERICAL SCHEMES

The numerical schemes used for solving the Euler or the Navier-Stokes equations for turbomachinery flow simulations do not differ from those used for other applications. As is well-known, a large variety of numerical schemes have been developed within the CFD community, and it is very difficult to list them exhaustively. Therefore, this section gives a short summary of the most popular of them for turbomachinery applications. For a detailed review of numerical schemes used in fluid dynamics, refer to Hirsch (1988, 1990).

Most of the computations performed up to now assume steady flow, and most of the methods used for these calculations rely on an unsteady or pseudo-unsteady approach. In such approaches, different combinations of space discretisation (centred, upwind) and time discretisation (explicit, implicit) exist, sometimes based on a coupling between space and time and sometimes not, which may use convergence acceleration techniques. However, some methods will also be mentioned for solving the equations written in steady formulation.

### 1.4.1 Space discretisation

The discretisation of the gradients is mainly performed through finite volume methods or finite difference methods on structured meshes. However, on structured, unstructured or hybrid meshes, finite volume methods and finite element methods have been used (Holmes, 1988 and Ivanov, 1993). Because of the importance of mass flow conservation in turbomachinery applications, finite volume methods are generally preferred.

#### 1.4.1.1 Space Centred Schemes

The Lax-Wendroff scheme (Lax, 1964) is based on a Taylor expansion of second order in time, where the time derivatives are replaced by 3-point space-centred derivatives for the Euler equations. Several extensions of this scheme have been done in multi-space-dimensions, for the Euler and the Navier-Stokes equations, differing by their non-linear properties and their grid dependence. For more details concerning these properties, see the complete study by Lerat (1979).

One original formulation of the Lax-Wendroff scheme associated with an efficient multigrid method has been proposed by Ni for Euler and Navier-Stokes turbomachinery simulation (Ni, 1982, Davis, 1987), and used by several authors (see for instance Giles (1988), Cambier (1988), and Heider (1993)). This formulation is very easy to implement but does not preserve the good numerical properties of the original Lax-Wendroff scheme extended on a curvilinear mesh by Lera (1979).

The MacCormack scheme (MacCormack, 1969), which is also second order accurate in space and time, is based on a predictor-corrector approach of the Lax-Wendroff type, allowing the calculation of the Jacobian matrix for the evaluation of the second order term to be removed. It has been extensively applied to different external and internal configurations. For turbomachinery flow simulations, see for instance the various single and multistage configurations detailed by Veuillot (1985) and Fourmaux (1987), and more recently it has been used for a coupled unsteady inviscid/boundary layer calculation by Tran (1992).

It must be noted that in the above schemes coupling space and time discretisations (for such types of scheme see also Denton, 1982), the numerical solution of a steady-state problem is not independent of the time-step used to reach this steady state, which can be seen as a drawback or as an advantage to build Lax-Wendroff schemes without need of artificial viscosity (Lerat, 1988).

The other important class of space centred scheme, used in particular for turbomachinery applications, is based on the scheme proposed originally by Jameson et al (1981), built on a simple centred discretisation of the physical flux completed by a non-linear second order dissipation accompanied by a linear fourth order dissipation. Different versions of this scheme, which is in fact the most popular scheme used in the CFD community, have been implemented in 3D codes using a node centred approach (Chima, 1991, Dawes, 1992) or a cell centred approach (Arnone, 1993, Calvert, 1997, Dawes, 1986, Jennions, 1993, Kang, 1993, Liu 1993, McNulty, 1994, Vuillot, 1993, Shabbir, 1996, and Zimmermann, 1992), with various implementations of the original numerical dissipation adapted to the type of mesh.

#### 1.4.1.2 Upwind schemes

The centred discretisations require the addition of non-linear numerical dissipation to remove oscillations near the shocks, and can also require the addition of linear numerical dissipation to ensure the stability of the scheme. On the other hand, the upwind approach uses directly the information linked to the hyperbolic nature of the Euler equations which is propagated along the characteristic lines. This upwind approach, which is certainly sounder theoretically than the centred approach, has generated different classes of scheme.

Godunov's method considers a piecewise-constant approximation of the field in each cell, associated with the resolution of a Riemann problem at each interface. Ivanov et al (1993), for turbomachinery applications, use a piecewise cubic distribution in each cell, leading to a third order scheme.

Schemes based on Flux Vector Splitting (Steger, 1981, Van Leer, 1982), Flux Difference Splitting (Roe, 1981, Osher, 1982), and Total Variation Diminishing (Harten, 1983, Yee, 1987) have been constructed with different space order approximations. Various turbomachinery applications have been performed with such schemes, for instance by Allmaras (1992), Benetschik (1992), Chen (1993), Dorney (1991), Engel (1994), and Madavan (1989, 1993).

#### 1.4.2 Other schemes

Some authors use the steady formulation of the governing equations to solve steady problems. Patankar and Spalding (1972) introduced a pressure correction method for solving the incompressible equations, extended by Hah (1984, 1992) for the simulation of 3D viscous compressible and transonic

flows in turbomachinery configurations. Another example of such a scheme based on a steady approach is that described by Moore and Moore (1991) for the calculation of the flow through a turbine with tip clearance.

#### 1.4.3 Time Discretisation

The time discretisation methods used to solve the Euler/Navier-Stokes equations can be split into two classes: coupled space-time methods, like the Lax-Wendroff or MacCormack schemes, and separate space and time methods. For the methods belonging to the second class, the time integration is commonly performed by using a Runge-Kutta approach. This Runge-Kutta time integration was first used for the solution of Euler equations by Jameson et al (1981), associated with a space centred discretisation, but it is also used with upwind space discretisation. All these schemes were initially developed in an explicit approach, and for turbomachinery simulations some examples of 2D or 3D calculations have been presented by Engel (1994), Couaillier (1991), Denton (1982), and Kunz (1992).

For steady state problems based on unsteady approaches, implicit schemes allowing the use of large time steps can be very efficient for reaching the converged solution rapidly. To remove the time step limitation of the explicit schemes corresponding to a condition on the Courant-Friedrichs-Lowy (CFL) number, various studies have been performed since the contribution of Beam and Warming (1978). For the Lax-Wendroff scheme, Lerat (1982) proposed implicit methods with ADI approaches using a block technique or a spectral radius technique, leading to an unconditionally stable second order scheme for a linear problem. This spectral radius technique, which simply requires the resolution of a tridiagonal system, has been coupled with Ni's scheme (see for instance Heider, 1993), and has also been coupled by Jameson (1985) to the Runge-Kutta scheme. This approach, which is well-known as Implicit Residual Smoothing (IRS), has been widely used for ten years, for either steady or unsteady problems, on structured meshes (see for instance Chima, 1993, Arnone, 1993, and Liamis, 1994), and also adapted for unstructured meshes with an unfactored approach (Dawes, 1992).

Rai et al. (1989) presented a third order space accurate upwind scheme associated with a fully implicit algorithm, solved by a subiteration procedure for the simulation of unsteady viscous flow (see also Madavan, 1993). In this scheme, factorisation and linearisation errors can be driven to zero at each time step. Such types of subiteration procedure associated with upwind schemes are presented, for instance, by Benetschick (1992) for steady simulations and by Furukawa (1992) for unsteady simulations.

#### 1.4.4 Acceleration methods

Different techniques can be used to accelerate the convergence to steady state, such as local time-stepping and implicit residual smoothing. Implicit methods aim to reduce the computational costs.

Perhaps the most effective technique leading to convergence acceleration is based on the use of multigrid methods. The multigrid methods consist of transferring residuals on to coarse grids, solving the modified system on these grids, and interpolating the new residual back to the fine grid. They have the property of smoothing the long wave errors much faster than by using only the fine grid. These methods were first developed at the beginning of the 1970s for the solution of elliptic problems, and were later extended to the solution

of Euler and Navier-Stokes time-dependent problems by Ni (1982) and Davis (1987), associated with the Lax-Wendroff scheme, and by Jameson et al (1985) associated with the space-centred Runge-Kutta scheme. Jameson's multigrid technique combined with the IRS stage enables very efficient solvers to be written, as for instance by Arnone (1993), where a 3D Navier-Stokes calculation on a 380,000 mesh point grid is presented. This calculation achieves a five order decrease of the residuals after 200 cycles, corresponding to 45 minutes on a CRAY-YMP.

### 1.5 TURBULENCE MODELLING

In order to close the Reynolds-averaged Navier-Stokes model (RANS) formulated with the system of equations (3) and (4), it is necessary to model the Reynolds stress  $\bar{\tau}_t$ , and the turbulent heat flux  $\bar{q}_t$ . There exist two broad classes of turbulence model, used at the engineering level.

The first one, representing most of the turbulence models used in practice, is defined by the eddy viscosity concept. With an eddy-viscosity concept, also called the Boussinesq hypothesis, the tensor  $\bar{\tau}_t$ , and the flux  $\bar{q}_t$ , are expressed by relations analogous to those existing for the laminar tensor  $\bar{\tau}$  and heat flux  $\bar{q}$ :

$$\begin{aligned}\bar{\tau}_t &= -2/3(\rho k + \mu_t \bar{V} \cdot \bar{V})\bar{I} + 2\mu_t \bar{D} \\ \bar{q}_t &= -C_p \mu_t / Pr_t \bar{V} T\end{aligned}$$

The modelling problem is thereby reduced to the determination of two scalar quantities, the turbulent viscosity  $\mu_t$ , and the turbulent kinetic energy  $k$ . Among the models adopting the Boussinesq hypothesis, there are at least two distinct categories:

The first approach consists of algebraic turbulence models, in which eddy viscosity is expressed directly from the characteristic properties of the boundary layer by considering the local equilibrium of turbulence (production=dissipation). In this approach, the turbulent kinetic energy is generally assumed to be zero, since it cannot be correctly estimated.

The second approach is transport equation models, where the eddy viscosity is generally related to the turbulent kinetic energy and to a characteristic length scale of turbulence, expressed in terms of the local turbulent quantities.

The second class of turbulence model, based on Reynolds Stress Models and Algebraic Stress Models, does not use the Boussinesq hypothesis. Whereas the RSM models solve a transport equation for each of the stresses, the ASM Models use only two transport equations, completed by algebraic relations for the Reynolds stresses. Very few turbomachinery simulations have been performed up to now with RSM or ASM models. For example, see the 3D calculations performed by Hah (1984) with an ASM model associated with wall functions for various conditions in a turbine blade configuration. No model belonging to this class has been used in the WG26 calculations.

Blade surface boundary layers undergo transition from the laminar to the turbulent state, in some cases by "natural transition", and in some cases before a separated laminar boundary layer reattaches (after a "transition bubble"). It is also possible for turbulent boundary layers to revert to a laminar state in a strong favourable pressure gradient. The prediction of these effects is critical to the accurate estimation of surface heat transfer, and in some cases it is also important to loss prediction.

In a turbomachine, rapid transition has been shown to be forced in some cases by the impact of a shock wave or a wake arriving from an upstream blade row, followed by reversion to the laminar state when the disturbance has passed. Transition is known to depend on the free stream turbulence and also on the roughness of the surface. So it is not surprising that there is as yet no generally accepted way of predicting transition within a RANS computation, although some of the turbulence models used include a way of estimating where transition is likely to occur. Mayle (1997) has recently summarised transition prediction methods for two-dimensional boundary layers, but three-dimensional transition is obviously more difficult to predict.

Almost all the computations undertaken for the WG have assumed the blade surface boundary layers to be fully turbulent from the leading edge. This assumption is believed to be adequate for the test cases chosen by the WG, but in general it is likely to be a significant limitation.

#### 1.5.1 Mixing-length algebraic models

a) Most of the Navier-Stokes simulations for turbomachinery are still carried out with simple algebraic turbulence models. The most popular of them is the Baldwin-Lomax model (Baldwin, 1978) derived from the Cebeci-Smith model (Cebeci, 1974), and a large number of turbomachinery computations have been done with it (see for instance Chima, 1993, Davis, 1987, Engel, 1994, Liu, 1988, Nakahashi, 1987, and Scott, 1986).

This model considers the boundary layer split into two parts: an inner region denoted by the subscript  $i$  and the outer region denoted by the subscript  $e$ . The turbulent viscosity  $\mu_t$  is defined as follows:

$$\mu_t = \mu_{ti} \text{ if } d \leq d_0 \text{ and } \mu_t = \mu_{te} \text{ if } d \geq d_0$$

where  $d$  is the distance to the wall and  $d_0$  is determined as the smallest value of  $d$  for which  $\mu_{ti} = \mu_{te}$ .

In the inner region the mixing length is defined by:  $I = Kd$ , where  $K = 0.41$  is the Von Karman constant. The eddy viscosity  $\mu_{ti}$  is then given by the relation:  $\mu_{ti} = \rho l^2 D^2 |\omega|$ , where  $\omega$  is the vorticity. The damping function  $D$  is defined as follows:

$$D(d) = 1 - \exp(-d^+ / A^+)$$

where  $A^+ = 26$ . The non-dimensional distance  $d^+$  is defined using the skin velocity  $V_t (\tau_w = \rho_w V_t^2)$  and the density at the wall  $\rho_w$  and molecular viscosity  $\mu_w$ :  $d^+ = \rho_w V_t d / \mu_w$ .

In the outer region, the eddy viscosity  $\mu_{te}$  is given by the relation:

$$\mu_{te} = C_i C_{cp} \rho F_{wake} F_{Kleb}(d)$$

where  $C_i = 0.0168$  and  $C_{cp} = 1.6$ . The quantity  $F_{wake}$  is defined as follows:

$$F_{wake} = d_{max} \min(F_{max}; C_{wk} V_m^2 / F_{max})$$

where  $C_{wk}$  was originally given the value 0.25,  $d_{max}$  is the value where the function  $F(d) = d \cdot D(d) \cdot \omega$  attains its maximum value  $F_{max}$ , and where  $V_m$  denotes the difference between the maximum and the minimum velocity inside the shear layer. The Klebanoff intermittency factor  $F_{Kleb}$  is defined by:

$$F_{Kleb} = \left[ 1 + 5.5(C_{Kleb} d / d_{max})^6 \right]^{-1}$$

with  $C_{Kleb} = 0.3$ .

b) In the model of Michel et al (1969), the turbulent viscosity  $\mu_t$  is obtained as follows :

$$\mu_t = \rho l^2 F^2 |\bar{\omega}|, \text{ where } l = 0.085 \delta \tanh(Kd / 0.085\delta).$$

where  $F$  is the Van Driest viscous sublayer damping function given by :

$$F(\xi) = 1 - \exp(-\sqrt{\xi} / 26K), \text{ where } \xi = \rho l^2 (\mu + \mu_t) / \mu^2 |\bar{\omega}|.$$

These relations lead to an implicit equation for  $\mu_t$ , which is solved by Newton's method. The quantities  $d$  and  $\delta$  are respectively the distance to the wall and the boundary layer thickness.

Theoretical and practical difficulties appear when implementing these models in the presence of several walls, where corner flows exist. In that case, if the quantity  $d$  can be relatively easily defined for both models, the evaluation of the quantities  $d_{max}$  and  $F_{max}$  for the Baldwin-Lomax model and  $\delta$  for the Michel model causes great difficulties.

### 1.5.2 One-equation Spalart-Allmaras model

Recently there has been significant interest in one equation transport models as a way of obtaining the advantages of a transport model at a minimum computational cost. Perhaps the most popular at present is the Spalart-Allmaras model (Spalart and Allmaras, 1992, 1994) which solves an equation for the high Reynolds number eddy viscosity  $\tilde{v}$  written in the following form :

$$\frac{D\tilde{v}}{Dt} = C_{b1} [1 - f_{12}] \tilde{S}\tilde{v} + \frac{1}{\sigma} [\nabla \cdot ((v + \tilde{v}) \nabla \tilde{v}) + C_{b2} (\nabla \tilde{v})^2] - \left[ C_{w1} f_w - \frac{C_{b1}}{K^2} f_{12} \right] \left[ \frac{\tilde{v}}{d} \right]^2 + f_{11} \Delta U^2$$

where the turbulent kinematic viscosity  $v_t$  is given by

$$v_t = \tilde{v} f_{v1}, \text{ where } f_{v1} = \frac{\chi^3}{\chi^3 + C_{v1}^3} \text{ with } \chi = \frac{\tilde{v}}{v},$$

$$\tilde{S} = S + \frac{\tilde{v}}{K^2 d^2} f_{v2} \quad \text{where } S \text{ is the vorticity,}$$

$$f_{v2} = 1 - \frac{\chi}{1 + \chi f_{v1}},$$

$$f_w = g \left[ \frac{1 + C_{w3}^6}{g^6 + C_{w3}^6} \right], \quad g = r + C_{w2} (r^6 - r), \quad r = \frac{\tilde{v}}{SK^2 d^2}$$

$$f_{12} = C_{13} \exp(-C_{14} \chi^2)$$

$$f_{11} = C_{11} g_t \exp(-C_{12} \frac{w_t^2}{\Delta U^2}) \left[ d^2 + g_t^2 d_t^2 \right]$$

$$g_t = \min(0.1, \Delta U / w_t, \Delta x_t)$$

$$\Delta x_t = \text{grid spacing along the wall}$$

$$\text{at the nominated transition point}$$

$$d_t = \text{distance between the local point and the transition point}$$

$$w_t = \text{vorticity at the wall at the nominated transition point}$$

$$\text{values of constants:}$$

$$C_{b1} = 0.1355, \sigma = 2/3, C_{b2} = 0.622, K = 0.41$$

$$C_{w1} = C_{b1} / K + (1 + C_{b2}) / \sigma, C_{w2} = 0.3, C_{w3} = 2$$

$$C_{v1} = 7.1, C_{11} = 1, C_{12} = 2, C_{13} = 1.1, C_{14} = 2$$

(In Spalart and Allmaras (1994),  $C_{13} = 1.2, C_{14} = 0.5$ .)

The boundary condition on the wall is expressed by setting  $\tilde{v} = 0$ .

### 1.5.3 Two-equation turbulence models

Because they provide a good compromise between accuracy and computational cost, the use of turbulence models with two transport equations for turbomachinery applications has been increasing for several years. Examples of these models are the Jones-Launder k- $\epsilon$  model (Jones, 1973), the Wilcox k- $\omega$  model, the Wilcox-Rubesin k- $\omega^2$  model (Wilcox and Rubesin, 1980, Wilcox, 1991) and the Coakley q- $\omega$  model (Coakley, 1983). The low-Reynolds-number Jones-Launder model and Wilcox model, which are in fact popular two-equation models, are presented hereafter. For these two models, the low Reynolds number closure coefficients do not depend on geometrical quantities, such as the reduced wall distance  $y^+$  depending on the wall distance and on the friction velocity inaccurately defined in separation zones, but instead the damping functions are based on the turbulent Reynolds number  $Re_t$ , only depending on local flow quantities:

$$Re_t = \frac{\rho k^2}{\mu \epsilon} = \frac{\rho k}{\mu \omega}$$

(Note that this equation defines the symbol  $\omega$ , which is not the same as the vorticity  $\bar{\omega}$  used in Section 1.5.1.) Hence, from a practical point of view, these two-equation models are well-suited for complex three-dimensional configurations. However, there can be numerical difficulties associated with solving two-equation models with explicit schemes due to the stiffness of the equation system (Dailey et al, 1994).

a) The equations of the k- $\epsilon$  system can be written as follows :

$$\begin{aligned} \frac{\partial \rho k}{\partial t} + \bar{\nabla} \cdot (\rho k \bar{V}) &= \bar{\nabla} \cdot \left[ \left( \mu + \frac{\mu_t}{\alpha_k} \right) \bar{\nabla} k \right] + \bar{\tau}_t : \bar{\nabla} \bar{V} - \rho \epsilon - D \\ \frac{\partial \rho \epsilon}{\partial t} + \bar{\nabla} \cdot (\rho \bar{V} \epsilon) &= \bar{\nabla} \cdot \left[ \left( \mu + \frac{\mu_t}{\alpha_\epsilon} \right) \bar{\nabla} \epsilon \right] + C_1 f_1 \frac{\epsilon}{k} \bar{\tau}_t : \bar{\nabla} \bar{V} \\ &\quad - C_2 f_2 \frac{\epsilon^2}{k} + E \end{aligned}$$

In these equations,  $D$  is a wall term and  $E$  is a low Reynolds term introduced to solve the k- $\epsilon$  system in the region down to the wall with low turbulent Reynolds number ( $Re_t \leq 100$ ). The turbulent viscosity is evaluated by the relation:  $\mu_t = c_\mu f_\mu \rho k^2 / \mu \epsilon$ . Some examples of the terms  $E, f_\mu, f_1$  and  $f_2$ , including empirical constants and damping functions, were presented by Patel (1984). The Jones-Launder model is based on the following definitions :

$$D = 2\mu (\bar{\nabla} \sqrt{k})^2, \quad E = 2 \frac{\mu \mu_t}{\rho} \left( \frac{\partial V_t}{\partial n^2} \right)^2$$

$$\alpha_k = 1, \alpha_\epsilon = 1.3, C_1 = 1.57, C_2 = 2,$$

$$f_1 = 1, f_2 = [1 - 0.3 \exp(-Re_t^2)],$$

$$f_\mu = \exp \left( \frac{-2.5}{1 + Re_t / 50} \right), C_\mu = 0.09$$

The boundary condition on the wall is expressed by setting  $k=0$  and  $\epsilon=0$ .

b) The equations of the k- $\omega$  system can be written as follows :

$$\frac{\partial \rho k}{\partial t} + \bar{\nabla} \cdot (\rho \bar{V} k) = \bar{\nabla} \cdot \left[ \left( \mu + \sigma^* \mu_t \right) \bar{\nabla} k \right] + \bar{\tau}_t : \bar{\nabla} \bar{V} - \beta^* \rho k \omega$$

$$\frac{\partial \rho \omega}{\partial t} + \bar{\nabla} \cdot (\rho \bar{V} \omega) = \bar{\nabla} \cdot \left[ \left( \mu + \sigma \mu_t \right) \bar{\nabla} \omega \right] + \alpha \frac{\omega}{k} \bar{\tau}_t : \bar{\nabla} \bar{V} - \beta \rho \omega^2$$

The turbulent viscosity is evaluated by the relation:  $\mu_t = \alpha^* \rho k / \omega$ . The parameters  $\alpha, \alpha^*, \beta, \beta^*, \sigma, \sigma^*$  in the

above equations are the closure coefficients of the model and, according to Wilcox (1994), are given by :

$$\alpha = \alpha_0 \frac{\alpha_0 + Re_t / R_\omega}{1 + Re_t / R_\omega} (\alpha^*)^{-1}, \quad \alpha^* = \alpha_0 \frac{\alpha_0 + Re_t / R_k}{1 + Re_t / R_k}$$

$$\beta = \beta_t, \quad \beta^* = \beta_t \frac{\beta_0^* + (Re_t / R_\beta)^4}{1 + (Re_t / R_\beta)^4}$$

$$\sigma = \sigma^* = 1/2,$$

$$\alpha_0 = 1/10, \alpha_0^* = \beta_t / 3, \beta_0^* = 5/18,$$

$$\alpha_t = 5/9, \alpha_t^* = 1, \beta_t = 3/40, \beta_t^* = 9/100,$$

$$R_\beta = 8, R_k = 6, R_\omega = 2.7.$$

At solid walls,  $k=0$  and

$$\omega = \frac{u_t^2}{v} S_R \quad \text{where } u_t = \text{friction velocity} = \sqrt{\frac{\tau_w}{\rho}}$$

$S_R$  is related to the non-dimensional surface roughness

$$k_R^+ = \frac{k_R u_t}{v} \text{ through the correlation}$$

$$S_R = \left( \frac{50}{k_R^+} \right)^2 \quad \text{for } k_R^+ < 25$$

$$= \frac{100}{k_R^+} \quad \text{for } k_R^+ \geq 25$$

where  $k_R^+ \leq 5$  for smooth surfaces.

The  $k-\omega$  model presented here includes low Reynolds number modified closure coefficients, which aim to simulate transition. This form of the coefficients is not strictly necessary in a turbulent boundary layer even if the equations are integrated down to the wall.

#### 1.5.4 Wall functions

##### 1.5.4.1 Wall function corrections for skin friction

The calculation of the viscous shear stresses at solid surfaces is a critical factor in predicting boundary layer development accurately. A simple calculation is adequate if the near wall grid spacing is small, i.e.  $\tau_w = \mu(V_p - V_w) / Y_p$ , where  $V_p$  is the flow velocity at the point nearest to the wall,  $Y_w$  is the distance of the point from the wall, and  $V_w$  is the velocity of the wall.

For equilibrium turbulent boundary layers, this gives accurate results if the point nearest the wall is in the laminar sub-layer, (i.e  $y^+ < 5$ ), but it underestimates  $\tau_w$  for coarse grids. For example, assuming Spalding's expression for the law of the wall, the error is just over 50% if the first point is at  $y^+ = 25$ . It is then necessary to apply corrections based on the law of the wall to give a closer estimate to the velocity gradient at the wall. The corrections can be correlated against  $\rho(V_p - V_w)Y_p/\mu$  in order to avoid the expense of solving the law of the wall during the calculation.

##### 1.5.4.2 Wall functions for high Reynolds number turbulence models

In order to avoid the use of grid nodes very near to the wall ( $y^+ < 5$ ), wall functions are often used. Let  $\Delta y$  be the size of the nearest cell to the wall,  $V$  be the velocity  $V$  at  $\Delta y$ , and  $\Theta = (T_{\Delta y/2} - T_y)$ , where  $T$  = temperature. Then

$$R_{\Delta y} = \frac{\rho V \Delta y}{\mu}, \quad \alpha_p = \frac{\tau_p \Delta y}{2 \mu V}, \quad \beta_p = \frac{q_p \Pr \Delta y}{2 \mu c_p \Theta}$$

The boundary conditions for  $k$  and  $\epsilon$  at the wall are:

$$k = \frac{u_t^2}{\sqrt{C_\mu}}, \quad \epsilon = 0.25 \frac{u_t^3}{K \Delta y}.$$

In these equations,  $Pr$  is the Prandtl number,  $q_p$  is the wall heat flux,  $\tau_p$  is the wall shear stress, and  $u_t$  is the friction velocity.

According to Shabbir et al (1997), the following relations due to Shih and Lumley (1993) must be used for  $y^+ > 11$ . They also allow the integration of the equations up to the wall.

$$k = 0.25 u_t^2, \quad \epsilon = 0.25 \frac{u_t^4}{v_{lam}}$$

The friction velocity  $u_t$  (or the wall shear stress  $\tau_p$ ) is deduced from the coefficient  $\alpha_p$ . Similarly, the wall heat flux is deduced from the coefficient  $\beta_p$ . One of two models could be used, or a blending of the two models to form a third model:

##### 1st model

Assume a Couette flow with turbulence in equilibrium near the wall:

$$\alpha_{1p} = 1 + F_1, \quad \beta_{1p} = 1 + F_1 G$$

where

$$F_1 = \frac{\left( \frac{R_{\Delta y}}{120} \right)^2 \left( \frac{R_{\Delta y}}{447} \right)^{0.825}}{1 + \frac{R_{\Delta y}}{80} + \left( \frac{R_{\Delta y}}{120} \right)^2}, \quad G = \frac{\frac{P_r}{P_{r,T}}}{1 + P \sqrt{\frac{2(\alpha - 1)}{R_{\Delta y} + 300}}},$$

$$P = 9.24 \left[ \left( \frac{P_r}{P_{r,T}} \right)^{0.75} - 1 \right] \left[ 1 + 0.28 \exp \left( -0.007 \frac{P_r}{P_{r,T}} \right) \right].$$

##### 2nd model

The turbulence is produced outside the wall boundary layer, and is diffused towards the wall:

$$\alpha_{2p} = 1 + F_2, \quad \beta_{2p} = 1 + F_2 G$$

where

$$F_2 = \exp \left( \frac{-v_t^+}{20} \right) + \frac{v_t^+}{3.05 + \ln(1 + v_t^+)} - 1, \quad v_t^+ = \frac{v_t}{v}$$

##### 3rd model

a blending of the first two models (Duchêne, 1995):

$$\alpha_{3p} = 1 + F_3, \quad \beta_{3p} = 1 + F_3 G$$

$$F_3 = \max(F_1, F_2)$$

#### 1.5.5 Validation of turbulence models

The use of a reliable turbulence model being an important key to capturing the main features of complex internal flows, and then to predict the losses, several studies comparing different turbulence models according to different levels of grid refinement have been done.

Chima et al (1993) presented a modified Baldwin-Lomax model showing good agreement with experimental measurements of kinetic energy efficiency for an annular turbine cascade, and of heat transfer at the endwall for a linear turbine cascade.

Several other authors have presented results with a modified Baldwin-Lomax model (see for instance Granville, 1987 and York, 1985). The "2D ONERA bump" is a typical configuration used to validate turbulence models for shock/boundary layer interaction. This test case has been used in the EUROVAL project (Haase, 1993) and more recently for an ETMA Workshop organized by UMIST (ETMA, 1994). In these references, several calculations

performed with a mixing-length model, a two-transport equation model, or an ASM or RSM model, using space centred or upwind discretisations, are detailed. In particular, systematic comparisons of mean and turbulent quantities are presented. From these results it appears that, for methods using second order space accuracy, the influence of the turbulence model is greater than the influence of the space discretisation if sufficient mesh refinement is used. The Baldwin-Lomax and Michel models do not predict the characteristic  $\lambda$  shock interacting with the viscous layer. The k- $\epsilon$  model provides a better representation of the shock behaviour but underpredicts the separation zone, whereas a multi-scale model (Gleize, 1994) is as close to the experiment as an RSM simulation presented in (Lien, 1993).

Biswas (1994) gave some examples of the different k- $\epsilon$  model versions and compared them on a flat plate test case (Savill, 1993) and on a turbine blade. A detailed study of the flow in a transonic fan, modelled by different Baldwin-Lomax and k- $\epsilon$  versions, was presented by Jennions and Turner (1993). In this paper, it is shown how an extended k- $\epsilon$  model, which takes into account multiple time scales, provides a better prediction of the shock position.

A 3D shock/boundary layer interaction in a transonic channel with a swept bump has been measured and compared with simulations performed using the Michel model and using the k- $\epsilon$  model (Cahen, 1993). The results show, as for 2D cases, a better prediction using the k- $\epsilon$  model in the shock/boundary layer interaction region, as in the corner regions, which is an interesting point for 3D turbomachinery applications. A comparison of skin-friction pattern lines between calculation and experiment, presented for the wall bearing the bump and for the adjacent wall with a strong interaction, shows the interesting behaviour of the predicted solution. Nevertheless, even if the main tendencies are well represented, the k- $\epsilon$  calculation does not predict correctly the levels of kinetic energy and the length of the separation zone in the interaction region. A comparison between a Baldwin-Lomax model and a k- $\epsilon$  model for a 3D subsonic blade row configuration was presented by Matsuo (1991). As above, it shows also that the k- $\epsilon$  model leads to a better prediction of the separated region, even if the secondary flows are not correctly reproduced.

Fougères (1994) undertook numerical simulations of heat transfer with film cooling using the Michel model for a flat plate test case and for a nozzle guide vane configuration. These calculations were done by using overlapping grids to refine the fluid injection holes accurately. It is demonstrated that a good quality fine mesh is required to obtain well-predicted heat transfer coefficients.

## 1.6 CODE VALIDATION

As already indicated, 3D steady viscous turbomachinery applications are commonly computed today with solvers which have been "calibrated" on typical test cases where detailed experimental data are available. In order to validate these solvers, not only the wall pressure distribution is needed but also finer experimental measurements, like boundary layer velocity profiles, heat transfer coefficients, wall stresses and velocity vectors in the field. In this section some examples are presented of compressor and turbine blade flow calculations which are typical of the state of the art reached for these configurations, and which have been performed on grids probably finer than those currently used in the blade design process. See, for instance, the proceedings of the AGARD Conference on CFD techniques (AGARD, 1991) and the proceedings of the seminar organized by the

ERCOFTAC Turbomachinery Special Interest Group (Gregory-Smith, 1993) to find various turbomachinery flow calculations compared with experiment.

### 1.6.1 Compressor flows

Several authors have tested their codes on the NASA Lewis Rotor 67 fan documented by Fottner (1990), and some of these calculations, including tip clearance, are reported in AGARD (1991). As regards the detailed analysis of tip leakage phenomena in compressor configurations, in terms of the physics and also the influence of the mesh on numerical solutions, see for instance Adamczyk (1993), Chen (1991), and Kang (1993). For such a transonic compressor, different complex flow features provide an interesting challenge to validate numerical methods: a bow shock, a separation zone induced by the passage shock/boundary layer interaction on the suction surface, tip-leakage, and a strong radial flow, ... Two flow configurations, corresponding to the peak efficiency condition and the near stall condition, are presented by Hah (1992) using a k- $\epsilon$  model on a 250,000 point H grid and by Arnone (1994) using a Baldwin-Lomax model on a 350,000 point H grid. In comparison with laser measurements, both calculations reproduce the main features of the shock structure at different sections of the span.

Couaillier (1991) performed a calculation on the SNECMA TS27 wide chord fan at the peak efficiency condition, using a 617,000 point H-O-H grid. No tip clearance was taken into account and a slip condition was imposed on the casing. The use of an O Mesh around the blade led to an accurate representation of the leading edge bow shock, and comparison with laser measurement data showed good agreement with the shock location.

Nozaki (1993) simulated the flow through a complete stage of a fan configuration for different operating points. The calculations did not take into account unsteadiness because the boundary conditions on the rotor/stator interface were set to circumferentially averaged values. Nevertheless, the overall time-averaged performance showed a qualitatively good agreement with the experimental measurements.

The ASME test case exercise in 1994 using Rotor 37 has already been mentioned as one of the starting points of the present WG.

### 1.6.2 Turbine flows

The use of 3D Navier-Stokes solvers gives the opportunity to analyse such typical flow features as film cooling, heat transfer, and transition phenomena. As an example of a turbine test case with strong effects of transition phenomena and secondary flows, the Durham cascade (Gregory-Smith, 1992) has been computed by several groups and reported by Gregory-Smith (1994). It appears that the calculated solutions are largely dependent on the turbulence models and transition criteria. The analysis presented by Wegener (1992) showed comparisons of the wake development behind an annular turbine stator predicted by two different solvers with the experiment. A numerical study of heat transfer for a 2D turbine rotor cascade and for a 3D turbine cascade near the endwall was presented by Hah (1989). The 3D computation, which was performed with a k- $\epsilon$  model on a 600,000 grid point mesh, provided a numerical solution showing an acceptable accuracy for heat transfer prediction. A Navier-Stokes analysis of turbine blade heat transfer was also presented by Dorney (1991).

Zimmermann (1992) used the Baldwin-Lomax model to undertake a numerical analysis of the total pressure losses in

a transonic turbine cascade. Comparisons with experiment show acceptable predictions, and an analysis of the pressure loss components leads to the conclusion that the total pressure losses depend strongly on secondary flows. The analysis presented by Horton (1991) showed the influence of the mesh quality on total loss pressure prediction with two endwall geometries of a transonic turbine.

Linear cascades and rotor turbine configurations with tip clearance were calculated by Fourmaux (1993) using the Michel model. Both for the linear cascade and the rotor configurations, a five-domain mesh with 11 points in the gap between the blade tip and the casing was used. When comparing results obtained with and without tip clearance representation, large differences in the flow field were seen in the hub region, covering 25 % of the blade in the spanwise direction.

## Chapter 2

### THE TEST CASES

The two test case data sets described in this report were selected by the members of the Working Group from a larger group of candidate sets. They are

- (1) an isolated axial-flow compressor rotor designed and studied experimentally at the National Aeronautics and Space Administration Lewis Research Center (US), identified as NASA Rotor 37.
- (2) an axial-flow turbine inlet stator blade row designed and studied experimentally in the Institut für Antriebstechnik of the Deutsche Forschungsanstalt für Luft - und Raumfahrt e.V. (GE). This configuration is identified here as the DLR turbine stator.

These data sets were selected following a thorough review of the experimental programmes and the available data. Both configurations were representative products of proven design methods and carefully-controlled manufacturing processes. The test programmes were carried out in well-developed test installations operated by experienced research groups. In both programmes a wide range of data were available, based on proven instrumentation and data acquisition methods, and reduced by accepted and traceable procedures. Finally both test cases involved experiments under steady-state entrance flow conditions, with internal and exit flows representing a substantial challenge to current CFD codes.

In the following sections the two test cases are individually discussed, with reference to design background, flow path and blade geometry, test installation and methods, and definition of the data available and relevant to the current study.

#### 2.1 NASA ROTOR 37

##### 2.1.1 Design Background

Rotor 37 was designed and initially tested as part of a research programme involving four related axial-flow compressor stages. These stages were intended to cover a range of design parameters typical of aircraft turbine engine high-pressure (core) compressor inlet stages. In the case of stage 37, representative values were:

Rotor inlet hub-to-tip diameter ratio	0.7
Rotor blade aspect ratio	1.19
Rotor tip relative inlet Mach number	1.48
Rotor hub relative inlet Mach number	1.13
Rotor tip solidity	1.29
Blade airfoil sections	Multiple-Circular-Arc (MCA)

No inlet guide vanes were specified for any of the stages. Some design information and overall stage performance results were reported by Reid and Moore (1978). More detailed stage performance was reported later by Moore and Reid (1980). It should be noted that while the designs and stage tests were initiated during the 1970's, geometries and performance levels are similar to those for current turbine engine stages.

Design point values for the rotor as estimated in the design computations were:

Equivalent rotational speed

$$N \sqrt{\frac{T_{ref}}{T_{in}}} = 17188.7 \text{ rpm} \quad (1800 \text{ rad/s})$$

where  $T_{in}$  = inlet total temperature

$T_{ref} = 288.15 \text{ K}$  (sea level standard atmosphere)

$$\text{Equivalent rotor tip speed } U_t \sqrt{\frac{T_{ref}}{T_{in}}} = 454.1 \text{ m/s}$$

Equivalent mass flow per unit annular area

$$\frac{\dot{m}}{A_{an}} \frac{P_{ref}}{P_{in}} \sqrt{\frac{T_{in}}{T_{ref}}} = 200.5 \text{ kg/s/m}^2$$

where  $P_{in}$  = inlet total pressure

$P_{ref} = 101.33 \text{ kN/m}^2$  (sea level standard atmosphere)

$A_{an}$  = annulus area

Rotor total pressure ratio = 2.106

Rotor polytropic efficiency = 0.889

Number of rotor blades = 36

##### 2.1.2 Configuration Geometry for WG26 Test Case

Subsequent to the tests of Moore and Reid (1980) on NASA Stage 37, the rotor was retested as an isolated component. This is the geometry identified by NASA as Rotor 37. Fig.2.1 shows in schematic form the annular flow path and blade airfoil geometries with coordinate reference definitions for computational purposes. These coordinate definitions are those utilized in all data reported and in all performance computations reported in other sections of this document. All of the values are estimated design point operating values of dimensions and angles. Detailed numerical values of passage and blade coordinates are not given in this document but are available by electronic data file transfer as outlined in Section 2.1.5.

Additional geometry of interest for CFD purposes is shown in Fig. 2.1. The blade hub fillet radius was 2.5 mm and the RMS blade surface roughness was 0.5 - 1.25 microns.

##### 2.1.3 Test Installation

Figure 2.2 is a schematic diagram of the single-stage axial-flow compressor stage test installation at the NASA Lewis Research Center in Cleveland, Ohio (US). This is the facility used for all experimental work on the NASA Stage 37 and Rotor 37 configurations. Atmospheric air enters the system through an inlet and filters, followed by a standard thin-plate orifice for compressor mass flow rate measurement. Compressor inlet pressure and mass-flow rate are set by combined use of parallel butterfly valves in the inlet ducting and a sleeve throttle between the test unit and the collector ducting. Air enters the test compressor from an upstream plenum tank containing screens and a honeycomb grid. Flow enters the annular flow path of Figure 2.3 through a bell-mouth inlet with a central nose cone and three airfoil-shaped support struts. The installation exhausts to the atmosphere or to the Center altitude exhaust system. Atmospheric exhaust was utilized in all Rotor 37 experiments.

The test compressor is driven by a 3000 hp alternating current motor through a speed-increasing gear box. Motor speed is varied by changing supply power frequency.

##### 2.1.4 Experimental Programme

The data sets selected for the PEP Working Group 26 test case were developed during 1992 and 1993. The same data were the basis for an extensive CFD code assessment effort sponsored by the ASME International Gas Turbine Institute's Turbomachinery Committee during 1993 and 1994. Wisler (1993) and Denton (1996) discuss the organization and results of this work.

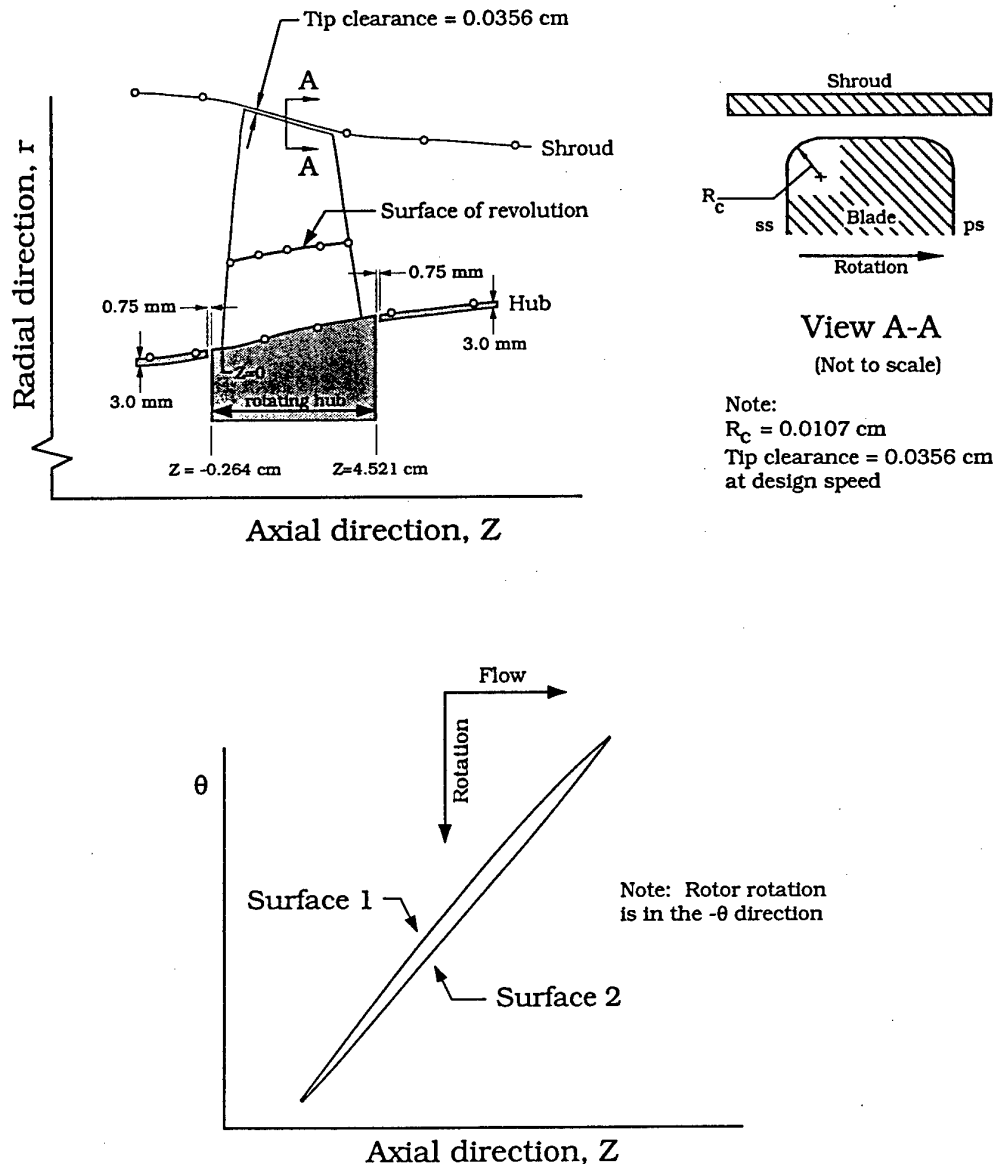


Figure 2.1 Blade and flowpath coordinates

#### 2.1.4.1 Test Conditions

All of the data used in the AGARD and ASME code validation studies were measured with NASA Rotor 37 operating at the design equivalent rotational speed defined above. To establish reference points for detailed flow field measurements, overall performance was determined at equivalent mass flow rates from the maximum attainable, referred to in this document as  $\dot{m}_{choke}$ , to a minimum slightly above the rotor stall flow. This near stall flow rate was experimentally determined to be  $\dot{m} / \dot{m}_{choke} = 0.925$ . A total of 13 sets of overall performance data were measured over this mass flow rate range. These points are shown on Figure 2.4.

Data points  $\dot{m} / \dot{m}_{choke} = 0.98$  and  $\dot{m} / \dot{m}_{choke} = 0.925$  were designated by both ASME and the Working Group as flow rates for concentration of CFD effort. The experimental  $\dot{m}_{choke}$  as determined by NASA was 20.93 kg/s. All reported

values are equivalent values referenced to sea-level standard atmosphere values of  $P_{ref}$  and  $T_{ref}$ .

#### 2.1.4.2 Performance Measurement

The performance data acquired for the NASA Rotor 37 test case include averaged overall total pressure ratio and adiabatic efficiency for a range of equivalent mass flow rates with the rotor operating at the design value of equivalent rotational speed. Mass flow rates reported are based on the test facility orifice plate measurements. Rotational speed was measured using a shaft-mounted magnetic pick-up system and an electronic counter.

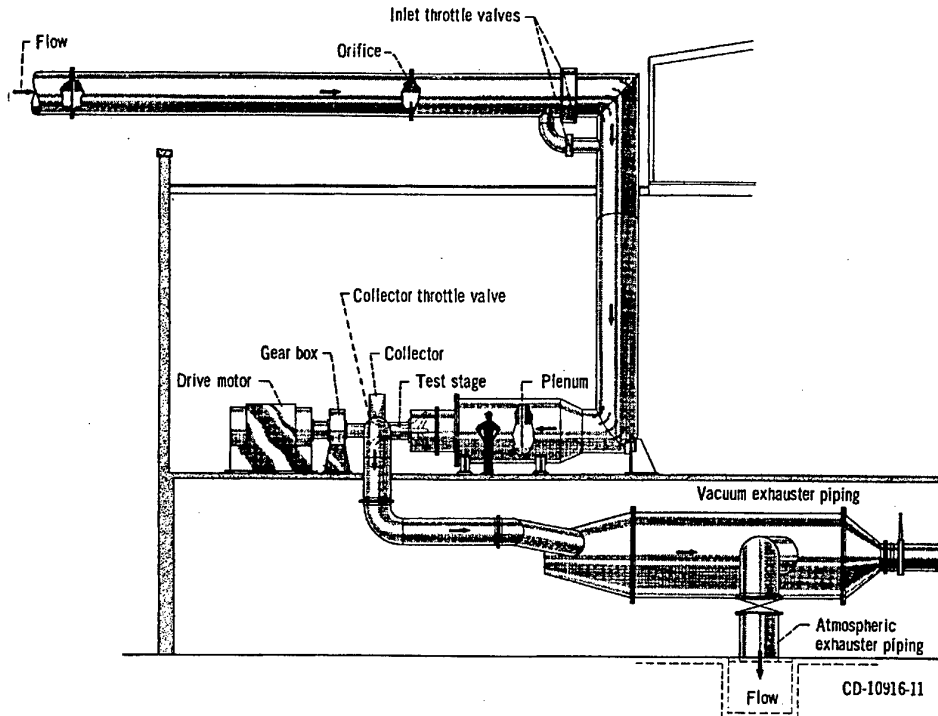


Figure 2.2 Test facility

In addition, flow passage data based on radial surveys with pneumatic pressure probes and thermocouples were recorded at each equivalent mass flow rate at design equivalent rotational speed. The surveys were at Station 1 and Station 4 (Fig. 2.3). The probes used were a combination probe with a "cobra" head for total pressure and absolute flow angle information, with a thermocouple for total temperature data; and a wedge probe for static pressure data. Wall static pressure taps were also located on hub and tip walls at Stations 1 and 4. The circumferential locations of survey positions are shown in Figure 2.5. Radial surveys included 18 measurement locations.

Turbulence intensity was measured at Station 1. Laser anemometer velocity data were acquired in four hub-to-tip measuring planes, and also on five blade-to-blade surfaces of revolution. Locations of these planes and surfaces are defined schematically on Figure 2.3. The laser anemometer system used and the procedures followed have been described in detail by Suder et al (1995), Suder and Celestina (1996) and Hathaway et al (1993). Laser data were acquired only at flow rates of  $\dot{m} / \dot{m}_{choke} = 0.98$  and 0.925.

#### 2.1.4.3 Data Reduction

For the ASME test case exercise, the averaging scheme used to calculate the performance from the CFD results was closely defined by Wisler (1993), and these same definitions were adopted by the Working Group.

For obtaining pitchwise averages, the measured total pressures and temperatures, axial and radial velocities are

mass-averaged, and the mean angle is calculated from those averaged velocities. For comparing overall performance with measured values, the preferred method is to interpolate the pitchwise-mean computed values at the radial locations of the measurement points given in Tables 2.1 and 2.2, and then mass-average those values radially. The flow area associated with each measurement location is also given in those tables. This ensures that the overall performance figures are directly comparable despite the relatively sparse distribution of the measurement points.

The equations defining these averages can also be obtained as described in the next Section.

#### 2.1.5 Test Case Data

The data sets selected for the WG26 code evaluation included averaged overall performance values, rotor entrance and exit (Stations 1 and 4) probe survey information and selected laser velocimeter results. These data as well as the configuration geometry may be obtained by mailing a request to Dr K. L. Suder at the NASA Lewis Research Center, Cleveland, OH 44135, U.S.A. Request letters should include a current electronic mail address.

##### 2.1.5.1 Defined Values for CFD Code Input

Turbulence intensity = 3% at station 1.

$P/P_{ref}$  and  $T/T_{ref}$  values in Table 2.1 for Station 1 should be used in describing entrance conditions for CFD codes, including calculation of  $\dot{m} / \dot{m}_{choke}$ .

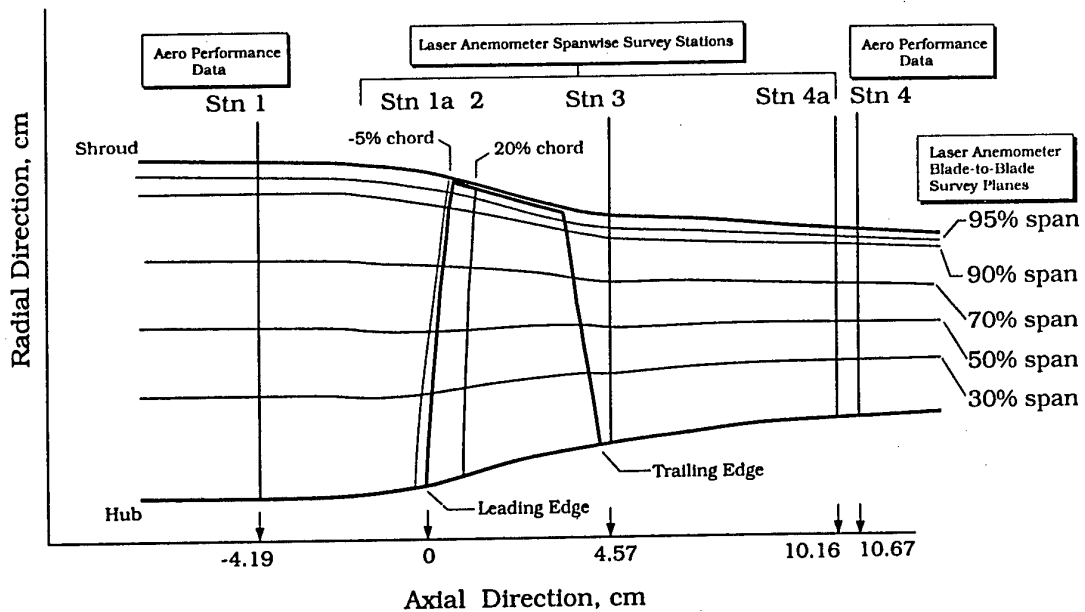


Figure 2.3 Measurement stations

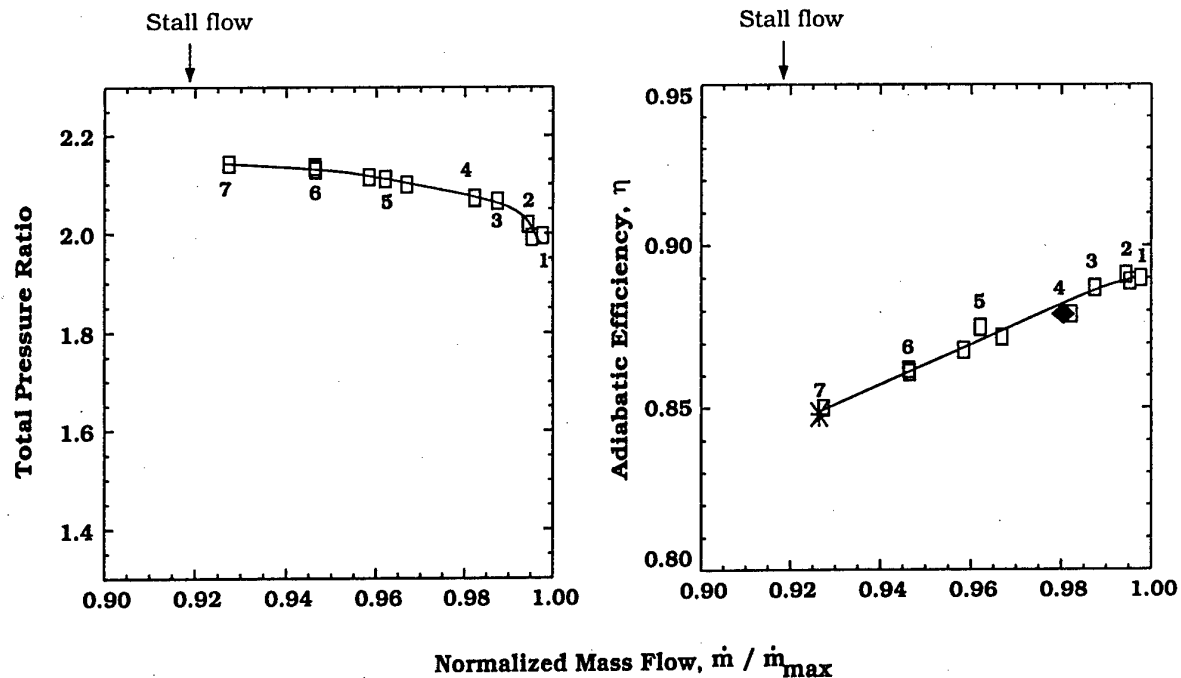


Figure 2.4 Overall performance at station 4



Figure 2.5 Instrument positions (facing upstream)

Table 2.1 Aerodynamic Survey Measurement Locations and Flow conditions at Station 1, z = 4.19 cm

point	% span	radius (cm)	P/Pref	T/Tref	$\Delta A_{an}$ (cm <sup>2</sup> )	% area
1	97.0	25.4203	0.9435	1.0008	59.3723	0.0537278
2	94.0	25.1765	0.9762	1.0004	45.7621	0.0414115
3	90.0	24.8412	0.9959	1.0004	57.0518	0.0516279
4	85.0	24.4450	1.0020	1.0002	63.1837	0.0571768
5	80.0	24.0182	1.0041	1.0000	62.1197	0.0562140
6	75.0	23.6220	1.0048	1.0002	58.8042	0.0532137
7	70.0	23.2258	1.0041	1.0006	60.0314	0.0543242
8	65.0	22.7990	1.0034	1.0008	69.7699	0.0631369
9	58.0	22.2504	1.0041	1.0004	78.8012	0.0713096
10	51.0	21.6713	1.0048	0.9996	78.8530	0.0713565
11	44.0	21.0922	1.0054	0.9994	74.7585	0.0676512
12	37.0	20.5435	1.0054	0.9990	72.7605	0.0658431
13	30.0	19.9644	1.0054	0.9988	61.3109	0.0554821
14	25.0	19.5682	1.0054	0.9988	50.5746	0.0457665
15	20.0	19.1414	1.0054	0.9988	49.5106	0.0448036
16	15.0	18.7452	1.0054	0.9987	46.6640	0.0422276
17	10.0	18.3490	1.0040	0.9990	47.4221	0.0429137
18	5.0	17.9222	0.9864	1.0004	68.3072	0.0618133

hub radius = 17.5259 cm

tip radius = 25.6692 cm

area = 1105.06 cm<sup>2</sup>

Table 2.2 Aerodynamic Survey Measurement Locations at Station 4, z = 10.64 cm.

point	% span	radius (cm)	$\Delta A_{an}$ (cm <sup>2</sup> )	% area
1	97.0	23.7134	25.3625	0.0420720
2	94.0	23.5915	22.5758	0.0374494
3	90.0	23.4086	31.3590	0.0520192
4	85.0	23.1648	33.2834	0.0552114
5	80.0	22.9514	30.7671	0.0510373
6	75.0	22.7381	32.6485	0.0541582
7	70.0	22.4942	32.3201	0.0536135
8	65.0	22.2809	36.2286	0.0600970
9	58.0	21.9761	42.0868	0.0698147
10	51.0	21.6713	43.5641	0.0722654
11	44.0	21.3360	42.9205	0.0711977
12	37.0	21.0312	40.2774	0.0668134
13	30.0	20.7264	35.7477	0.0592993
14	25.0	20.4826	29.4308	0.0488206
15	20.0	20.2692	27.1778	0.0450834
16	15.0	20.0558	28.7959	0.0477674
17	10.0	19.8120	28.4675	0.0472227
18	5.0	19.5986	39.8218	0.0660575

hub radius = 19.381 cm

tip radius = 23.823 cm

area = 602.835 cm<sup>2</sup>

## 2.2 DLR CASCADE

### 2.2.1 Test Case

The annular test cascade is a scaled version of a subsonic, low aspect ratio turbine stator. This stator is scaled by a factor of 2.348 and has constant hub and tip radii. The aim of the tests was to provide detailed information about the flow field inside the passage as well as upstream and downstream of the blade row. The measurements carried out were performed with a 5-hole probe downstream of the stator and with the three dimensional Laser-Two-Focus (3D-L2F) measuring technique inside the passage and downstream. Additionally the upstream boundary layers were traversed using a "fish-mouth" pitot probe.

### 2.2.2 Facility and Instrumentation

The tests were carried out in the DLR annular turbine test rig with 25 blades mounted on the stator hub (Fig. 2.6). It is an open loop continuously operating facility supplied with cold air (maximum temperature 315K, maximum pressure 2.0 bar) and the following main dimensions:

hub diameter, $d_H$	0.315 m
tip diameter, $d_T$	0.400 m

The operating point was determined by measuring the mass flow, the total pressure and the total temperature upstream of the stator.

The 5-hole probe used to measure the flow field downstream of the blade row is mounted in computer controlled actuators which allow spanwise traversing. Pitchwise traversing was achieved by turning the complete stator hub with the blades. The resultant tip leakage is prevented by a tiny plastic tip seal. The flow field was measured in a plane 40% axial chord length behind the stator measuring plane 3 (MP3). There the number of radial measuring positions was 18 and the number of circumferential positions was 15, arranged equidistantly.

The applied L2F measuring technique is described in detail in Schodl (1989). Because the 3D-L2F measurements are very time consuming, the flow field is highly resolved only in the regions of interest. The undisturbed mainflow is described at some characteristic points. For MP1 and MP2 the nearest measuring points to the suction side are at a distance of 0.5 mm from the surface. The distribution of the measuring points is shown by the beginning of the contour plot presentation for each measuring plane.

The axial position of the measuring planes (MP) of the 5-hole probe measurements and the Laser-Two-Focus measurements are shown in Figs. 2.7 and 2.8.

### 2.2.3 Cascade and geometry

The blade geometry at mid-span is shown in Fig. 2.7. The main dimensions are indicated below:

number of blades	25
chord length at hub, $C_H$	0.0622 m
Chord length at mid span, $C_{MS}$	0.0698 m
chord length at tip, $C_T$	0.0768 m
axial chord length at mid span, $C_{ax, MS}$	0.0445 m
aspect ratio, $l/C_{MS}$	0.61
outlet flow angle rel. to tangl direction, $\bar{\alpha}_3$	20.5°

The 3D-blade coordinates are available on a floppy disk, which may be obtained from C. Langowsky, DLR, Institut für Antriebstechnik, D-51140, Köln, Germany.

### 2.2.4 Uncertainty and evaluation methods

#### 2.2.4.1 5-hole probe measurements

The measurable variables of the 5-hole probe are evaluated three dimensionally. For this application the probe had to be calibrated for the two flow directions  $\alpha$ ,  $\beta$  and the Mach number. Polynomial approximations were used to relate the calibration data to the measured data (Gallus and Bohn, 1976). A correction method for the influence of the head geometry to the flow with gradients on the measured results is not used. Thus, the original data are presented. Unsteady effects as described for the 3D-L2F measurements could not be detected with the 5-hole probe.

The estimated uncertainty of the 5-hole probe data is as indicated below:

flow angles $\alpha$ , $\beta$	$\pm 0.5^\circ$
pressures $p_t$ , $p_{st}$	$\pm 0.1$ mbar

For the radial-distribution plots, two circumferential averaging techniques were used depending on the specific quantity being averaged. These are the area-average and the mass-average defined as follows:

Area-average of a quantity  $F$ :

$$\overline{F}_a = \frac{\int F dA}{\int dA}$$

Mass-average of a quantity  $F$ :

$$\overline{F}_m = \frac{\int F \cdot p v_{ax} dA}{\int p v_{ax} dA}$$

The total pressure  $P_t$  is mass-averaged, while the static pressure  $P_{st}$  is area-averaged. The Mach number emerged from the quantities of the averaged total pressure and static pressure,  $\overline{M} = f(\overline{p}_t, \overline{p}_{st})$ . Reported average flow angles are calculated from the area-averaged velocity components.

#### 2.2.4.2 3D Laser-Two-Focus (3D-L2F) measurements

The measured variables with the 3D-L2F are the projected mean velocity  $v$  and the flow angles  $\alpha$  and  $\beta$ . For the results presented here, the mean velocity  $v$  is converted to the Mach number.

Unsteady effects in the wake region (e.g. von Karman vortex streets) could be resolved with this measuring technique. The statistical evaluation method describes an averaged condition different from the true alternating flow condition. These unsteady effects have an influence only on the measured flow angle  $\alpha$ , which differ slightly in the wake region at measuring plane 3 (MP3) for the two measuring techniques, because they are averaged in different ways.

For the measurements a window of quartz glass with a plane surface is necessary in the casing. An unavoidable tiny tip leakage results due to the deviation to the contour of the casing. For that reason the flow field is slightly disturbed at the tip. The laser device had to be inclined to the quartz glass window for the measurements inside the passage, increasing the possible measurable region. The accuracy, therefore, arises as following:

mean velocity $v$	$\pm 1.5$ m/s	$\pm 1.5$ m/s
flow angle $\alpha$	$\pm 0.1^\circ$	$\pm 0.2^\circ$
flow angle $\beta$	$\pm 0.4^\circ$	$\pm 1.5^\circ$

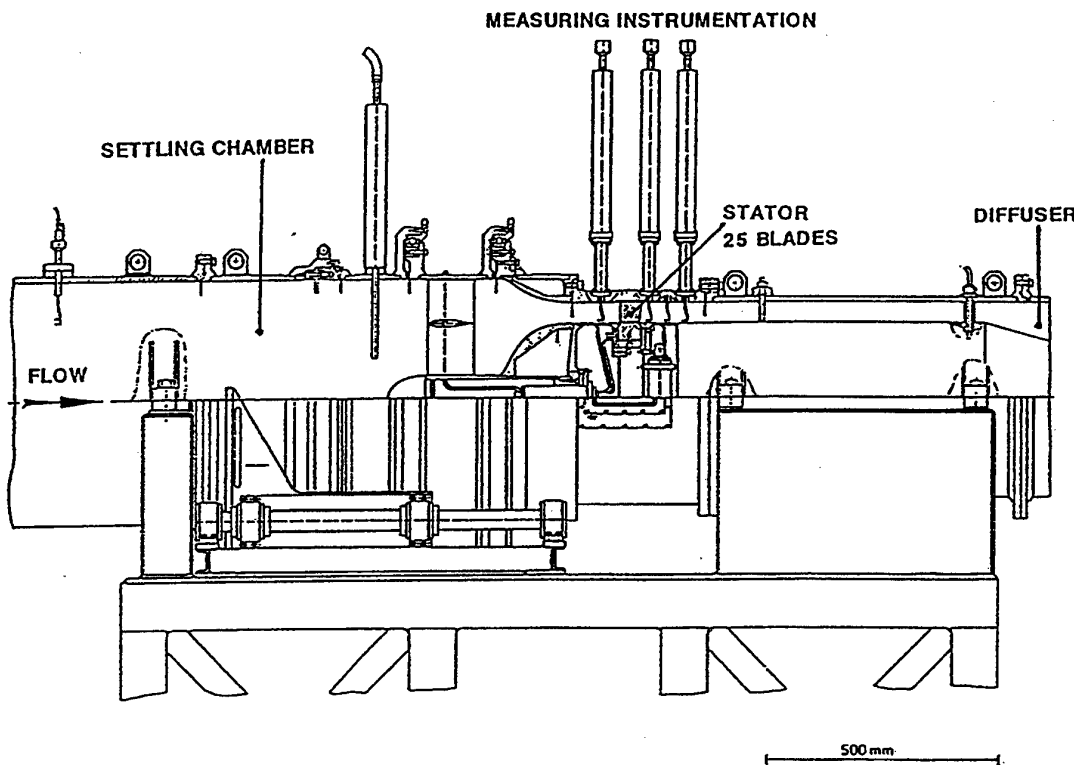


Fig 2.6 DLR test facility

The flow variables  $M$ ,  $\alpha$  and  $\beta$  are based on the area-averaged velocity components for the radial distribution plots.

## 2.2.5 Experimental conditions and results

The characteristic data of the operating point for which the measurements were carried out are listed below:

Mass flow rate, $m_0$	5.490 kg/s
total pressure, $p_{t,0,MS}$	1.6760 bar
total temperature, $T_{t,0}$	306.6K
inlet flow angle, $\alpha_0$ (circumf.)	90°
inlet flow angle, $\beta_0$ (radial)	0°
inlet turbulence level, $Tu_0$	4.4%
inlet Mach number, $M_{a0}$	0.176
mean outlet Mach number, $M_{a3}$	0.74
static pressure at hub, $P_{st,3}$	1.0750 bar
Reynolds number, $Re$	$1 \times 10^6$

The results of detailed 5-hole probe measurements prove that the inlet flow angle at MP=0 is uniform. The incoming boundary layers at hub and tip have a thickness of about 4.5% blade height and their profile is shown in Fig.2.9.

Derived from the 5-hole probe measurements, Figs.2.10-13 present the contour plots of the total pressure ratio, the Mach number, the circumferential flow angle  $\alpha$  and the radial flow angle  $\beta$  at MP 3. The radial distribution of the circumferential averaged total pressure ratio  $p_{t,3}/p_{t,0,MS}$ , Mach number  $M_3$ , static pressure ratio  $p_{st,3}/p_{t,0,MS}$ , and circumferential flow angle  $\alpha$  is shown in Figs.2.14-17. The data for the 5-hole probe measurements are also available on the disk mentioned in Section 2.2.3.

The distribution of the measuring points and the results of the 3D-L2F measurements at MP3 are shown in Figs.2.18-21. The radial distribution of the averaged three flow variables

$M$ ,  $\alpha$  and  $\beta$  is presented in Figs.2.22-24. Contour plots of the measurements inside the passage at MP2 and MP1 and the distribution of the measuring points follow in Figs.2.25-32. The results of the 3D-L2F measurements are also stored on the disk.

## 2.2.6 Nomenclature for Section 2.2

C [m]	chord length
d [m]	diameter
h [m]	blade height
m [kg/s]	mass flow rate
M	Mach number
p [bar]	pressure
r [m]	radius
Re	Reynolds number = $\frac{\bar{v}_3 C_{MS}}{v_3}$
Tu [%]	turbulence level
v [m/s]	velocity
x,y,z	cartesian coordinates
$\alpha$ [°]	circumferential flow angle, rel to tangl.direction
$\beta$ [°]	radial flow angle
$\delta$ [m]	boundary layer thickness
$\phi$ [°]	stator circumferential position
$\nu$ [ $m^2/s$ ]	kinematic viscosity.

### Subscripts and Superscripts

0...3	measuring plane
ax	axial direction
H	hub
MS	mid-span
st	static condition
t	total condition
T	tip
-	averaged

### Symbols

MP	measuring plane
PS	pressure side
SS	suction side
TE	trailing edge

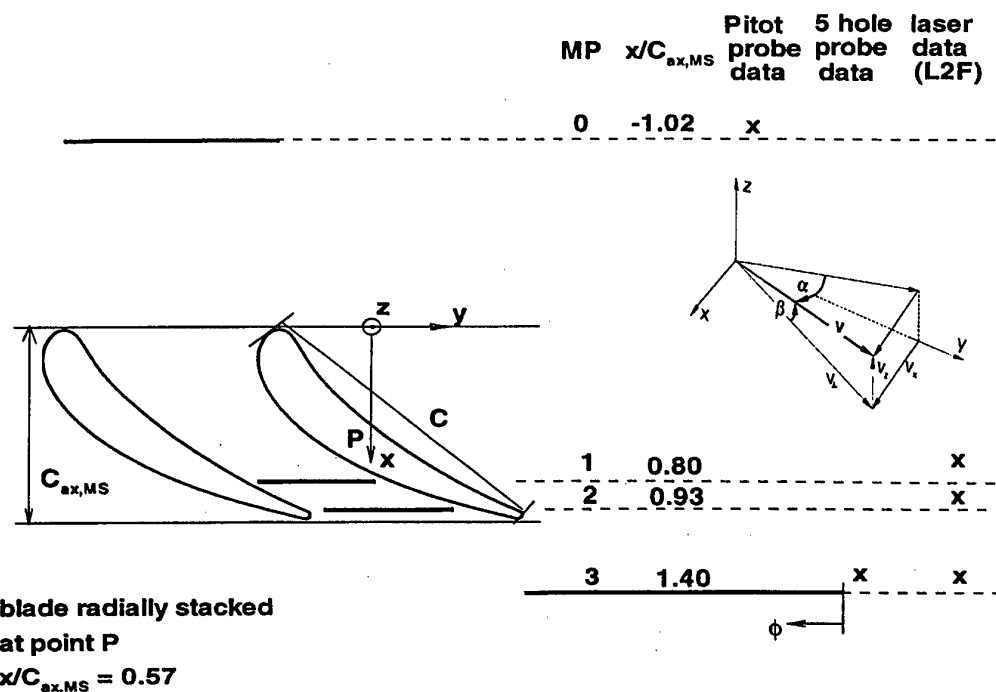


Fig 2.7 Cascade geometry at mid-span and measuring planes

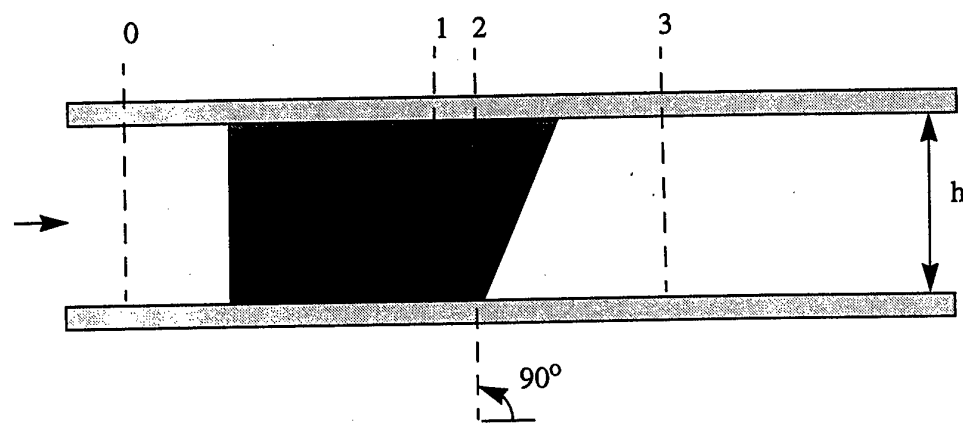


Fig 2.8 Test section

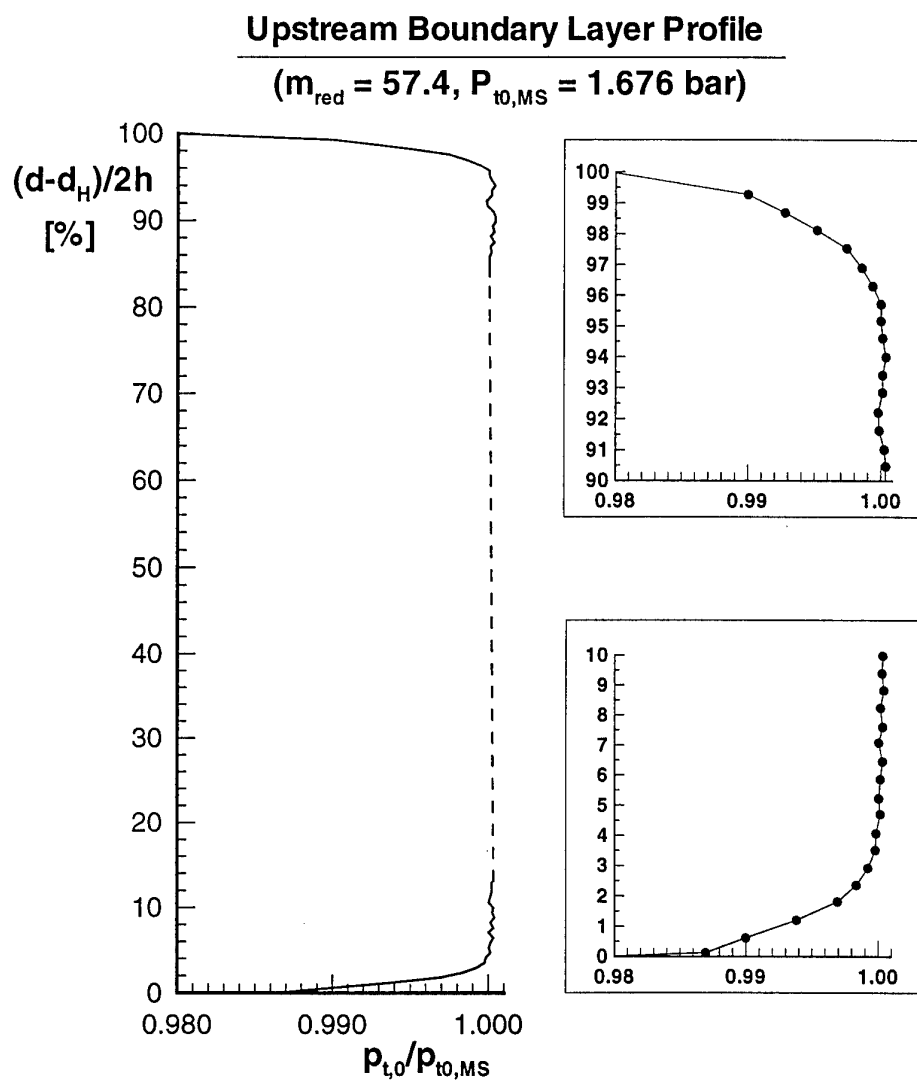


Fig 2.9 Upstream flow condition at measuring plane 0

### Results of the five-hole probe measurements in MP3

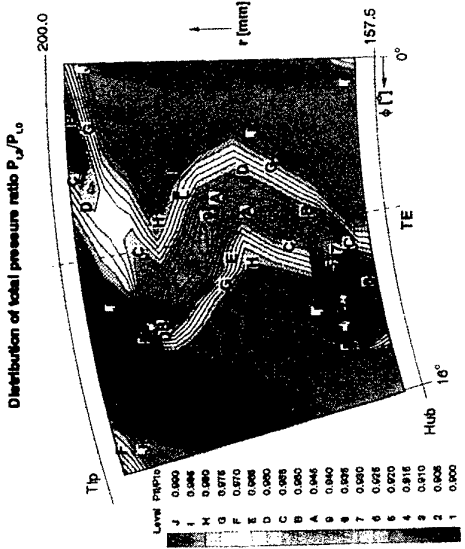


Fig 2.12

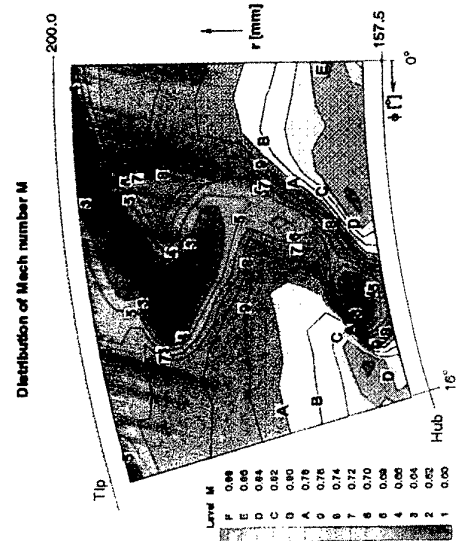


Fig 2.11

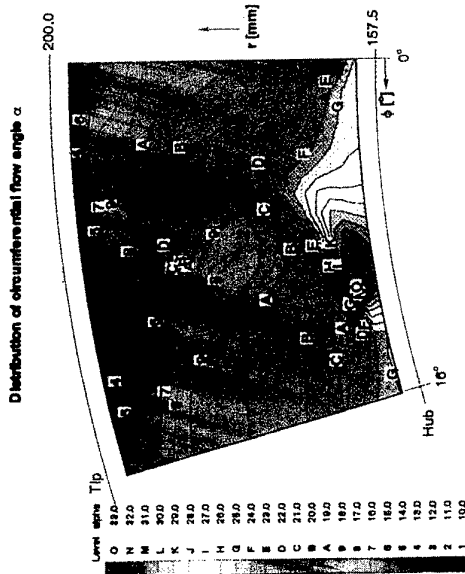


Fig 2.12

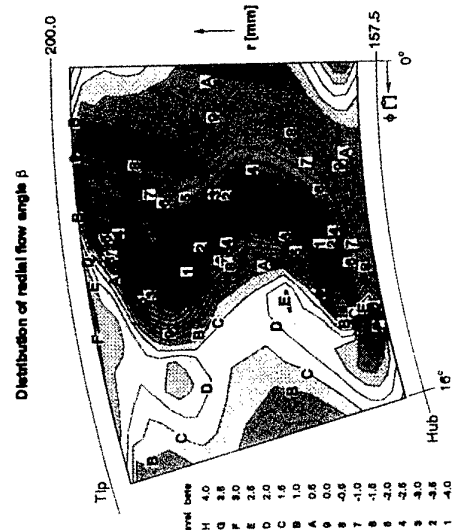
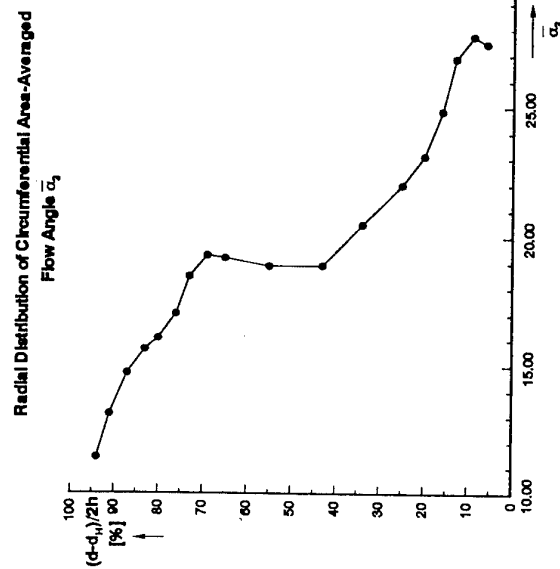
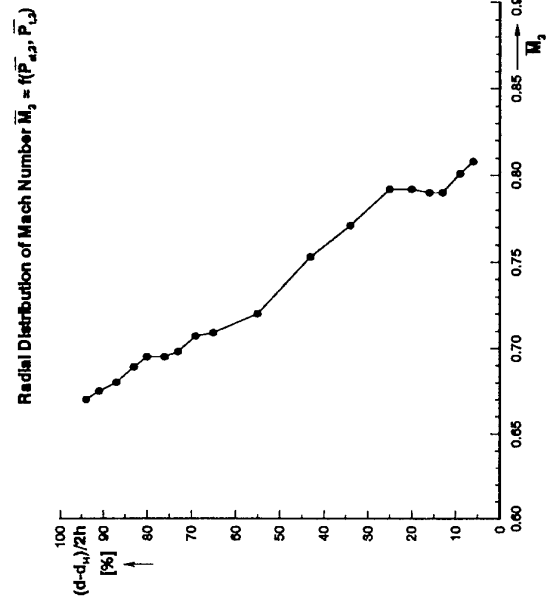
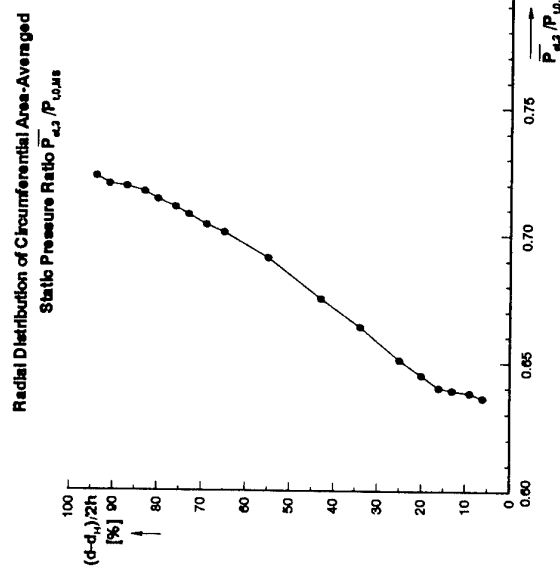
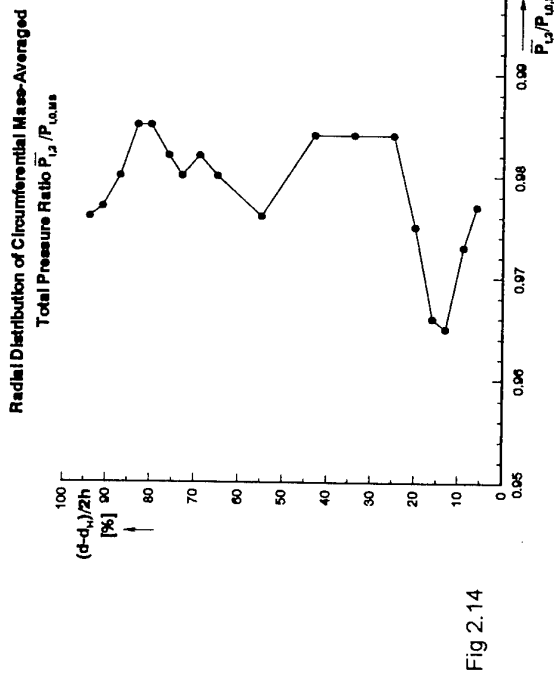


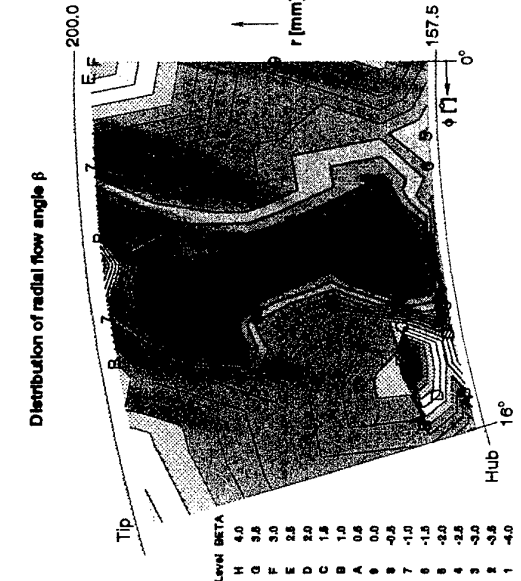
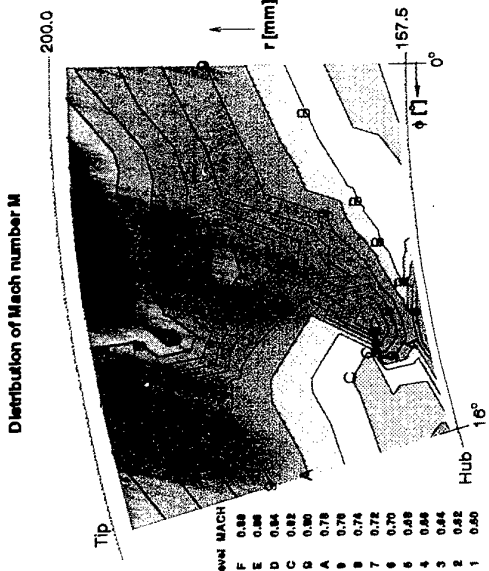
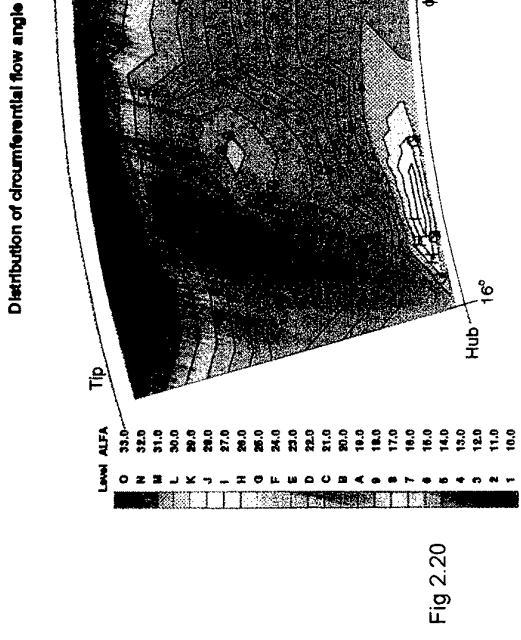
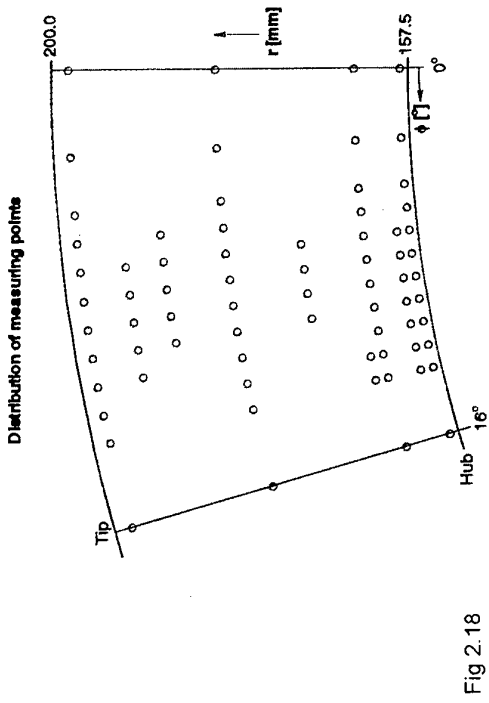
Fig 2.13

### Results of the five-hole probe measurements in MP3



### Results of the 3D-L2F measurements at MP3

22



### Results of the 3D-L2F measurements at MP3

Radial Distribution of Mach Number  $\bar{M}_s$

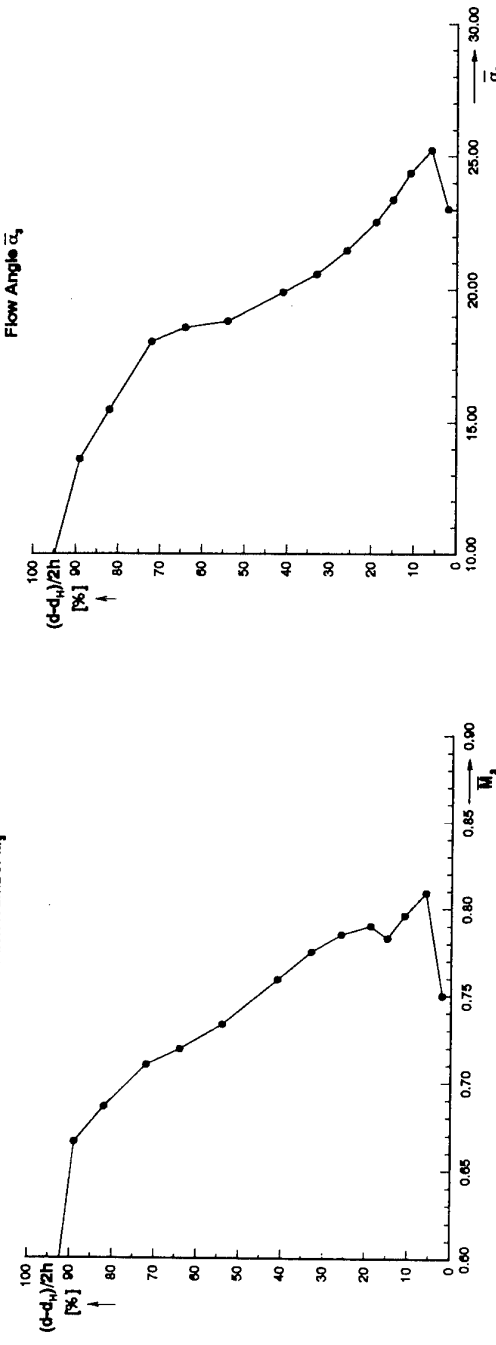


Fig 2.22

Radial Distribution of Circumferential Area-Averaged Flow Angle  $\bar{\alpha}_s$

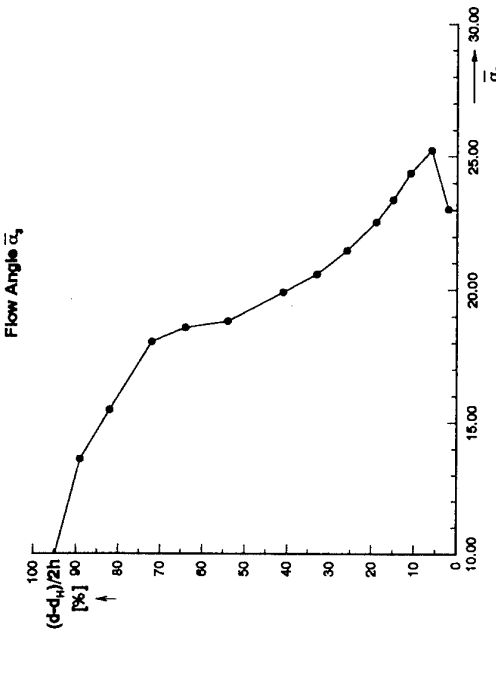


Fig 2.23

Radial Distribution of Circumferential Area-Averaged Flow Angle  $\bar{\beta}_s$

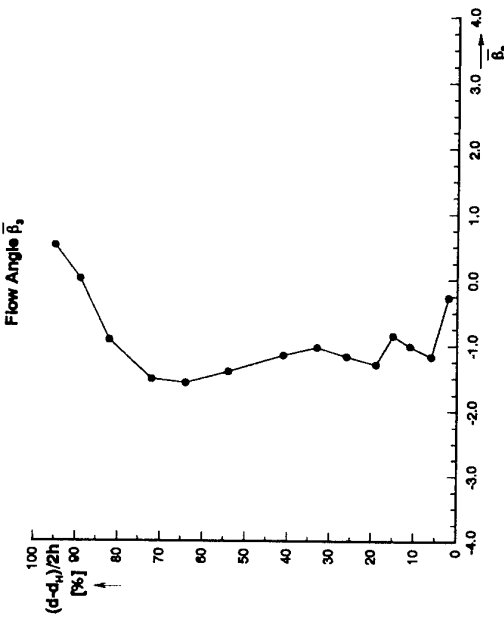


Fig 2.24

### Results of the 3D-L2F measurements at MP2

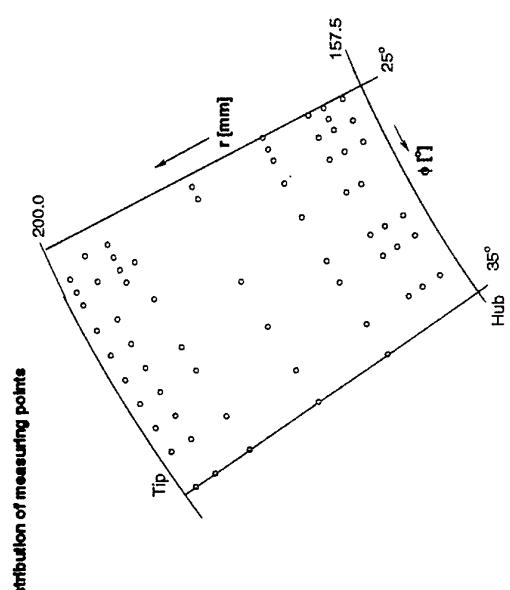


Fig 2.25

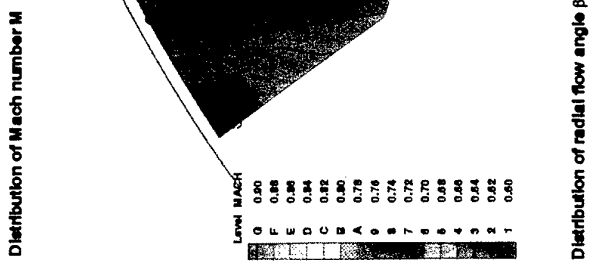


Fig 2.26

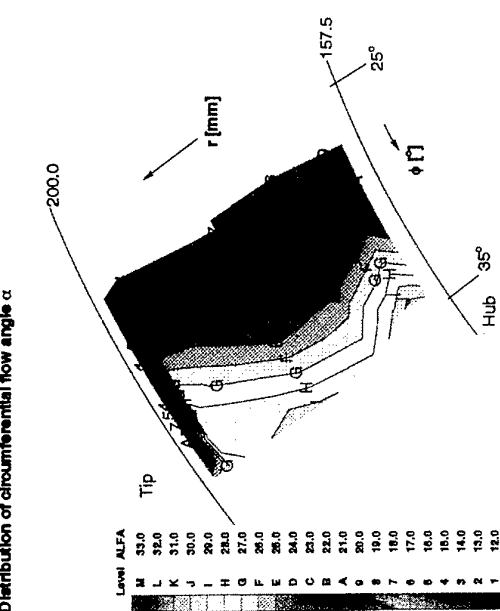


Fig 2.27

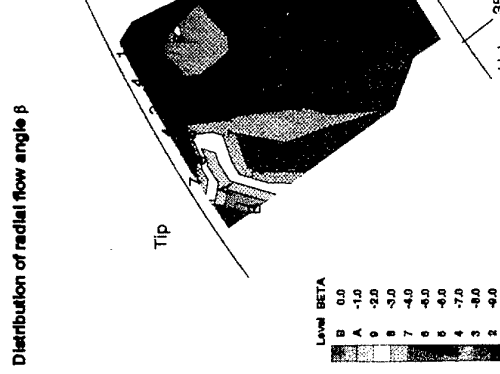
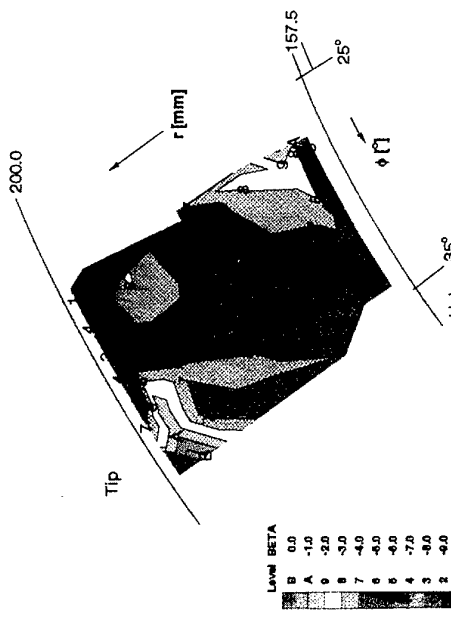
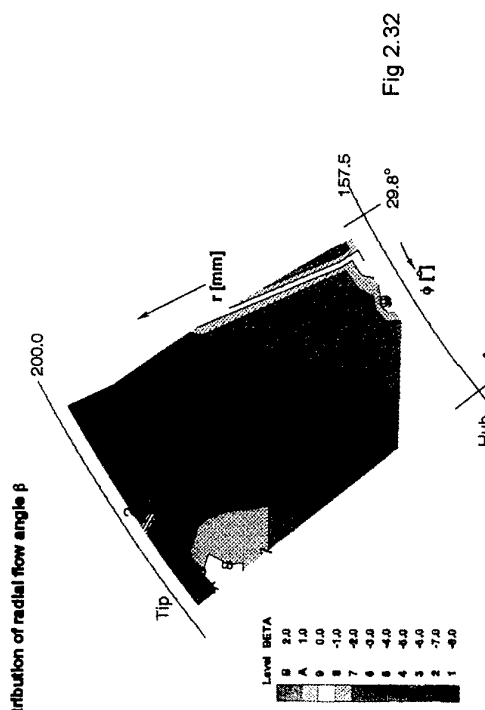
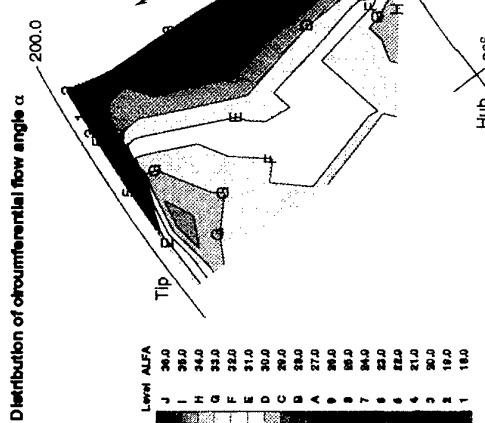
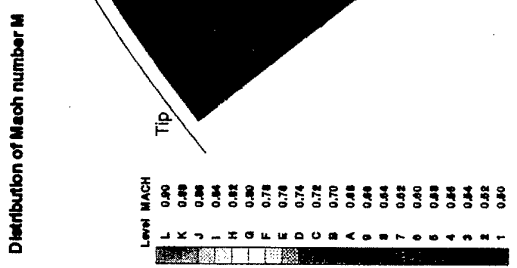
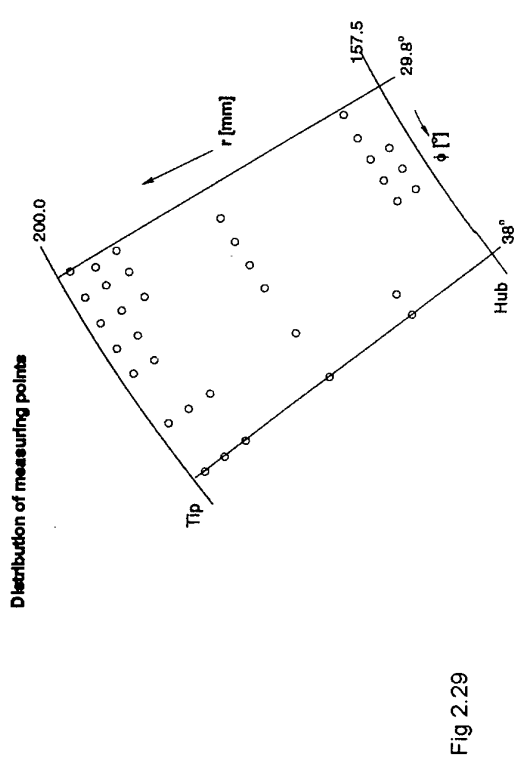


Fig 2.28



### Results of the 3D-L2F measurements at MP1





## Chapter 3

### THE COMPUTATIONS

#### 3.1 INTRODUCTION

The members of the Working Group invited research workers to undertake computations of the test cases using any 3D RANS codes they wished to use. Computations using fifteen different codes were supplied to the WG, in some cases with a range of grids and turbulence models. All the codes solved the steady flow RANS equations. Most of the computations were undertaken specifically for the WG. Some solutions obtained earlier (perhaps as a result of ASME's use of Rotor 37 as a test case) were also provided. Not all the codes in common use in industry were included, but all the important types were represented. In all, a wide range of grids and turbulence models were employed.

Tables 3.1 and 3.2 give details of the codes used. These details are collected in this way for reference purposes, but in the analysis sections of this chapter specific details considered to be of particular importance are repeated.

As both test cases involved only an isolated blade row, the question of how to "average" or otherwise to model in a steady code the unsteady aerodynamic interference between adjacent blade rows did not arise in the present study. The WG recognises this as a key issue to be addressed at a later date, when unsteady codes have become established.

#### 3.2 THE RESULTS FOR ROTOR 37

##### 3.2.1 Computations requested

In 1993, The ASME Turbomachinery Committee invited research workers to predict, using RANS codes, the overall mass flow range, pressure ratio, temperature ratio, and efficiency of Rotor 37 at design speed, and also to predict at both 92.5% and 98% of the choked flow the spanwise distribution of pitchwise-mean pressure ratio, temperature ratio, and efficiency. (Only the geometric data not the flow measurements were provided at that time, but contributors to the present study also had the measurements.) These same parameters were also specified to the WG; but in addition contributors were also asked to provide certain parameters in the form of contour plots to enable a thorough analysis to be undertaken.

The overall performance predictions and the pitchwise-mean traverse predictions at 98% of the choked flow are shown in Figs 3.1-3.5 in comparison with the measurements. (Relatively little attention was given to the stall point results.) Owing to the enormous volume of the three-dimensional results, only selected plots will be shown to illustrate specific points in the analysis.

##### 3.2.2 Flow description

This description of the flow is based on published results. Denton (1996) has given a good global analysis of the flow in this compressor. Chima (1996b) and Suder and Celestina (1996) analysed the tip leakage flow, and Hah-Loellbach (1997) and Shabbir et al (1997) analysed the hub corner flow.

Three regions are considered: the mid-span, the hub wall and the tip wall regions.

- (1) The mid-span region is dominated by a strong shock attached at the blade leading edge. This shock interacts strongly with the suction side boundary layer. The

boundary layer after the shock may separate either up to the trailing edge according to some authors, or reattach before the trailing edge. A strong radial movement is also observed in the separated area from the hub to the tip wall, as for example in Fig 3.6.

- (2) Near the hub wall, the measurements of absolute stagnation pressure  $P_0$  at station 4 show a region of low pressure at 20% of the blade span, for both 98% and 92% of the choked mass flow. Strazisar has pointed out that this pressure deficit is present over a wide range of mass flow for the nominal speed of rotation (Fig.3.7). He mentions also that the stagnation temperature distribution  $T_0$ , deduced from the Euler energy equation, shows the same trend at station 3 immediately downstream of the rotor trailing edge. This indicates that the spanwise character of the  $P_0$  distribution is not an artifact of the radial mixing.

There are strong indications that a corner stall occurs near the suction side corner (Fig.3.8). This corner stall greatly reduces the axial momentum in the region of the stagnation pressure deficit near the hub (Fig.3.9). The axial momentum is then redistributed all over the blade span, thereby reducing the amount of the blade work, and therefore the overall pressure ratio.

This corner stall seems mainly influenced by the supersonic Mach number ahead of the leading edge, in the hub region. Both experiments and simulations do not show the strong  $P_0$  deficit if they are performed with a lower subsonic Mach number ahead of the hub leading edge (Shabbir et al., 1997, Hah, Loellbach, 1997). This stall may be partially due to the glancing side wall shock wave interaction with the hub boundary layer, as shown in Fig 14 of Povinelli (1997).

- Two other effects have a very important influence:
- A change of the overall mass flow at the nominal speed strongly modifies the radial  $P_0$  distribution over the whole blade span. As the mass flow is reduced, the  $T_0$  deficit is always present at the hub, while the  $P_0$  deficit is slightly smeared out for the highest mass flow (Fig. 3.7.)
  - A possible leakage flow occurs through the axial gap between the non-rotating upstream hub and the rotor (Fig.3.9). Shabbir et al (1997) report experiments and CFD studies on the effect of modifying the upstream axial gap between the non-rotating hub and the rotor. All these studies show an increase of the stagnation pressure downstream near the hub, with a reduction of the upstream axial gap. Their simulations show a deficit of stagnation pressure at 20% from the hub in agreement with the experimental observations. More important, the simulations shows this deficit, either with a very low leakage mass flow introduced of the order of 0.25 to 0.33% of the choking mass flow, or even when there is no net mass flow through a gap connected with a blind cavity. For this last configuration, the upstream wave of the leading edge shock could drive a circumferential inflow/outflow pattern through the upstream gap. Most of the CFD simulations have neglected this upstream gap. Their

Table 3.1a Code information for Rotor 37 case

AUTHOR AFFILIATION CODE	MODEL EQ. and APPROACH	TURBULENCE MODEL	BOUNDARY CONDITIONS (inlet, outlet walls, periodic boundaries)	SPACE/TIME DISCRETIZATION and CONVERGENCE,ACCELERATION	INITIAL SOLUTION and CONVERGENCE	MEMORY REQUIREMENT and CPU TIME
A.ARNONE (Univ.of Florence) TRAFF3D	3D/RANS Time marching	Baldwin-Lomax $C_{w\infty}=1.0$	<ul style="list-style-type: none"> <li><math>P_t, T_t</math>, and flow angles specified</li> <li><math>P_s</math> extrapolated from the interior points, no-slip condition and temperature condition</li> <li>phantom cells at periodic boundaries</li> </ul>	Finite volume. Explicit time integration. Local time stepping, residual smoothing, multigrid and grid refinement.	Averaged RMS of residuals $< 10^{-7}$	234 MB for 800K grid points. Near 18h on IBM RISC/6000 mod.590
J.CALVERT (DERA) TRANSCode	3D/RANS Time marching	(a)Baldwin-Lomax $C_{w\infty}=1.0$ (b) Spalart-Allmaras	<ul style="list-style-type: none"> <li><math>P_t, T_t</math>, swirl velocity and radial flow angle specified</li> <li>Hub or tip <math>P_s</math> specified and simple radial equilibrium</li> <li>No slip condition</li> <li>No special treatment</li> </ul>	Cell centred finite-volume time marching; 2 or 4 stage Runge-Kutta solution. Local time-stepping, implicit residual smoothing and multigrid. Nominally second order accurate	Static pressure assumed to vary linearly with axial distance through the blade. Residual is the imbalance in the axial momentum equation on the fine grid. Mass conservation: typically maximum error $< 0.29\%$ and inlet to outlet error $< 0.029\%$ .	280 bytes/grid point (single precision). 10h 37m for 1000 time steps and 324K grid points, using DEC 3000-700 (spec FP92<230) (approx. 40% longer for db).
R.V.CHIMA (NASA Lewis) SWIFT	3D Thin Layer NS Time marching	Baldwin-Lomax $C_{\text{cp}}=1.216$ $C_{\text{ns}}=0.646$	<ul style="list-style-type: none"> <li><math>P_t, T_t</math>, swirl velocity and meridional flow angle specified</li> <li>hub <math>P_s</math> and radial equilibrium</li> <li>Overlap by one grid point at periodic boundaries.</li> </ul>	2nd order cell vertex finite-difference formulation. 4-stage Runge-Kutta time integration scheme. Spatially-varying $\Delta t$ and implicit residual smoothing with variable coefficients	Maximum and rms residuals reduced by 2 - 2½ decades	30 words/grid point. 4.1h on Cray C90 for 1057K grid points for most cases and 8.2h near stall.
V.COULAILIER (ONERA) CANAR	3D/RANS Time marching	(a) Michel (b) Baldwin-Lomax (c) Jones-Launder low Re $K_{\infty}$ (d) Spalart-Allmaras	<ul style="list-style-type: none"> <li><math>P_t, T_t</math>, and flow angles specified</li> <li><math>P_s</math> and simple radial equilibrium</li> <li><math>P_s</math> extrapolated to walls</li> <li>mesh interpolation</li> </ul>	Cell centered finite volume and four step Runge-Kutta time integration. Local time-stepping and multigrid Lerat's Implicit Spectral Radius method	Rms residuals reduced by 1.5 to 2 decades Continuity error $< 0.5\%$	60-65 words/grid point, 21-32 us/iter/grid point, on Cray YMP
J.D.DENTON (Cambridge Univ) TIP3D	3D Thin Layer NS Time marching	mixing length	<ul style="list-style-type: none"> <li><math>P_t, T_t</math>, and flow angles specified</li> <li><math>P_s</math> at tip and simple radial equilibrium</li> </ul>	Cell vertex finite volume. Local time-stepping with multigrid	Rms residuals reduced by 2½ decades Continuity error $< 0.5\%$	36 $\mu$ s/grid point/step on IBM RISC/6000 mod.350
C.HAH (NASA Lewis) HAH3D	3D/RANS Relaxation	Chien low Re $k-\epsilon$	<ul style="list-style-type: none"> <li><math>P_t, T_t</math>, angles, turbulent k-e specified</li> <li><math>P_s</math> at shroud</li> </ul>	Finite volume. Pressure based	Integrated residuals reduced by 4 decades	25 words/grid point. 2h on Cray YMP

$P_t$  = total pressure,  $P_s$  = static pressure,  $T_t$  = total temperature

Table 3.1.a Code information for Rotor 37 case (continued)

AUTHOR AFFILIATION CODE	MODEL EQ. and APPROACH	TURBULENCE MODEL	BOUNDARY CONDITIONS (inlet, outlet, walls, periodic boundaries)	SPACE/TIME DISCRETIZATION and CONVERGENCE ACCELERATION	INITIAL SOLUTION and CONVERGENCE	MEMORY REQUIREMENT and CPU TIME
T.HILDEBRANDT (I.S.A.) and T.VOGEL (DLR) TRACE-S	3D/RANS Time marching	standard k-ε wall functions	<ul style="list-style-type: none"> <li><math>P_t, T_t</math> and flow angles specified</li> <li><math>P_s</math> specified, density and velocities extrapolated</li> <li>No slip condition and static pressure extrapolated</li> <li>No special treatment</li> </ul>	Finite volume, cell centered scheme with second and fourth order eigenvalue scaled damping. Explicit time marching Runge-Kutta scheme. Implicit residual smoothing, multigrid and local time stepping	Start with zero flow Max and rms density residuals reduced by 5 decades Rms k and $\epsilon$ residuals reduced by 8 decades	300 bytes/point approx. (s.p.) 10h on IBM RS6000 (72k). 1h on NEC SX4 (250 kpoint). 2h on NEC SX4 (500 kpoint).
T.HILDEBRANDT (I.S.A) TASCFLOW	3D/RANS Pressure based method	standard k-ε wall functions	<ul style="list-style-type: none"> <li><math>P_t, T_t</math> and flow angles specified</li> <li>Specified mass flow (below 0.99 choke) or average static pressure</li> <li>No slip condition</li> <li>Periodic</li> </ul>	Finite element based finite volume method. Upwind, implicit, ILU-matrix factorization. Multigrid. The spatial discretization is second order accurate.	Normalised RMS residuals of order 5E-07. Normalised global balances (in-out) approx. 1E-05.	1000 bytes/point approx. (s.p.), 20h on IBM RS6000 (72 kpoint)
M.IVANOVICH and B.HUTCHINSON (Adv. Sci Comp.) TASCFLOW	3D/RANS Pressure based method	standard k-ε wall functions	<ul style="list-style-type: none"> <li><math>P_t, T_t</math> and flow angles specified</li> <li>Specified mass flow (below 0.99 choke) or average static pressure</li> <li>No slip condition</li> <li>Periodic</li> </ul>	Finite element based finite volume method. Upwind, implicit, ILU-matrix factorization. Multigrid. The spatial discretization is second order accurate.	Normalised RMS residuals of order 5E-07. Normalised global balances (in-out) approx. 1E-05.	9-10h for 100K grid points on an IBM 3BT workstation and 28h for 250K grid.
S.KANG and C.HIRSCH (Vrije Univ.Bрюссел) EURANUS/TURBO	3D/RANS Time marching	Baldwin-Lomax $C_{\alpha\alpha}=1.0$	<ul style="list-style-type: none"> <li><math>P_t, T_t</math> and flow angles specified</li> <li>Radial equilibrium condition</li> <li>No slip condition and adiabatic solid walls.</li> </ul>	Finite volume second order centered scheme with 2nd and 4th order artificial dissipation terms and a W cycle multigrid technique. Five stage Runge-Kutta scheme. Local time stepping and implicit residual smoothing.	Computations converged to about 2.0-2.5 orders of residual reduction and constancy of mass flow. The error in mass flow between inlet and outlet <0.1%.	
S.MCNULTY (Allison) ADPAC	3D/RANS Time marching	Baldwin-Lomax	<ul style="list-style-type: none"> <li><math>P_t, T_t</math> and flow angles specified</li> <li>Hub or tip <math>P_s</math> and simple radial equilibrium</li> </ul>	Finite volume, 4-stage Runge-Kutta time marching scheme. Local time stepping, implicit residual smoothing, and multigrid.	Uniform flow at inlet total pressure, total temperature and Mach number. Convergence was assumed when flow, pressure ratio and efficiency varied less than a specified tolerance between time steps. Mass flow variation between inlet and exit planes <0.1%.	28 MW required for 412,000 mesh points with 3 levels of multigrid. 1.4h for convergence on 412,000 point mesh.
C.SHABBIR and M.CELESTINA (NASA Lewis) VSTAGE	3D/RANS Time marching	(a) Baldwin-Lomax, $C_{\alpha\alpha}=1.0$ (b) SKE (Lauder-Spalding k-ε) (c) CKE (Shih k-ε)	<ul style="list-style-type: none"> <li><math>P_t, T_t</math> and flow angles specified</li> <li><math>P_s</math> and simple radial equilibrium</li> <li><math>k, \epsilon</math> gradients zero</li> <li>Lander wall boundary conditions for <math>k, \epsilon</math></li> </ul>	Finite volume. Explicit Runge-Kutta	maximum and rms density residuals reduced by 2 decades Continuity error < 0.017%	72.4 words/point. 15 μs/iter/point.
K.WEBER (Allison) OVERFLOW	3D/RANS Time marching	Spalart-Almaras with Deltas modification	<ul style="list-style-type: none"> <li><math>P_t, T_t</math> flow angles specified hub <math>P_s</math> and simple radial equilibrium</li> </ul>	Second order Roe upwind scheme	residuals reduced by 3 decades	16 MW for H-O-H grid 25 MW for overset O-H grid

Table 3.1 b Code information for DLR cascade case

AUTHOR AFFILIATION CODE	MODEL EQ. and APPROACH	TURBULENCE MODEL	BOUNDARY CONDITIONS (inlet, outlet, walls, periodic boundaries)	SPACE/TIME DISCRETIZATION and CONVERGENCE/ACCELERATION	INITIAL SOLUTION and CONVERGENCE	MEMORY REQUIREMENT and CPU TIME
F.BASSI (Ancona Univ) M.SAVINI (Bergamo Univ)	3D/RANS Time marching	Wilcox $k-\omega$	<ul style="list-style-type: none"> <li>enthalpy, entropy, angles, <math>k</math>, <math>\mu</math></li> <li>specified <math>P_s</math> and simple radial equilibrium</li> </ul>	Finite volume, cell-centered. Initially multigrid, then simple grid to convergence	2D at mid-span, zero velocity. Aims at 5 decades reduction of time derivatives of density	104 words/point 2.3E-4 sec/cycle/point on HP 735
R.V.CHIAMA (NASA Lewis) RVC3CD	3D/RANS Time marching	Baldwin-Lomax $C_{\alpha} = 1.216$ $C_{Re} = 0.646$	<ul style="list-style-type: none"> <li><math>P_t</math>, <math>T_t</math>, angles specified</li> <li>hub <math>P_\bullet</math> and simple radial equilibrium</li> </ul>	Thin-layer Navier-Stokes, finite difference, Runge-Kutta implicit residual smoothing	max and min residuals reduced by $2\frac{1}{2}$ to 3 decades Continuity error < 0.5%	Cray C-90 1.75 hours 14.3 Mwords storage
V.COQUAILLER (ONERA) CANARI	as for Rotor 37				RMS residuals reduced by 2 - 2½ decades	60-65 words/point, 21-32.1s/iter/point.
S.DADONE and P.DE PALMA (Bari Poly)	3D/RANS Time marching	Baldwin-Lomax Degani-Schiff modification	<ul style="list-style-type: none"> <li><math>P_t</math>, enthalpy, angles specified</li> <li><math>P_\bullet</math> and simple radial equilibrium</li> <li><math>P_\bullet</math> extrapolated to walls</li> </ul>	Finite volume, Runge-Kutta, Roe's flux difference splitting, Fully upwind 2nd order accurate MUSCL extrapolation	2D at midspan Continuity error < 0.5%	550 bytes/point 80 hours for 12000 cycles on Apollo 9000
J.D.DENTON (Cambridge Univ) TIP3D	as for Rotor 37					
C.HAH (NASA Lewis) HAH3D	as for Rotor 37					
S.LISIEWICZ (DLR) TRACE-S	3D/RANS Time marching	<ul style="list-style-type: none"> <li>standard <math>k-\varepsilon</math> (Lauder-Spalding)</li> <li>extended <math>k-\varepsilon</math> (Kato-Launder)</li> <li>Wilcox <math>k-\omega</math></li> <li>Spalart-Allmaras</li> </ul>	<ul style="list-style-type: none"> <li>Farfield non reflecting or standard inflow conditions.</li> <li>Farfield non reflecting or standard outflow conditions.</li> <li>Assuming zero pressure gradient define fluxes and velocities to zero.</li> </ul>	Finite volume, cell centered scheme with second and fourth order eigenvalue scaled damping. Explicit time marching Runge-Kutta scheme. Implicit residual smoothing, multigrid and local time stepping	Zero flow, prescribing constant flow quantities Maximum residual in density reduced up to 6 decades, averaged residual reduced up to ten decades (machine accuracy).	443 bytes/point. 5h on NEC SX-3 for 350K grid points.
F.MARTELLI (Florence Univ) FLOS3D	3D/RANS Time marching	Wilcox $k-\omega$	<ul style="list-style-type: none"> <li><math>P_t</math>, <math>T_t</math>, angles specified</li> <li>Hub <math>P_\bullet</math> with no-averaged radial equilibrium</li> <li>No slip condition</li> <li>Periodic fluxes and flow variables</li> </ul>	Finite central difference scheme with artificial smoothing terms. Implicit time-marching, approximate factorisation	Linear pressure distribution from inlet to exit Residuals reduced by 2.5 to 3 decades	
S.MCNULTY (Allison) ADPAC	as for Rotor 37					
A.W.STAPLETON (DERA) TRANSCode	as for Rotor 37 (Calvert)					

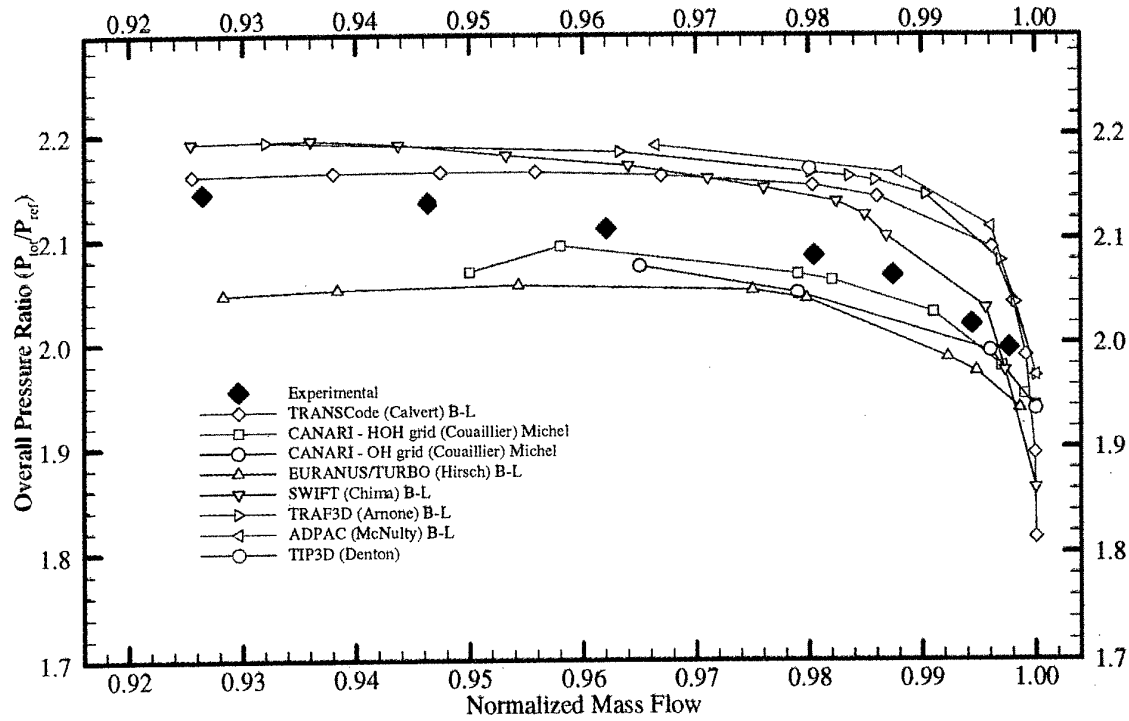
Table 3.2 Grid information

Contributor (code)	Case	Grid type	Grid size ( $x_0, l$ )	grid points	radial $y^+$ at wall	radial max spacing %H	radial min spacing %H	pitchwise max spacing %P	pitchwise min spacing %P	chordwise max spacing %C	chordwise min spacing %C	clustering	i.e. points	t.e. points	points in tip gap	max aspect ratio	max skew deg	no blocks	min x (m)	max x (m)	
Amone (TRAF3D)	R37	non-periodic C	285x3x57	800,565	NA	3	0.05	1	NA	0.01	NA	0.12	max cell to cell = 1.3	10	2	6	NA	NA	1	NA	NA
Bassi-Savini	DLR	periodic C	161x25x31	124,775	15	13	0.18	3	12	0.017	3.1	0.58	1.38H1.28P1.18C	10	7	0	194.1	43.8	1	NA	NA
Calvert (TRANSCode)	R37	sheared periodic H	241x37x45	401,265	7.5	10	0.08	2.25	11	0.011	2	0.39	1.26H1.17P1.12C	15	11	0	193.3	40	1	NA	NA
Chima (SWIFT)	R37	periodic H-C-O	151x45x49	362,551	5/25	3.89	0.103	5/25	3.51	0.117	1.67	0.182	max cell to cell =1.3	5	5	4	84	69	1	-0.0419	0.1067
Chima (RVC3CD)	DLR	periodic C	165x45x63	478,170	2/4	14.1	0.01	2/4	1.8	0.01	1.8 (C)	0.01 (C)	tanh	25	10	13	1410	60	3	-0.0419	0.1067
Couailler (CANARI)	R37	non-periodic H-O-H	O:221x41x69	821,459	1/8	6.52	0.094	0.5/3.5	1.6	0.011	1.29	0.027	1.15 (P), 1.303 (R)	15	15	11	146.24	28.32	5	NA	NA
			H:192x25x69																		
			O:221x41x69																		
			H:192x25x69																		
			O:189x7x11																		
			H:101x11x11																		
			O-H	577,042	0.5/8	6.187	0.015	0.5/4	1.1	0.016	2.315	0.035	1.25 (P), 1.278 (R)	15	15	11	259.89	35.27	4	NA	NA
			O:189x25x69																		
			H:155x21x69																		
			O:189x7x11																		
			H:183x13x11																		
			O:189x35x69	725,084	0.5/8	6.187	0.015	0.5/1.5	0.49	0.0034	2.315	0.035	1.20 (P), 1.278 (R)	15	15	11	870.04	35.41	4	NA	NA
			H:155x21x69																		
			O:189x15x11																		
			H:183x13x11																		
Dadone, DePalma (NIP3D)	DLR	non-periodic H-O-H	O:183x41x69	659,157	0.277.5	8.1	0.024	0.2/7.27	3.3	0.024	3.455	0.14	1.12 (P), 1.192(R)	15	15	0	276.29	60.17	3	NA	NA
Dadone, DePalma (NIP3D)	DLR	periodic C	H:65x25x69	124,775	15	13	0.18	3	12	0.017	3.1	0.58	1.38H1.28P1.18C	10	7	0	194.1	43.8	1	NA	NA
Denton (NIP3D)	R37	sheared periodic H	150x37x37	205,350	NA	5.3	0.12	NA	3.23	0.32	1.21	0.48	max cell to cell =1.4	3	NA	3	82	83	1	NA	NA
DLR	sheared periodic H	125x40x40	200,000	NA	4.82	0.19	NA	3.13	0.13	1.76	0.20	max cell to cell =1.3	22	NA	0	33	85	1	NA	NA	

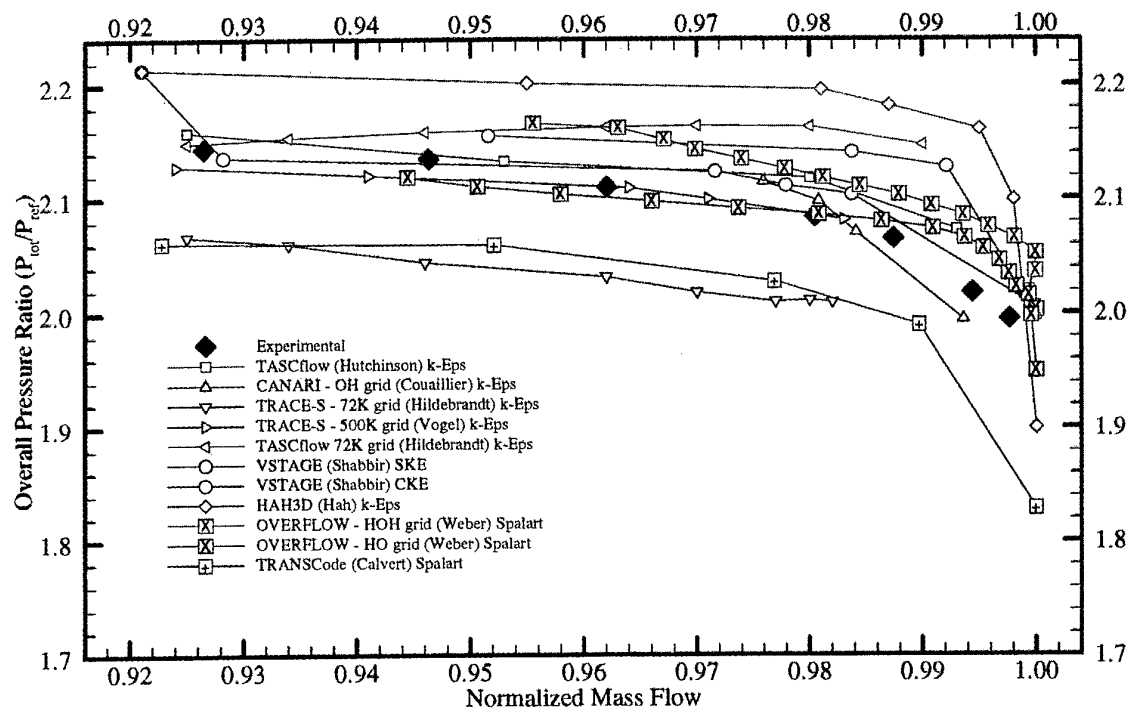
**Table 3.2** Grid information (continued)

Table 3.2 Grid information (continued)

Contributor (code)	Case	Grid type	Grid Size (x,y,r)	grid points	radial y+ at wall	radial max spacing %H	pitchwise max spacing %H	y+ at wall max spacing %P	pitchwise max spacing %P	chordwise max spacing %C	clustering	i.e. points t.e. points	points in tip gap	max aspect ratio	max skew deg	no blocks	min x (m)	max x (m)			
Marielli (FLOSSD)	DLR	non-periodic H	201x63x61	772,443	NA	NA	NA	NA	NA	NA	NA	1.13 (1e-)	16	0	57.13	75	8	NA	NA		
McNulty (ADPAC)	DLR	C (non-contiguous along wake)	193x33x25	159,225	NA	NA	NA	NA	NA	NA	NA	1.16 (1e-)	13	5	0	NA	1	NA	NA		
			193x33x49	312,081	NA	NA	NA	NA	NA	NA	NA	NA	13	5	0	NA	1	NA	NA		
			385x65x49	1,226,295	NA	NA	NA	NA	NA	NA	NA	NA	26	10	0	NA	1	NA	NA		
R37	H-O-H		H:25x17x41 O:145x25x41 H:25x17x41 tip gap O:145x9x9	194,950	NA	NA	NA	NA	NA	NA	NA	NA	6	6	9	86.3	NA	4	NA		
			H:25x25x49 O:201x33x49 H:25x3x49 tip gap O:201x9x9	412,348	NA	NA	NA	NA	NA	NA	NA	NA	6	6	9	86.3	NA	4	NA		
			H:25x17x73 O:145x25x73 H:25x17x73 tip gap O:145x9x9	338,420	NA	NA	NA	NA	NA	NA	NA	NA	6	6	9	86.3	NA	4	NA		
Shabbir/ Zhu Celestina (VSTAGE)	R37	sheared periodic H	132x41x51	276,012	20,30	2.82	0.036	15.25	10	0.83	8.55	0.268	1.2	6	6	3	98	60	1	NA	
Stapleton (TRANSCode)	DLR	sheared periodic H	135x48x49	324,135	3,17,5	3.5	0.118	10,16,0	3.5	0.118	2.1	0.115	max cell to cell =1.3	22	13	0	122.2	86.5	1	-0.356	0.08
			135x49x117	773,955	0.02,0.2	2.2	0.00143	10,16,0	3.5	0.118	2.1	0.115	max cell to cell =1.3	22	13	0	9942	86.5	1	-0.356	0.08
			167x73x73	889,943	0.5,6,0	2.5	0.0292	0.2,5,2	2.5	0.0292	1.7	0.1761	max cell to cell =1.25	20	11	0	273.1	85.4	1	-0.356	0.08
Weber (OVERFLOW)	R37	O embedded in H	H:181x49x67	855,427	hub 24-50 shroud 14-40	5,3	0.14	2.5-13	1.47	0.0266	4.1	0.32	tanh for O =1.27	13	11	7	433.3	25	3	NA	NA
			H:41x33x47 O:159x23x47 tip gap O:159x15x7	497,334	hub 26-50 shroud 14-40	5,8	0.14	2-16	2.94	0.0260	2.7	0.32	tanh	11	9	7	567.2	NA	4	NA	NA

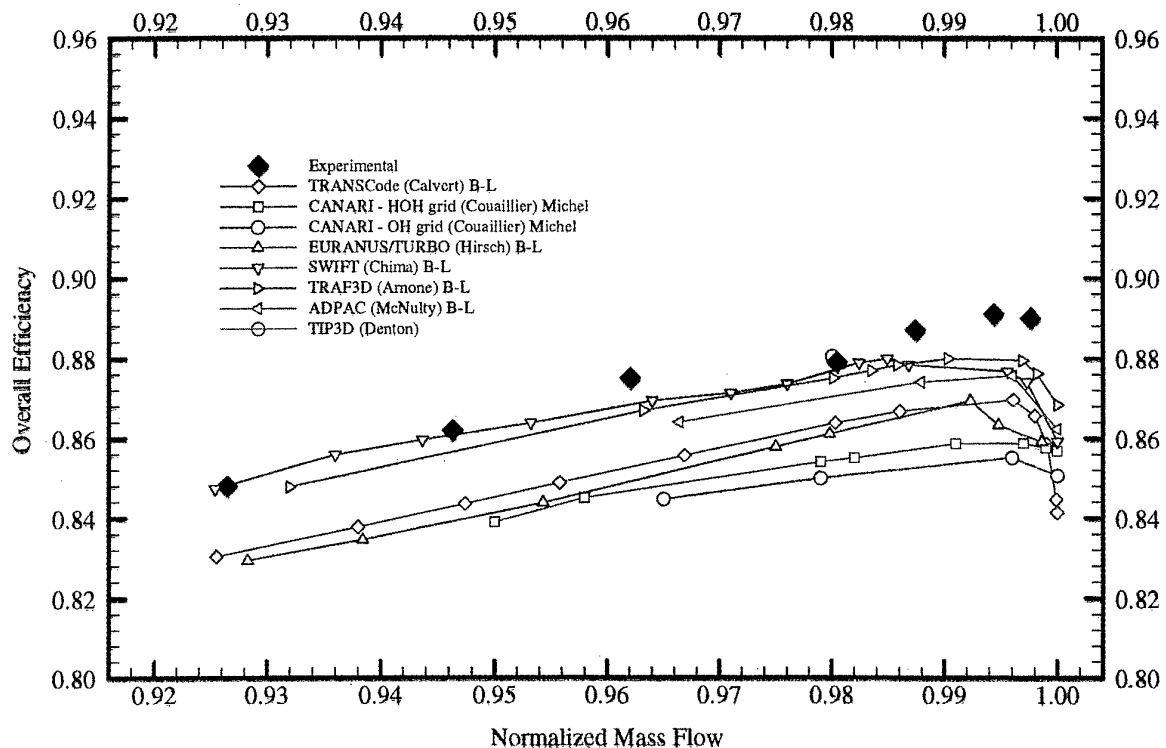


(a) algebraic / mixing length turbulence models

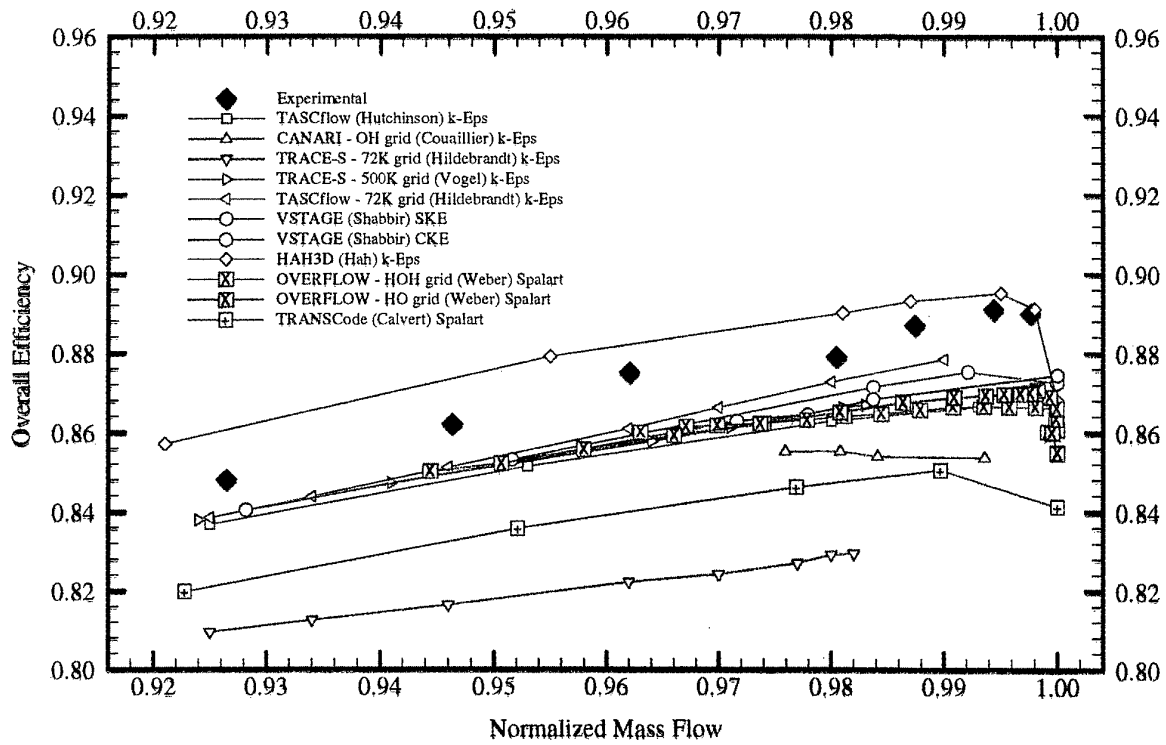


(b) turbulent transport models

Fig 3.1 Rotor 37: overall pressure ratio

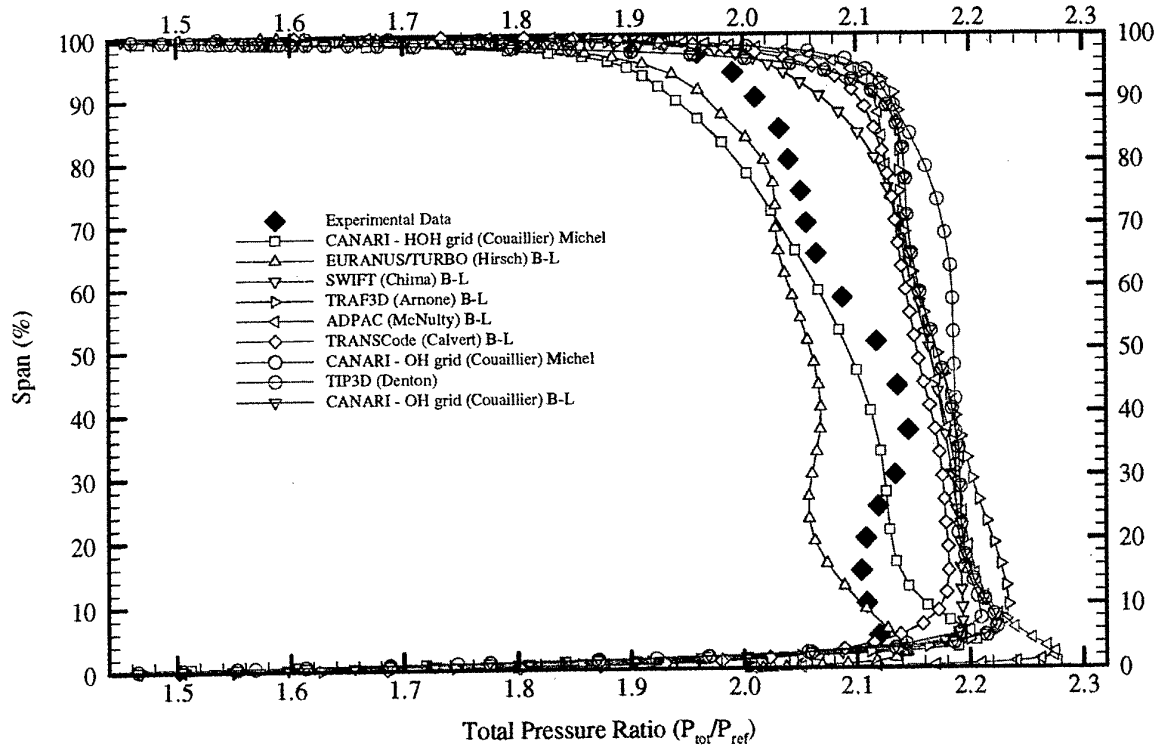


(a) algebraic / mixing length turbulence models

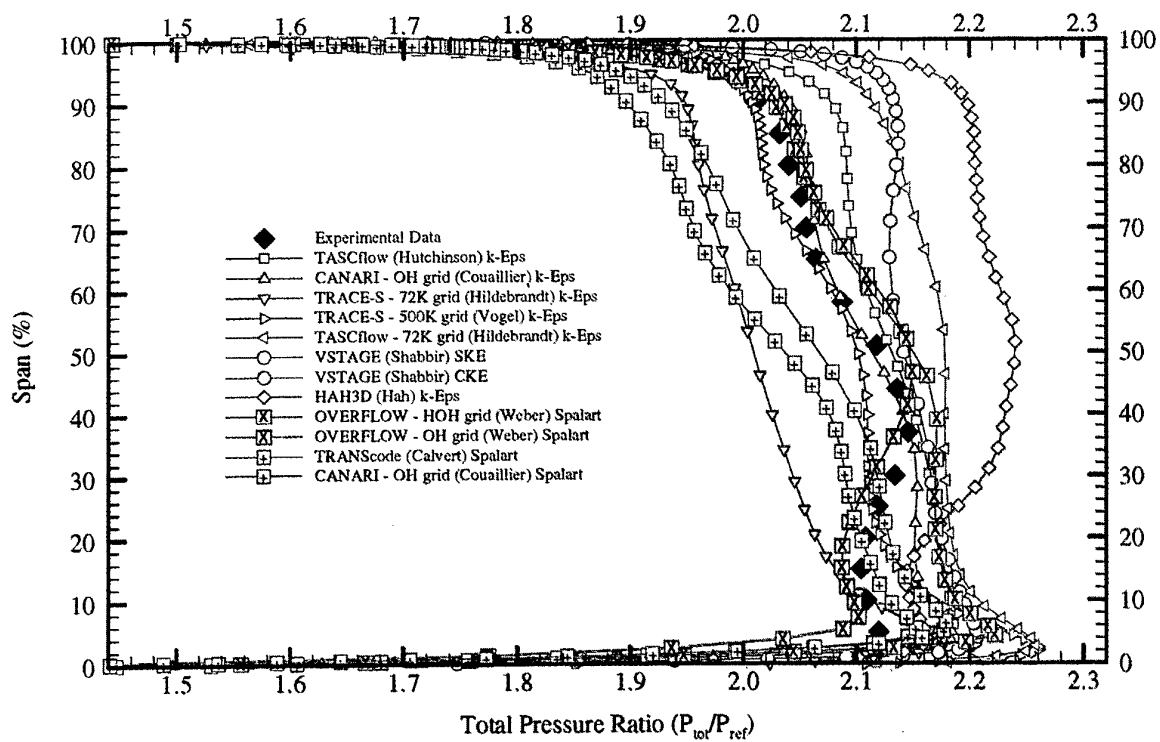


(b) turbulent transport models

Fig 3.2 Rotor 37 overall efficiency

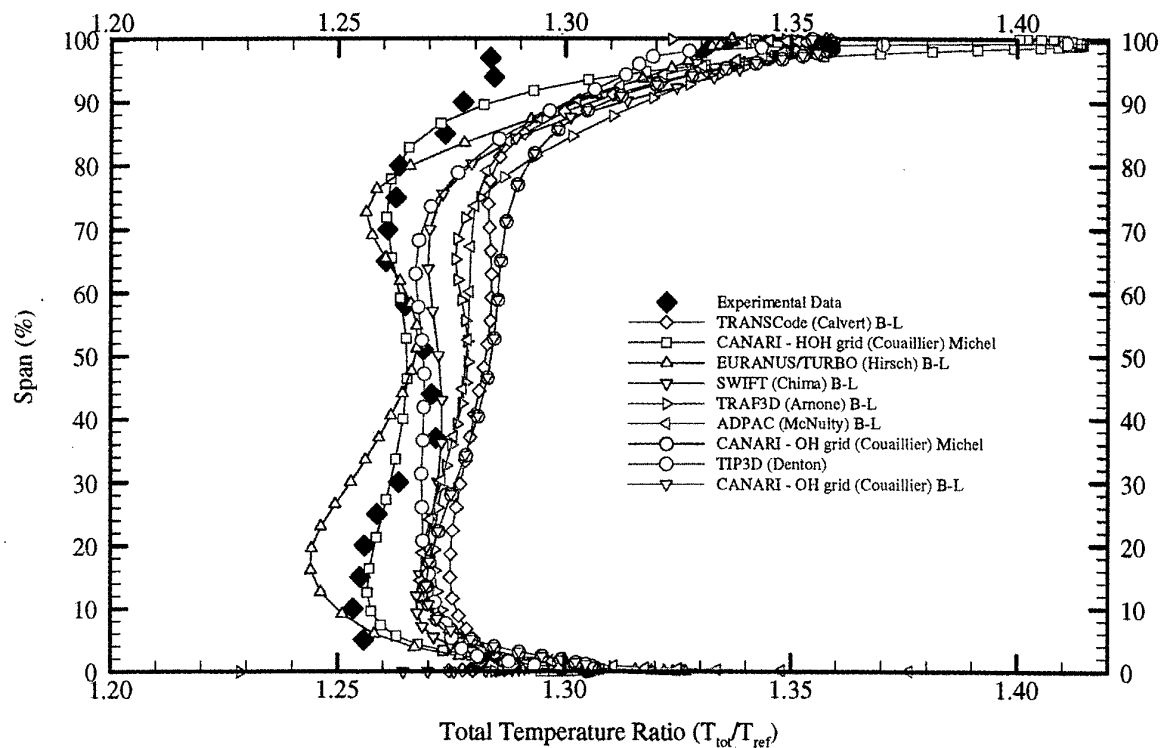


(a) algebraic / mixing length turbulence models

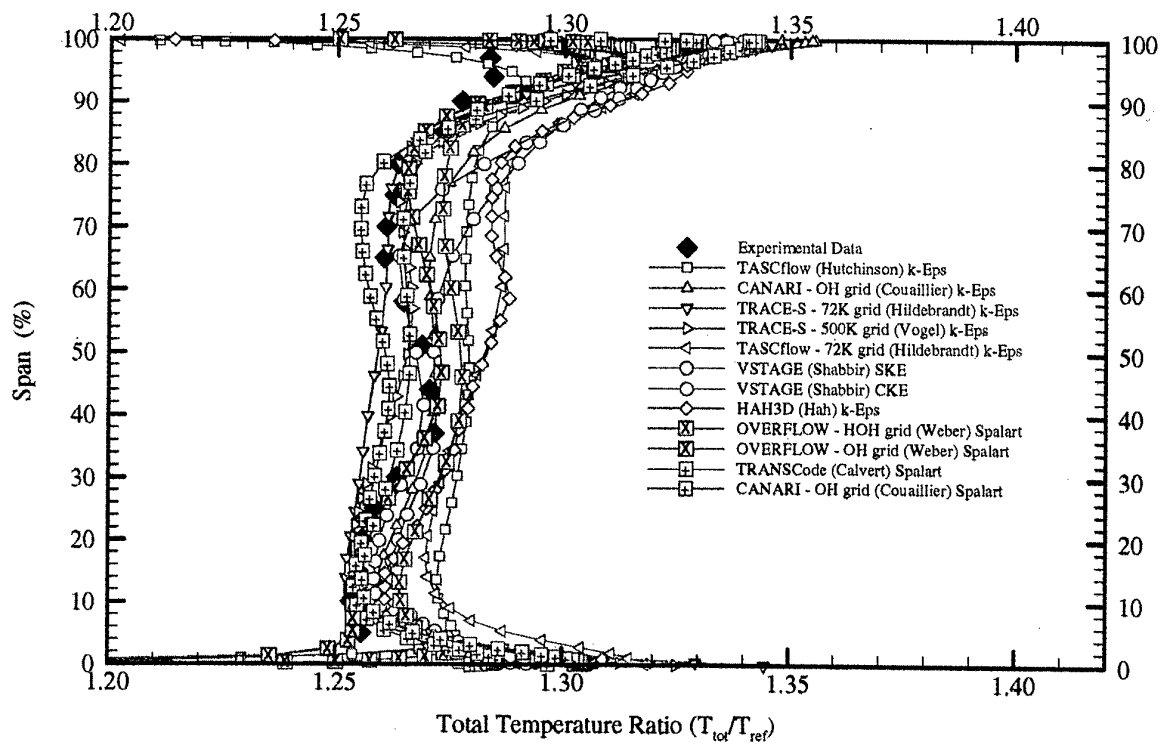


(b) turbulent transport models

Fig 3.3 Rotor 37 total pressure ratio

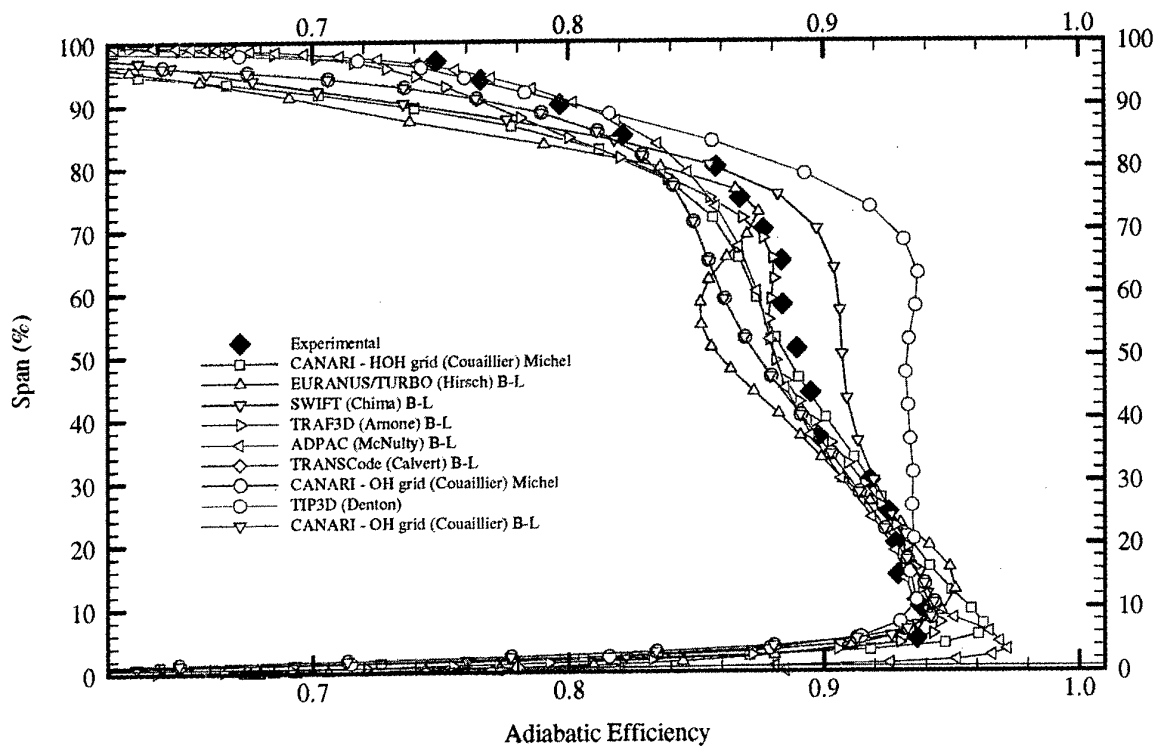


(a) algebraic / mixing length turbulence models

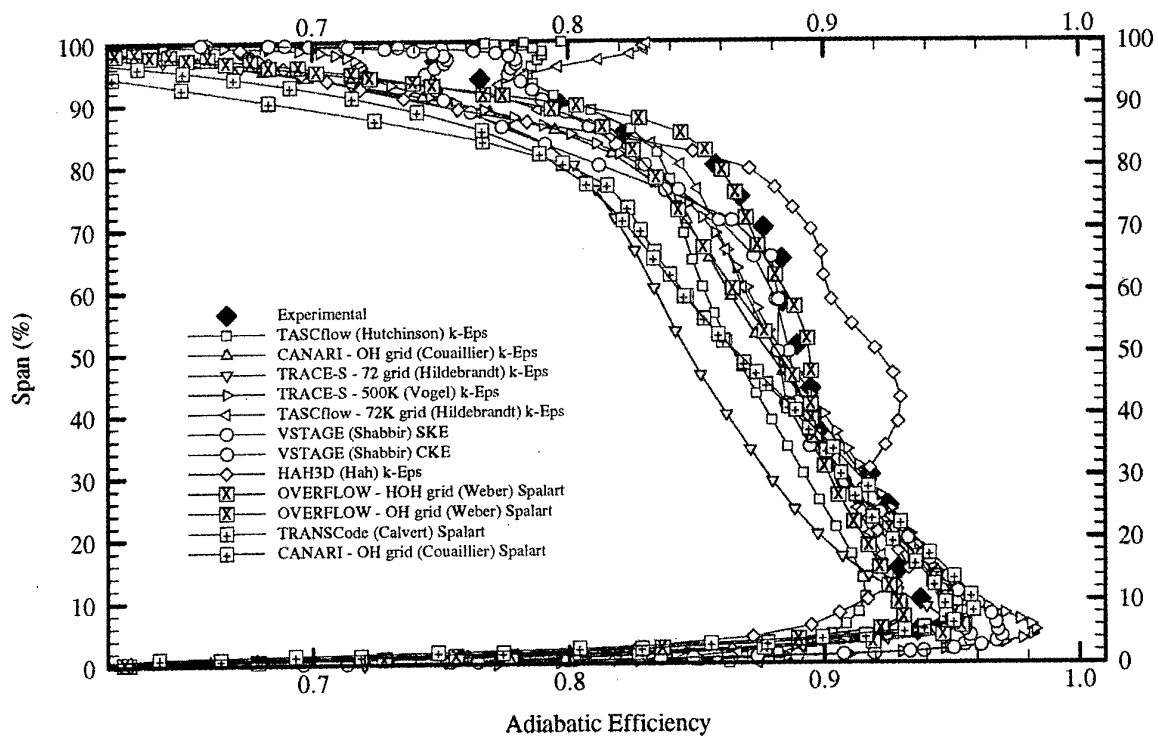


(b) turbulent transport models

Fig 3.4 Rotor 37: total temperature ratio



(a) algebraic / mixing length turbulence models



(b) turbulent transport models

Fig 3.5 Rotor 37 efficiency

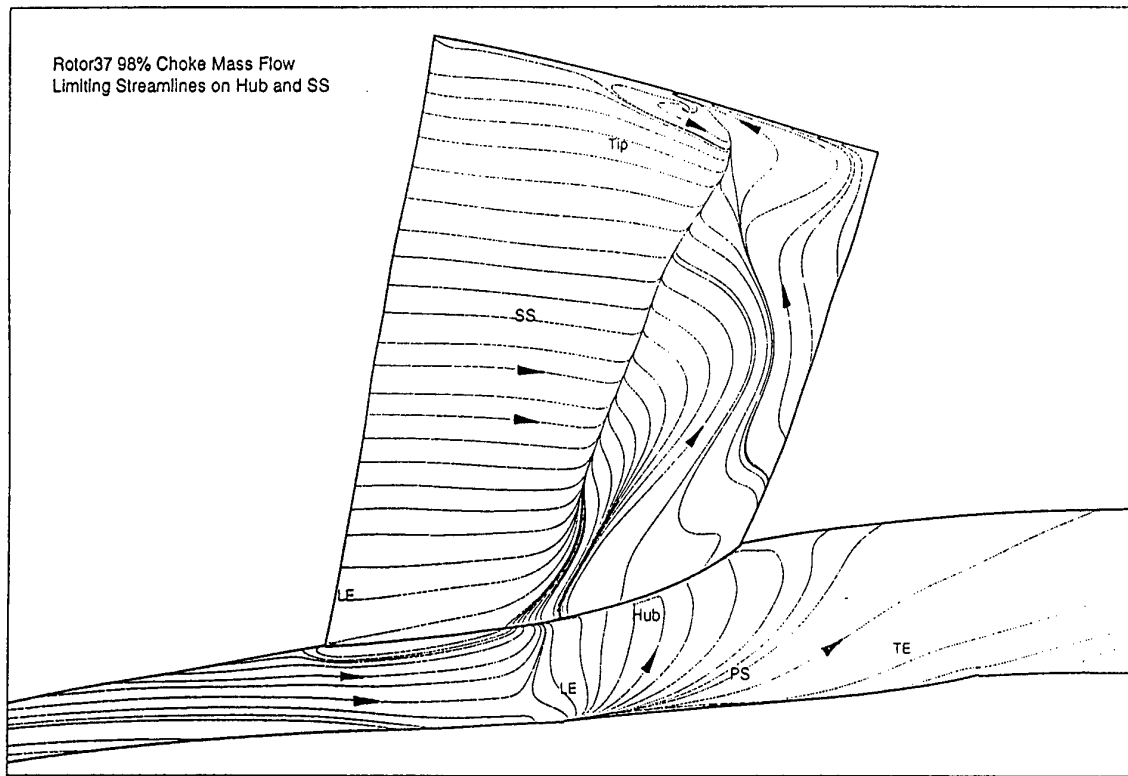


Fig 3.6 Limiting streamlines, showing hub corner stall (Kang)

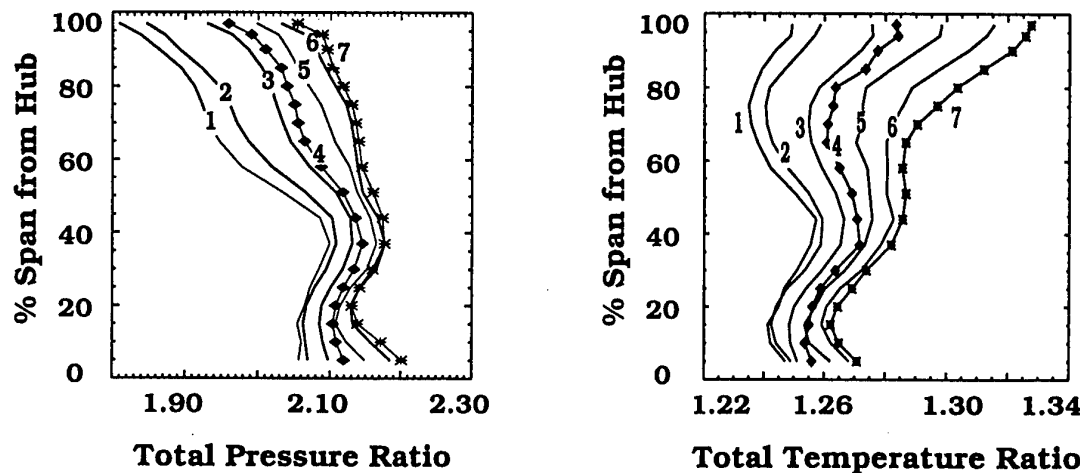


Fig 3.7 Sensitivity of performance to mass flow (1 is the highest flow and 7 the lowest flow)

overprediction of  $P_o$  in the hub region, and all over the blade span, is also consistent with hub leakage flow influences.

- (3) The tip wall region is dominated by a strong tip leakage flow. Chima (1996b) and Suder and Celestina (1996) have presented some detailed CFD results for the flow in this region. Detailed experimental results and analysis have also been given by Suder and Celestina. The main conclusions of these studies are:
- (a) The leakage flow issuing from the suction side, upstream of the passage shock, behaves almost as an

inviscid jet owing to a strong supersonic expansion (Fig. 3.10).

- (b) The limiting surface between the tip leakage jet and the main crossflow is a region of strong shear, owing to the very large difference of direction between the two flows (Fig. 3.10). This shear layer is attached to the blade corner on the suction side. Vorticity may be created at a particularly high rate in this layer.
- (c) At the exit from the tip gap, the particle traces presented by Chima, and Suder and Celestina, exhibit clearly a negative axial velocity (Fig. 3.11). The strong

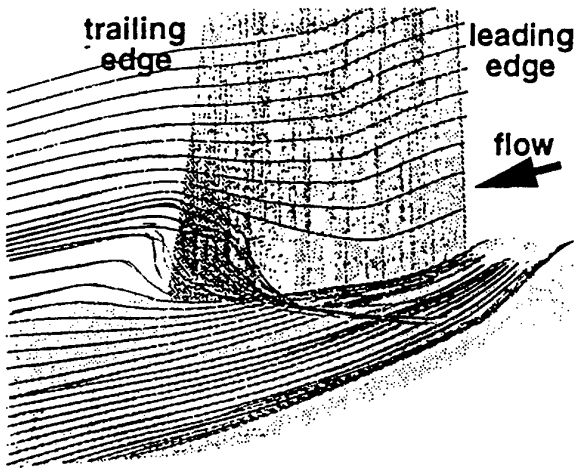


Fig 3.8 Computed particle traces at 99% choke flow (Hah & Loellbach, 1997)

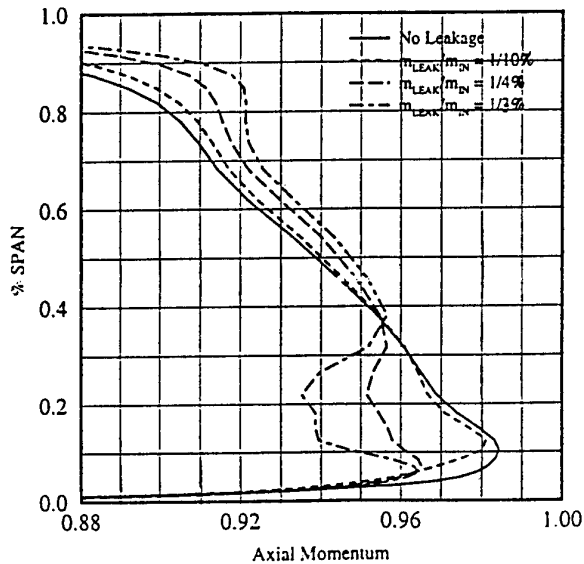


Fig 3.9 Effect of leakage flow on momentum mass distribution (Shabbir et al, 1997)

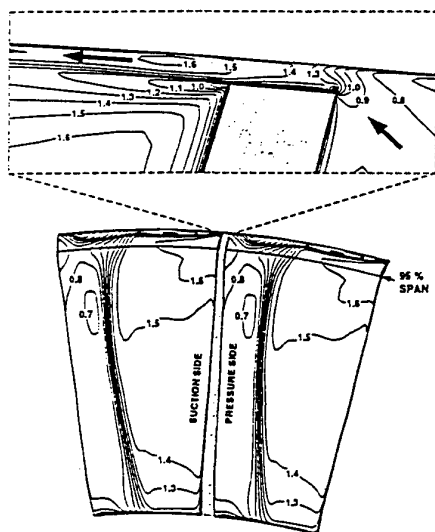


Fig 3.10 Relative Mach no. contours on a cross-section at 10% chord, near stall (Chima, 1996b)

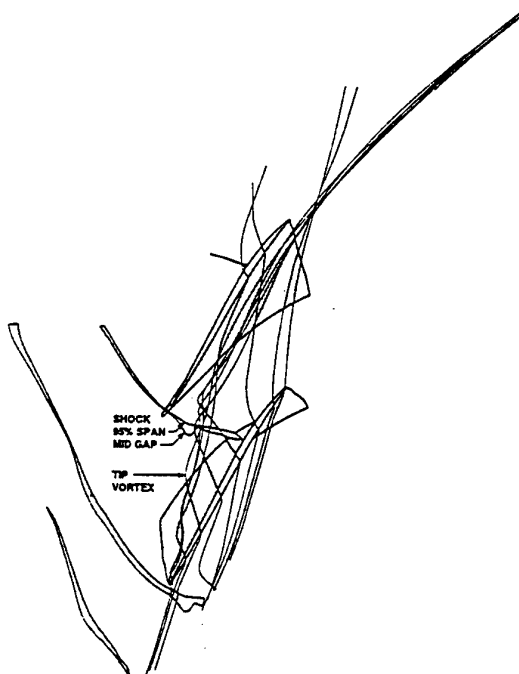


Fig 3.11 Shock system above 95% span at peak efficiency, with tip particle traces (Chima, 1996b)

- pressure gradient across the tip gap between the suction and pressure sides dominates the gradient along the blade chord. As a consequence, the leakage flow velocity vector points in a direction roughly normal to the blade suction surface.
- (d) The leakage flow and the main crossflow, both supersonic flows, merge along a line connected with the leading edge. The gradients of axial velocity component are very high across this line. Chima has shown that Chen's model (1991) predicts remarkably well the global flow path along this line. This is thought to be a three-dimensional separation line, along which the axial velocity is very small (Perrin et al, 1992). As soon as the leakage flow is ejected from the casing wall, it wraps itself up in a vortical movement. The origin of this vorticity is certainly linked to the shear layer attached to the suction side corner (see (b) above).
- (e) The interaction of this 3D separation line and the downstream leg of the passage shock occurs at mid-distance between the pressure and suction sides. A strong area of low velocity then appears downstream of the shock. This area extends over most of the blade passage as the mass flow decreases. The generation of a

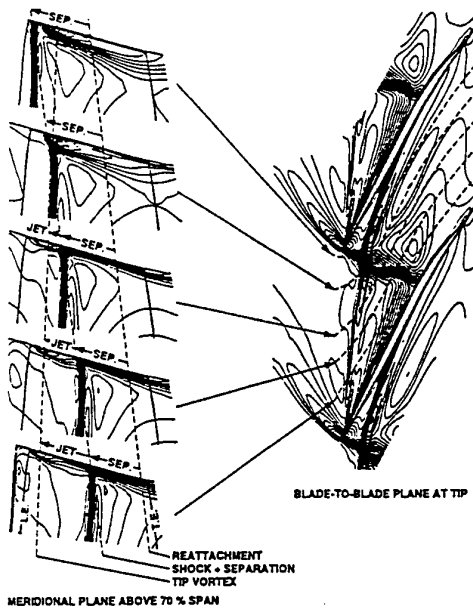


Fig 3.12 Mach number contours at peak efficiency (Chima, 1996b)

low longitudinal velocity area downstream of the passage shock is generated by an inviscid phenomenon. As mentioned by Schlechtriem and Lötzerich (1997), the interaction of a longitudinal clearance vortex with the passage shock creates a transverse vorticity in the direction parallel to the tip wall, that could lead to a flow separation. Chima (1996b) shows a separation in this area on the tip wall, which extends downstream of the passage shock over 30-40% of the blade chord (Fig. 3.12). This part of the leakage flow reaches the trailing edge, near the pressure side of blade.

- (f) The leakage flow, introduced downstream of the passage shock, deviates the separated boundary layer on the suction side that migrates radially towards the tip wall. This forms a second vertical movement particularly detected at part speed (Suder and Celestina, 1996). This second vortex does not merge with the first leakage vortex according to the simulation of Suder and Celestina (Fig. 3.13).
- (g) The mixing process of the leakage flow with the primary flow extends over 10% of the blade span, which is a distance equal to 20 times the tip clearance gap. This mixing process extends also probably far downstream.

The difficulties of analysing the simulated results arise from the lack of some plotted quantities in the experimental data, and in the simulated results as well. For example, the axial velocity component has not been plotted, although it was either measured or computed. As a consequence, the velocity triangles are difficult to analyse, and it is not possible to deduce always a firm conclusion from the comparisons between the experimental and CFD results.

Two main sets of data are considered:

- Blade-to-blade contour plots of  $M_{rel}$  are given at different percentages of the blade height; pitchwise plots of  $M_{rel}$  are given after the trailing edge, at stations 3 and 4, and at 20% chord inside the rotor at station 2.

- Radial plots of circumferentially averaged quantities are given at stations 3 and 4. Most of the authors have plotted the absolute stagnation pressure  $P_0/P_{ref}$ , the absolute stagnation temperature  $T_0/T_{ref}$ , the absolute flow angle  $\alpha = \tan^{-1}(V_y/V_z)$ , and the adiabatic efficiency  $\eta_{is}$ .

Two supplementary sets of plots are sometimes added:

- Contour plots are given in different surfaces (the meridional surface, a section normal to the axis of rotation, or on the blade surface) for the above quantities, plus the turbulent viscosity  $\mu_t/\mu$ , the entropy, and the static pressure.
- Particle traces show details of the tip leakage flow, the hub flow or the suction side flow behaviour.

### 3.2.3 Overall performance

The overall adiabatic efficiency is generally predicted to be at a lower level than in the experiments (Fig.3.2). The radial plots of the same quantities at station 4 (Fig 3.5) show an underprediction of 3% on efficiency between 10 and 80% of the blade span. Simultaneously, there is a strong deficit of efficiency for most of the simulations from 80% to the tip wall. It is concluded that the tip wall region is an important origin of the global loss overprediction in the simulations. Hah's simulation produces a higher value of the global efficiency, this seems to be associated with an underestimate of the losses from 30% to 85% of the span. It produces also an overestimate of the losses near the side walls for 98% of the choked mass flow.

Most of the simulations generate a higher pressure ratio than the measured one (Fig.3.1). A minority produces a lower value (Kang and Hirsch, CANARI using Michel's turbulence model). Two sets of results are close to the experiments at 98% of choked mass flow (TRACE-S, CANARI using the  $k-\epsilon$  turbulence model), and two others (CMOTT-CKE, TASCflow) are close to experiments at the near stall condition. The highest value of pressure ratio is obtained by Hah; that is consistent with the low losses at mid span as noted above.

The following remarks refer to the CFD results compared with the experimental ones in the form ( $Q_{simulation} - Q_{experiment}$ ). The pitchwise plots for 98% of the reduced mass flow show that, at station 2 at 20% chord inside the rotor, (Chima, Denton, 1996; Fig.3.14):

- 1) the computed  $M_{rel}$  is always lower downstream of the shock,
- 2) the shock is located too far upstream, provided a fine mesh is used.

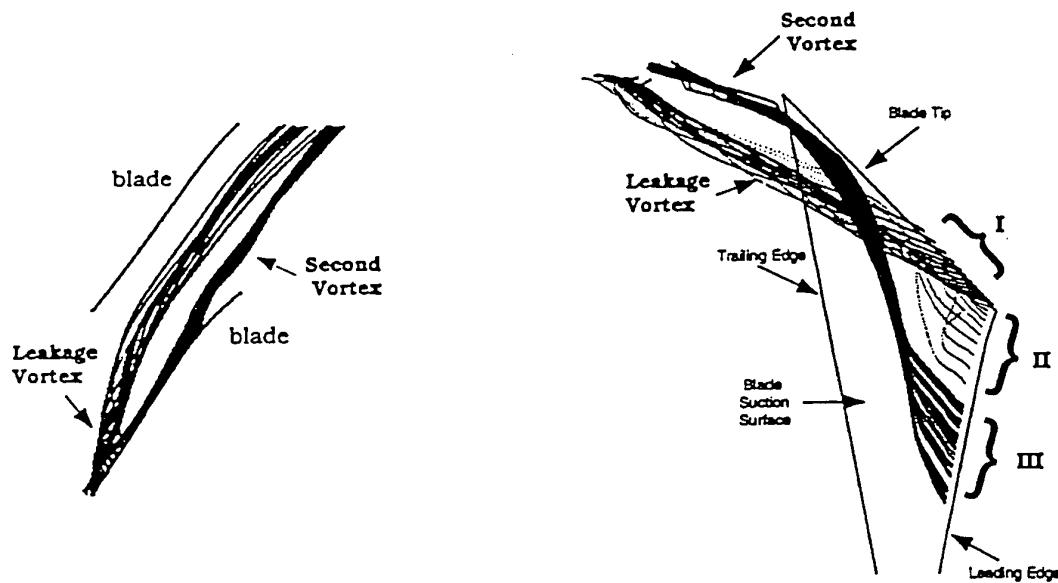
Part of the difference may be due to shock smearing in the calculation, though the smearing seems more important in the experimental results (Fig 3.14). A small particle lag effect could also have displaced downstream the experimental location of the shock wave.

At station 3, (Chima, Denton, 1996, McNulty; Fig.3.15):

- 3) the wake is always too deep,
- 4) the wake position at station 3 is for most of the simulations in agreement with the experiments.

At station 4,

- 5) the wake deficit is strongly reduced, although the experimental deficit is overpredicted (Chima), provided a sufficiently fine grid is used downstream.



Blade-to-blade view of particle traces indicating the formation of the leakage and second vortex.

Perspective view of particle traces indicating the formation of the leakage and second vortex.

Fig 3.13 Computed particle traces at 60% speed (Suder and Celestina, 1996)

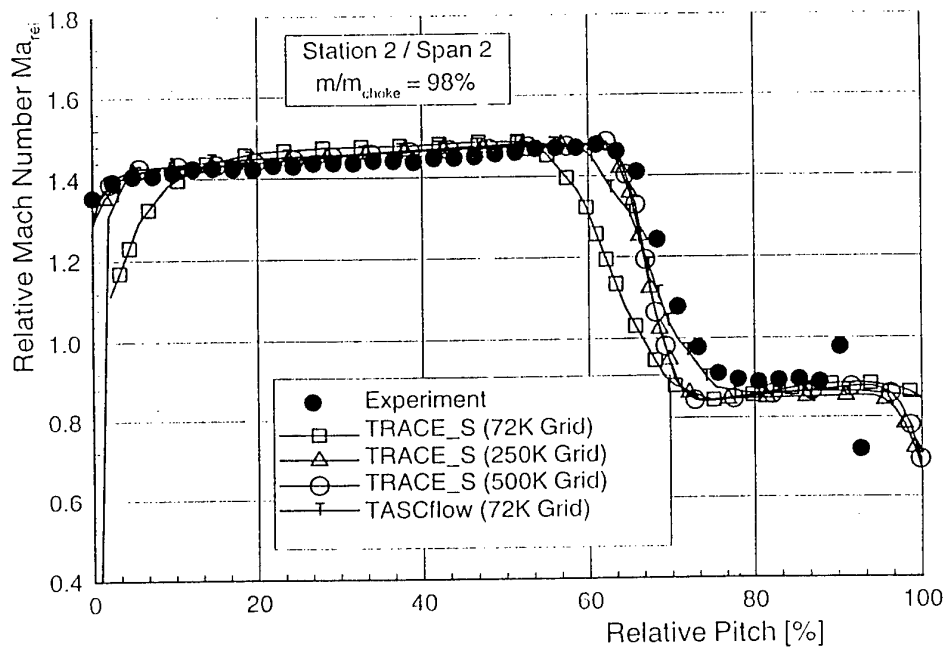


Fig 3.14 Mach number variation across the pitch at mid-span (Hildebrandt)

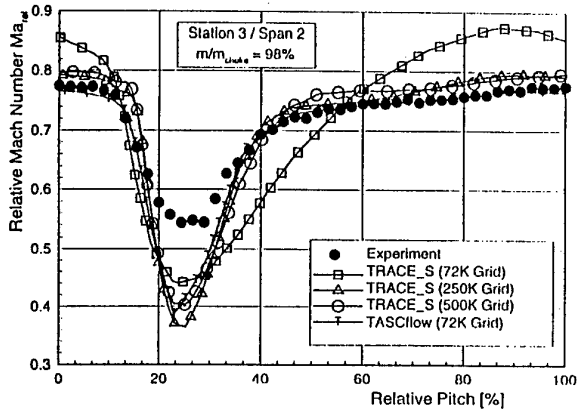


Fig 3.15 Mach number variation across the pitch at mid-span (Hildebrandt)

Some hypotheses are proposed for the origins of the differences between the results of the simulations and the experiment.<sup>1</sup>

- a) For a fixed passage shock strength, the low post-shock Mach number  $M_{rel}$  (observation no.1) could be induced by too thin a post-shock boundary layer on the suction side (Denton, 1996). This is because the subsonic Mach number downstream of the shock is reduced if the flow blockage diminishes. This implies a lower predicted loss in the wake. However, this hypothesis is in contradiction with (3) the deeper simulated wakes at station 3 (Denton, 1996).
- b) It was also observed that (2) the shock is slightly displaced upstream, implying a stronger shock than expected. This stronger shock is compatible with the lower Mach number downstream of the shock. This is obvious from the blade-to-blade plots of Chima or Hildebrandt for instance. As the shock is displaced on the suction side towards the leading edge, the downstream static pressure is higher than expected, implying that the mass flow used in the simulation is too low. Chima's simulations have shown, by means of a downstream adjustment of the static pressure, that an increase of 0.24% for the mass flow (from 98% to 98.24%) is sufficient to fit the experimental blade-to-blade Mach number distribution (Fig.3.16). Note that while this modification has a strong influence on the shock location and the downstream Mach number distribution, it has almost no effect on the upstream Mach number value. This value (0.24%) is also of the same order as the difference between the averaged choked mass flow deduced from the simulations (20.86 kg/s) and the experimental value (20.93 kg/s). It may be thought necessary to compensate for the small error in the predicted choked mass flow by making a comparison at a slightly higher mass flow than the required 98% value. However, this small difference on the choked mass flow will not explain alone the strong discrepancies between the experimental and simulated

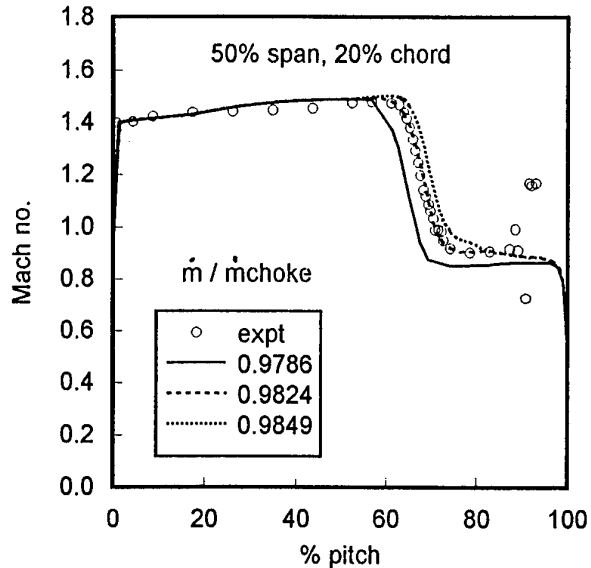


Fig 3.16 Comparison of three solutions nominally at 98% choked flow (Chima)

results observed at 20% of the blade height from the hub.

- c) The observation (3) of deeper simulated wakes in station 3 is a common feature of all the simulations. It may be thought that some flow phenomena are not simulated. The rotor wake deficit ( $M_{rel,max} - M_{rel,min}$ ) /  $M_{rel,max}$  has been plotted as a function of the axial distance by McNulty for 70% of the blade span (Fig. 3.17). It shows that the experimental deficit is 1/3 lower than in the simulation near the trailing edge. But the wake may be unsteady due to periodic vortex shedding. If so, a laser velocimeter will detect two velocity minima at slightly different positions, and the "average" wake will be less deep than either of the two time-resolved minima. So it is not clear whether the difference between the simulations and the measurements is due to unsteadiness in the real flow, to forcing the simulations to a "steady" solution, or to the turbulence model.
- d) It must be remembered that the experimental flow gradients are strongly dependent on the mass flow. The gradients computed at station 4 are also a consequence of the amount of loss generated in the rotor and downstream of the rotor. The slope of the wake decay is higher in the simulation (Chima) after a distance of 150% chord downstream. The higher wake dissipation observed in the simulation between stations 3 and 4 (5) may be connected with the mesh topology used in the downstream zone for most of the simulations. This suggests the need to improve the mesh density and the grid alignment with the wake direction downstream of the rotor.

### 3.2.4 Radial plots for 98% of choked mass flow

#### 3.2.4.1 Stagnation temperature plots

- At mid-span, Kang and Hirsch's results are slightly too low, while CMOTT, SWIFT, CANARI using both Michel's turbulence model and the  $k-\epsilon$  turbulence model, and TRACE-S agree with the experimental values, and all the other simulations produce too high a level of temperature.

<sup>1</sup> The numbers in parentheses designate the observations quoted at the beginning of the paragraph

## NEAR PEAK EFFICIENCY (98% Choke) - 70% SPAN

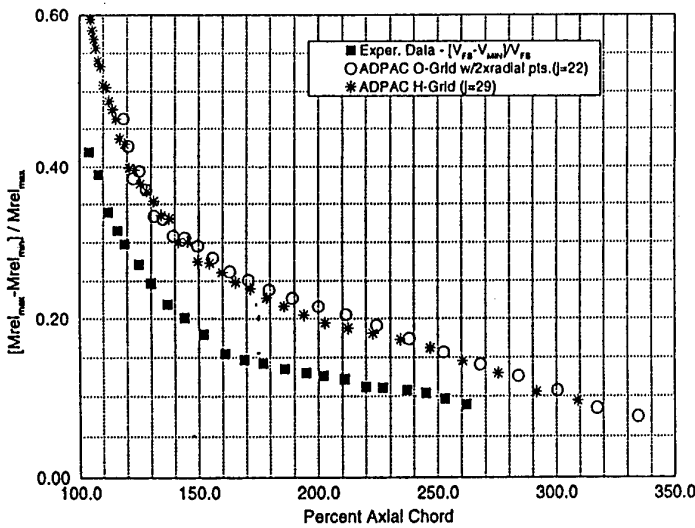


Fig 3.17 Rotor wake decay (McNulty)

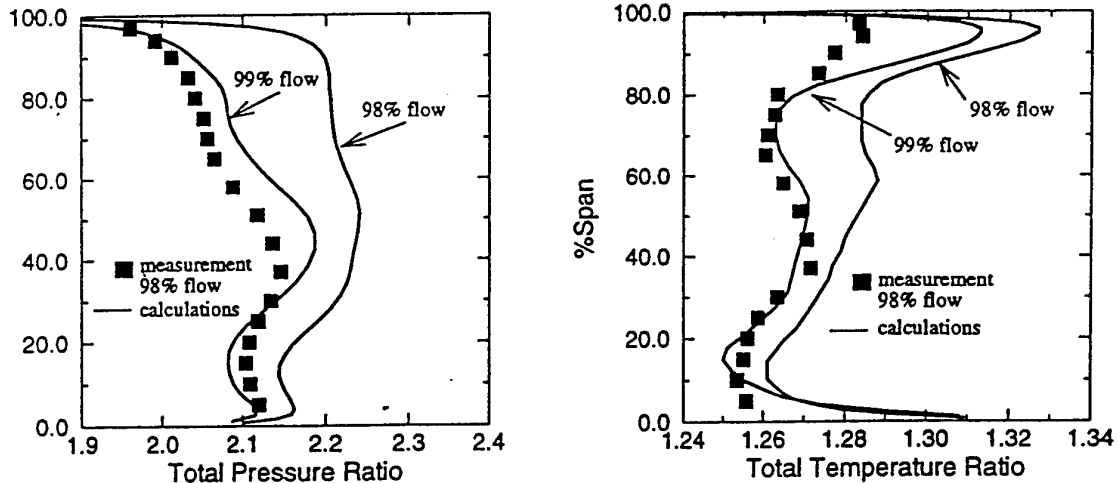


Fig 3.18 Variation of performance with mass flow (Hah and Loellbach, 1997)

- Near the casing, all simulations produce a strong increase of  $T_o$  after 90% of the span, except TASCflow<sup>†</sup> which shows a strong decrease.
- Near the hub wall, in between 0-8% of the span, all the simulations produce an increase of temperature, except for TASCflow that shows a strong decrease, and TRANSCODE-Baldwin-Lomax which produces a constant value.

### 3.2.4.2 Stagnation pressure plots

It has already been mentioned that only a few sets of results produced an overall pressure ratio lower than

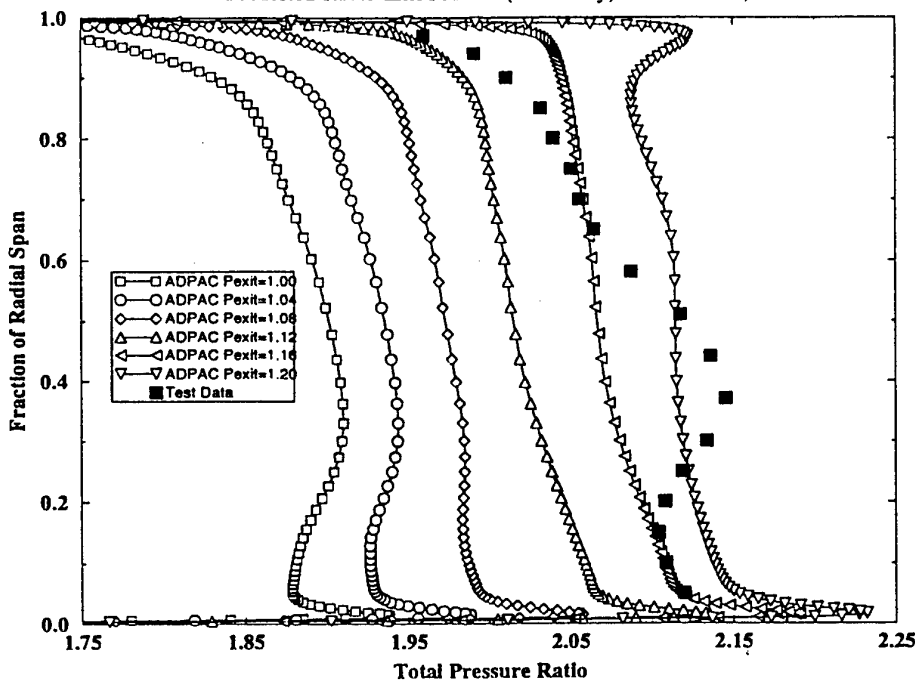
the experimental values. At mid-span, Kang and Hirsch and CANARI using Michel's turbulence model produce a low  $P_o$ , two sets (TRACE-S, CANARI using the  $k-\epsilon$  turbulence model) are very close to the experiments, while all the others produce a higher  $P_o$ .

- Near the casing, the slope of the decrease towards the wall is greater than the experiments for CANARI using Michel's turbulence model, and the Kang and Hirsch and SWIFT predictions.
- Near the hub wall, only Hah's simulations give the decrease of  $P_o$  observed under 30% of the blade height for the 98% of the choked mass flow. However some of them show a sort of plateau in this region (Kang and Hirsch, CANARI using the  $k-\epsilon$  turbulence model). Most give a supplementary increase in between 0-8% of the blade height. Hah and Loellbach (1997) report also a much better agreement with the experimental results for  $P_o$  and  $T_o$  if the mass flow is increased from 98% to

<sup>†</sup> As the report was going to press, Dr Hutchinson informed the WG that a revised treatment of the energy equation in the near-wall region had recently been incorporated in TASCflow, now called CFX-TASCflow, which had greatly improved the predictions of overall performance for Rotor 37.

### NASA Rotor 37 Cavity Analysis

Predicted Rotor Exit Profiles (No Cavity, Coarse Mesh)



Predicted Rotor Exit Profiles (No Cavity, Fine Mesh)

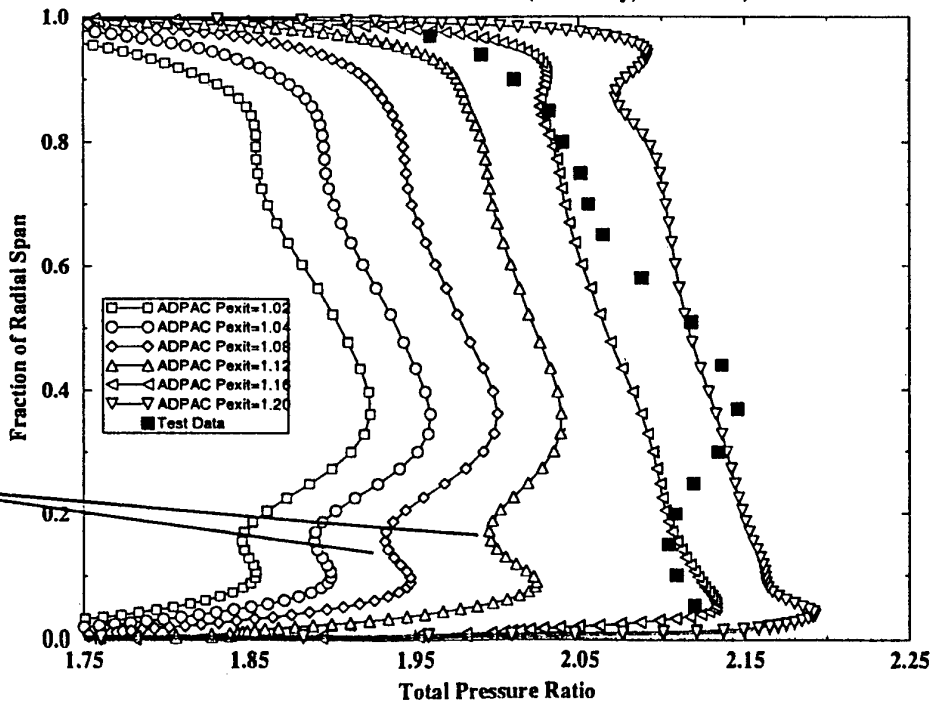


Fig 3.19 Influence of overall pressure ratio on rotor exit flow: coarse mesh and fine mesh, no cavities (Hall)

### NASA Rotor 37 Cavity Analysis

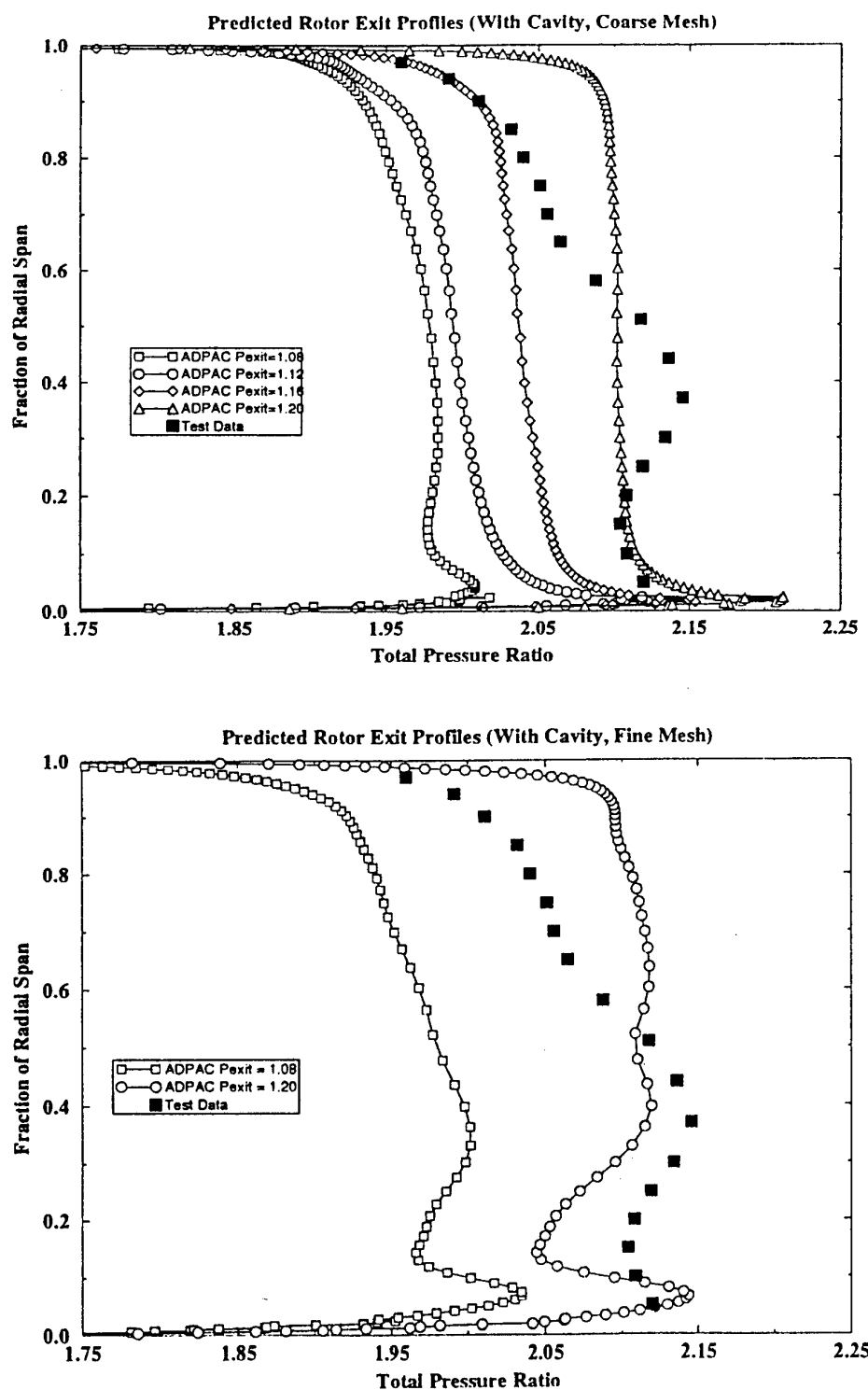


Fig 3.20 Influence of overall pressure ratio on rotor exit flow: coarse mesh and fine mesh, with cavities (Hall)

99% (Fig.3.18). Similar results are reported by Delaney. An increase of the mass flow by only 0.3% generates the decrease of  $P_o$  at 30% of the blade height (Fig.3.19). A sufficient mesh density in the radial direction seems very important in order to capture this  $P_o$  deficit. Note however that the  $P_o$  hub deficit exists in the experiment for all the mass flows (Strazisar).

- The existence of a cavity between the rotating rotor hub and the upstream fixed hub strongly influences the  $P_o$  deficit (Fig.3.20), (Delaney, Shabir et al, 1997).

#### 3.2.4.3 Adiabatic efficiency plots

- Most of the predictions give a good distribution at mid-span, except SWIFT which is too high, and Kang and Hirsch and TASCflow which are slightly too low.
- Near the casing, most of the simulations produce a lower efficiency than expected, except CMOTT and TASCflow. Near the hub wall, some of the simulations give an increase of the efficiency towards the wall (CMOTT, Shabir, CANARI using Michel's turbulence model, TRACE-S).

#### 3.2.5 Hypotheses for the origins of the differences

##### between results of simulations and experiment

Unfortunately, most of the radial plots are provided at station 4 only. Station 4 is also located near or even at the downstream boundary of the mesh. The numerical dissipation is believed to be too high between the rotor trailing edge and station 4, owing to the size of the cells. As a consequence, it is very difficult to derive firm conclusions.

- a) The radial stagnation temperature distribution gives a good estimate of the level of the axial velocity component  $V_z$ . To explain this point, assume that the relative flow angle  $\beta$  is correctly computed. This is a reasonable hypothesis, considering for instance the predicted location of the wake in station 3. Some authors provide  $\beta$  radial distributions (ADPAC-McNulty) with a good agreement between the results of simulation and experiment. An overprediction of the work is then generated by a low value of  $V_z$ , and conversely. A low/high mass flow is also consistent with a high/low pressure.
- b) Near the tip wall, the overestimate of the work may be linked with either a low axial velocity, associated with high losses, and/or a decrease of the relative flow angle  $\beta$ . Note, however, that the flow Mach number is very sensitive to small variations of the blade-to-blade relative flow direction as the exit Mach number is nearly sonic. According to the efficiency distribution, high losses occur near the tip wall for all the simulations, except for CMOTT and TASCflow. For CMOTT, there should be a low absolute value of the relative flow angle  $\beta$  near the wall. For TASCflow, there is actually an underprediction of the work at the wall, which is then compatible with low losses and a high velocity. By comparison with the measurements, the flow blockage generated by the tip wall layer should then create an increased axial velocity in the mid-span region, with a corresponding reduction of the work. This is not always observed in practice, (except for Kang and Hirsch's results) perhaps because of the influence of the error in the choked mass flow, as shown by Chima.
- c) For most simulations, near the hub wall, a high value of the work is observed with a high efficiency, and a high stagnation pressure. This is compatible with a small thickness of the wall shear layer, and then a high value

of the axial velocity and a high flow deflection in the relative frame of reference (passage vortex effect). This is particularly true for CMOTT, Shabir, CANARI using Michel's turbulence model, and TRACE-S. The flow in the hub region is probably dominated in the experiment by a strong corner stall near the suction side (Hah and Loellbach, 1997, Delaney, Kang and Hirsch). This corner stall is extremely sensitive to small modifications of the boundary conditions, such as the global mass flow variations that act upon the Mach number ahead of the leading edge at the hub, the upstream cavity, or the radial mesh distribution.

It is important to notice that the flow at mid span is also strongly dependent upon the flow near the hub and tip walls. This is typical for this sort of supersonic compressor. The large loss that should occur in the hub region acts as a strong aerodynamic blockage. It pushes the mass flow towards mid-span, thereby reducing the blade work at mid span (Kang and Hirsch). An exception is observed for Hah and Loellbach's results: although they obtain a large corner stall at the hub, they overpredict the pressure ratio at mid span. Owing to their parallel overestimation of the efficiency at mid span, it may be suspected that the shock boundary layer loss generation is minimised in their simulation.

#### 3.2.6 Plots of turbulent quantities

Detailed plots of turbulent viscosity have been provided by Calvert with TRANSCode, McNulty and Heidegger with ADPAC, Hildebrandt with TRACE-S, Couaillier with CANARI, and Chima with SWIFT. Although very different turbulent models have been used, all the results present similar trends.

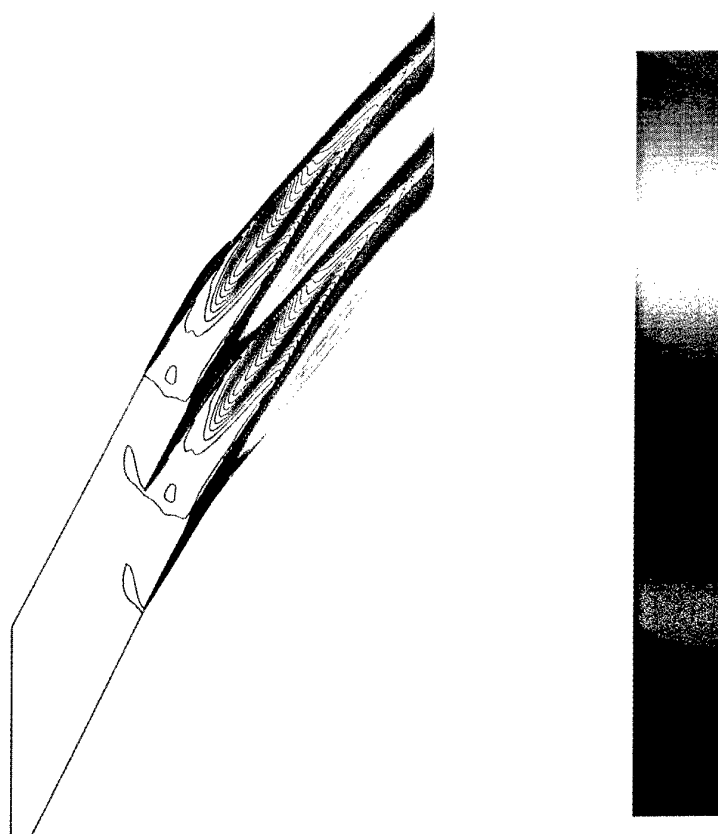
At 35% of the blade height near the trailing edge at station 3, the flow behaves as a quasi-3D flow outside the wake or viscous layers. The Mach number is also almost constant over a large part of the blade span, outside the wake region. The turbulent viscosity has a significant value only in the wake area, where a strong radial movement is also observed. (Fig. 3.21).

By contrast, at 90% blade height (Fig.3.22), the flow feels the influence of the tip wall. The increase of the turbulent viscosity on the pressure side near the trailing edge may be the result of the accumulation of the tip leakage flow that crosses the blade passage from the suction side (Chima, 1996b). Simultaneously, the contour maps of  $M_{rel}$  in the blade-to-blade section show a strong reduction of the Mach number in the middle of the blade passage.

This interaction of the primary flow with the leakage flow may be then dominated by a separation of the wall layer, as shown by Chima, that could create the very high values of turbulent viscosity, particularly for the low mass flow.

#### 3.2.7 Assessment

- 1) Most of the simulations generated a low axial velocity at mid-span. This could be induced by three phenomena. Firstly, most of the simulations predict a slightly low value of the choked mass flow. It can then be an error to compare simulations at a fixed percentage of the simulated choked mass flow. Secondly, most of the simulations do not capture the hub corner stall; this is probably the most important effect. As a consequence, a higher proportion of the mass flow passes through the hub region, thereby decreasing the axial velocity at mid-span. Thirdly, the shock/boundary layer interaction may not be predicted



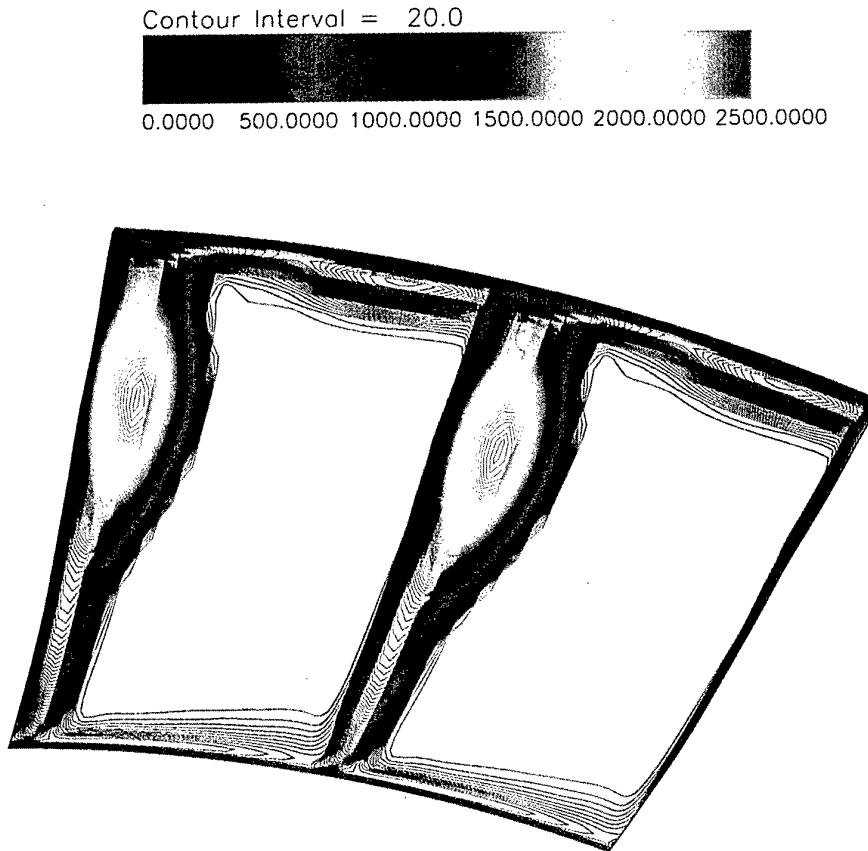


Fig 3.23 Viscosity ratio at station 3 (Calvert)

correctly. A more detailed study of the results is suggested, to establish which explanation is correct in this case.

- 2) The tip region generates too much loss in most of the simulations.
- 3) In the hub region, the predicted pressure ratio and temperature ratio are both too high, because the corner stall is either not predicted or is minimized. The corner stall has been linked by Shabbir et al (1997) to the existence in the experiment of an axial gap between the upstream fixed hub and the rotor. The predicted corner stall is also very sensitive to the radial mesh density, the global mass flow, and the turbulence model. A high flow deflection of the hub boundary layer is a possible explanation that would be consistent with an underestimation of the corner stall.
- 4) All the turbulence models are unable to predict the strong flow deceleration in the outer wall boundary layer. The high loss seems to appear as a consequence of the interaction between the passage shock and the leakage flow "vortex". The flow reaction is probably too abrupt across the shock, which is a common feature of all equilibrium turbulence models, such as the mixing length or linear  $k-\epsilon$  models. It is important to notice the low value of the turbulent viscosity near the tip wall, compared with the value obtained near 70-80% of the span at the trailing edge (Fig.3.23).
- 5) The mixing length model generates more loss in the tip wall region than the  $k-\epsilon$  model. The interaction between the leakage flow and the primary flow is certainly far more complex than a simple boundary layer situation

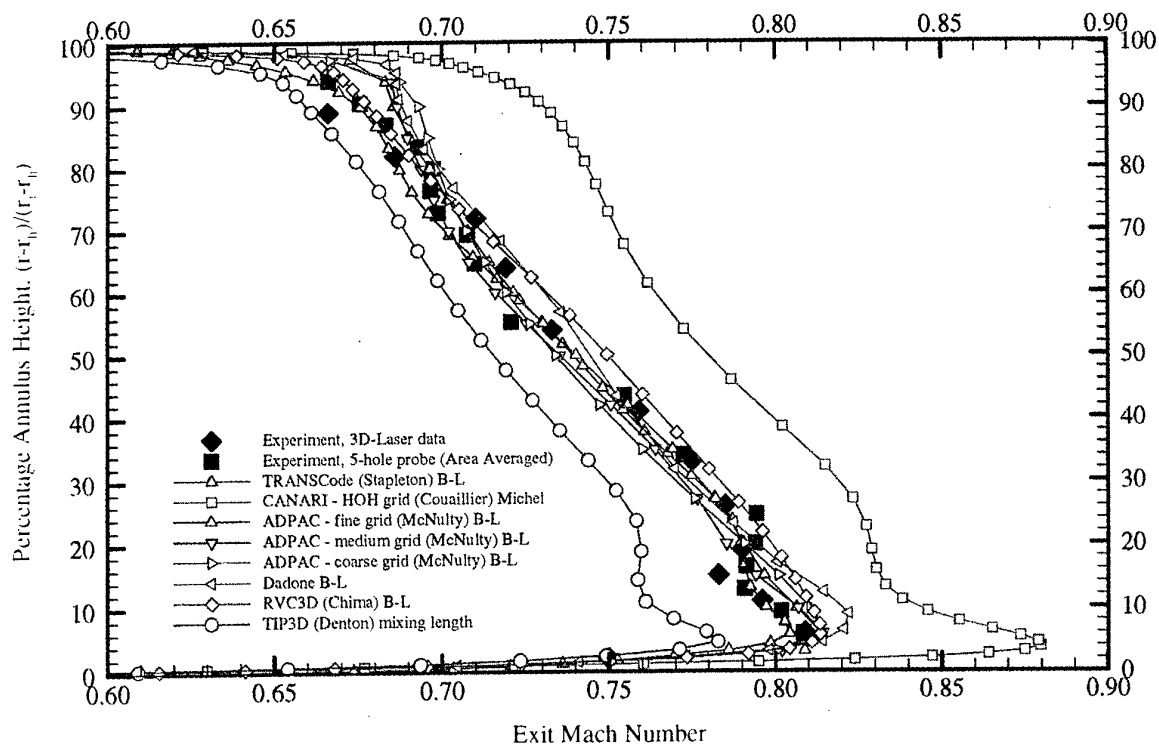
for which the mixing length model was developed. Various flow phenomena have been observed: the shear layer linked with the suction side corner at the blade tip, the 3D separation line followed by the so-called leakage "vortex", and the radial transport of the suction side boundary layer followed by its abrupt transfer toward the pressure side under the influence of the leakage flow. All these phenomena have to be treated along the tip wall, for which the turbulence model only "sees" a single length and a single velocity scale, while the tip wall flow is dominated by several different lengths and velocity scales.

Solutions using Baldwin-Lomax turbulence model are mostly similar, despite using a wide range of different codes, grid topologies and number of points, as long as at least 300K points are used.

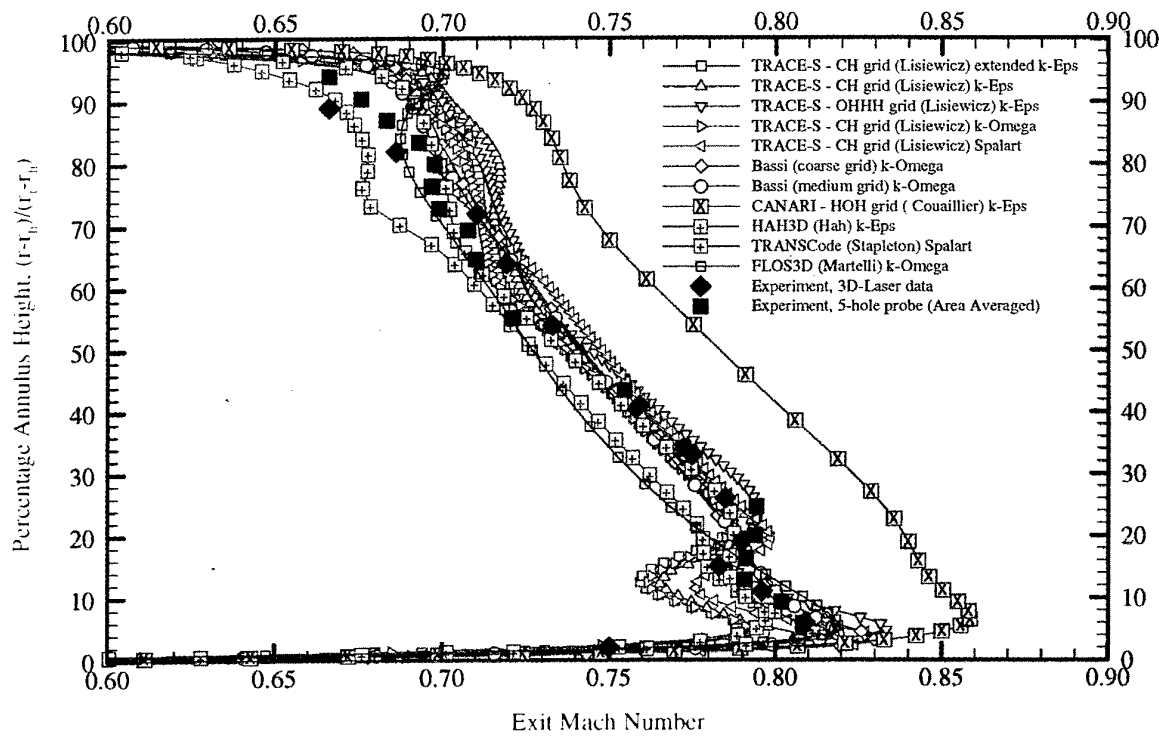
### 3.3 THE RESULTS FOR THE DLR CASCADE

#### 3.3.1 Computations requested

The contributors were requested to compute the flow field through the annular turbine cascade corresponding to the operating point defined in Section 2.2.5. Measurements were taken by means of both L2F anemometry and five-hole pressure probes in a plane (MP3) located at 40% of an axial chord downstream of the mid-span trailing edge. For the purpose of comparison the pressure probes data have been used for pressures, but the flow angles and Mach numbers measured by the anemometer have been preferred to those measured by the pressure probes. The main requested plots

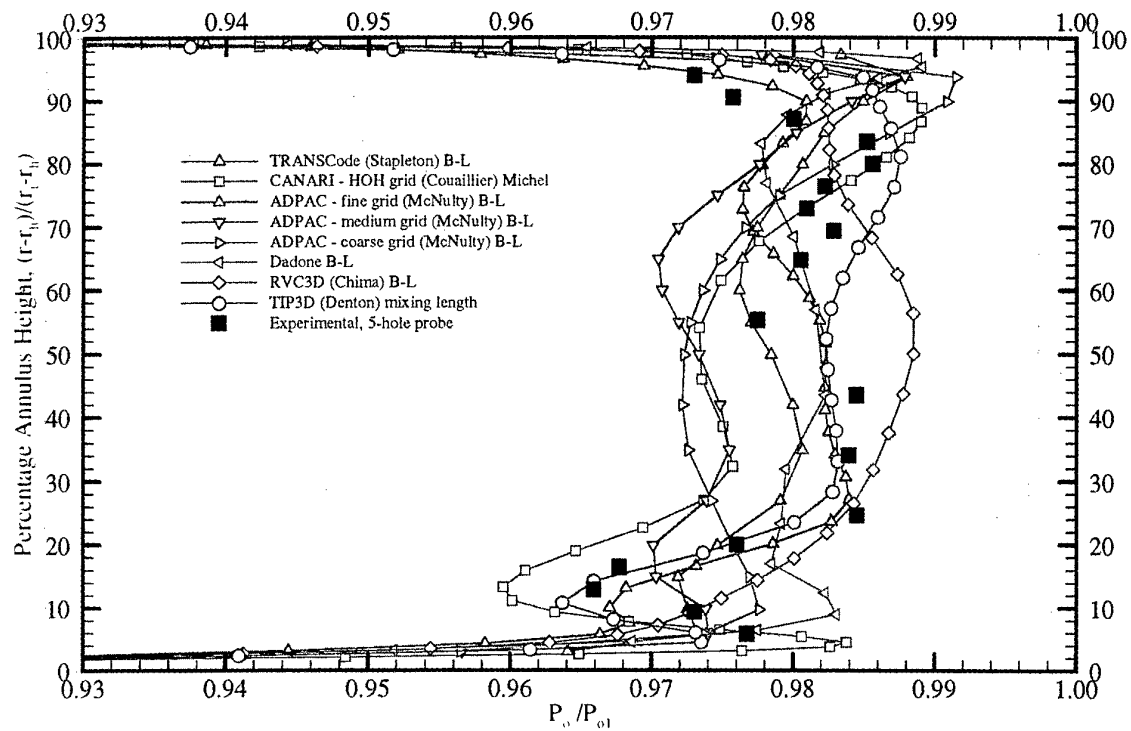


(a) algebraic / mixing length turbulence models

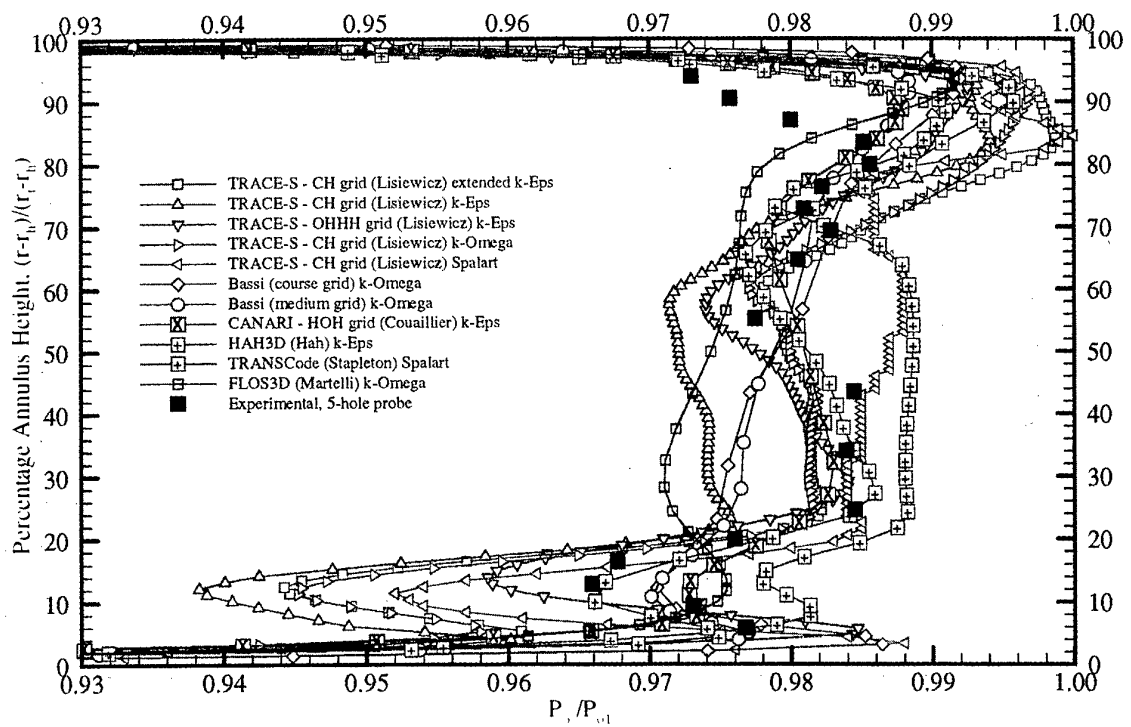


(b) turbulent transport models

Fig 3.24 DLR cascade: Mach number

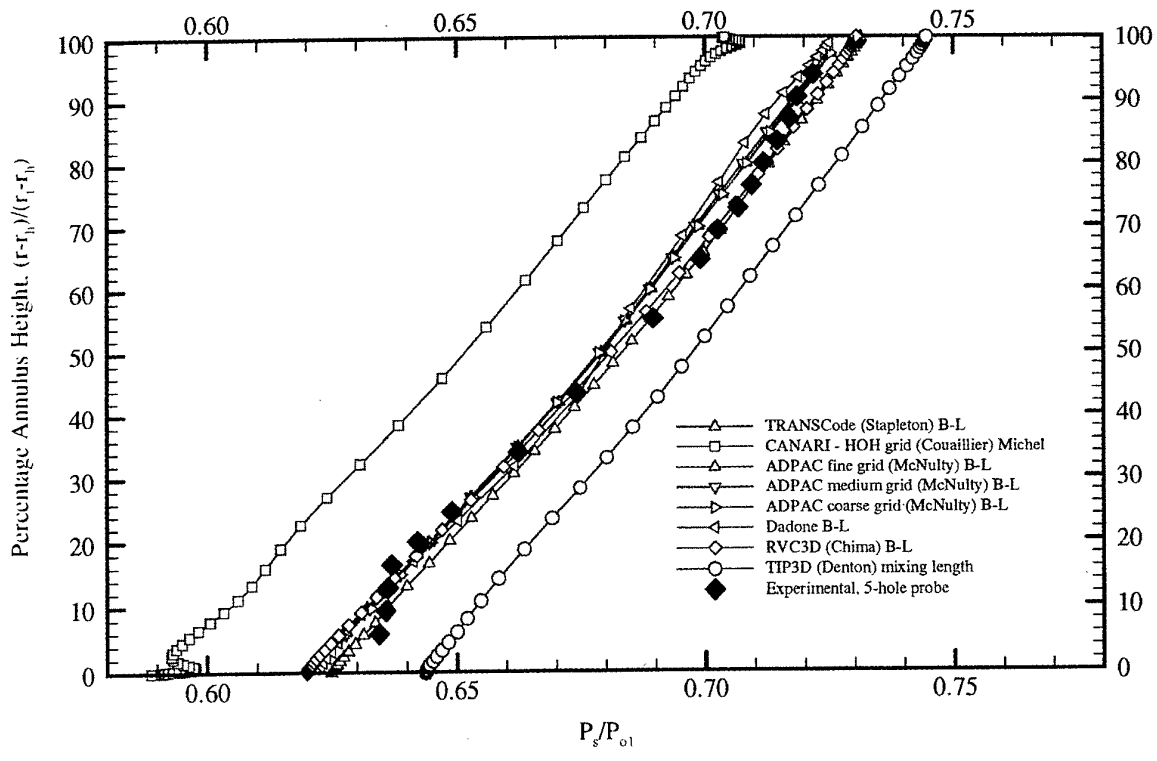


(a) algebraic / mixing length turbulence models

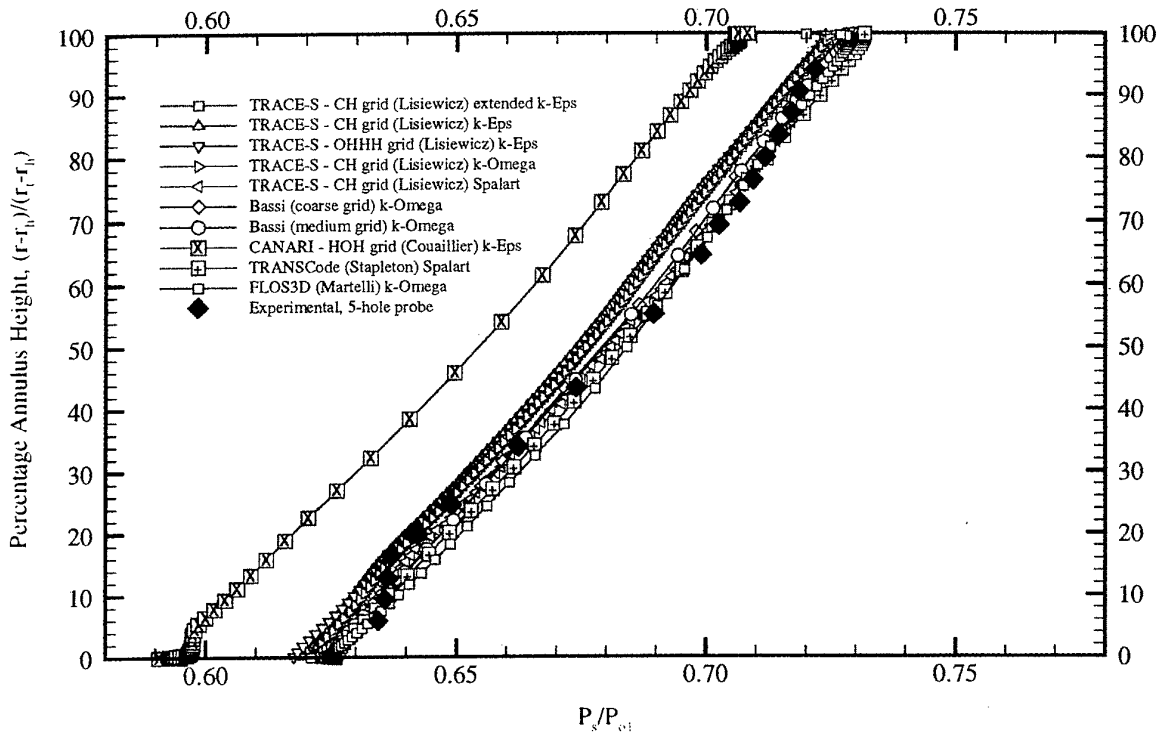


(b) turbulent transport models

Fig 3.25 DLR cascade total pressure ratio

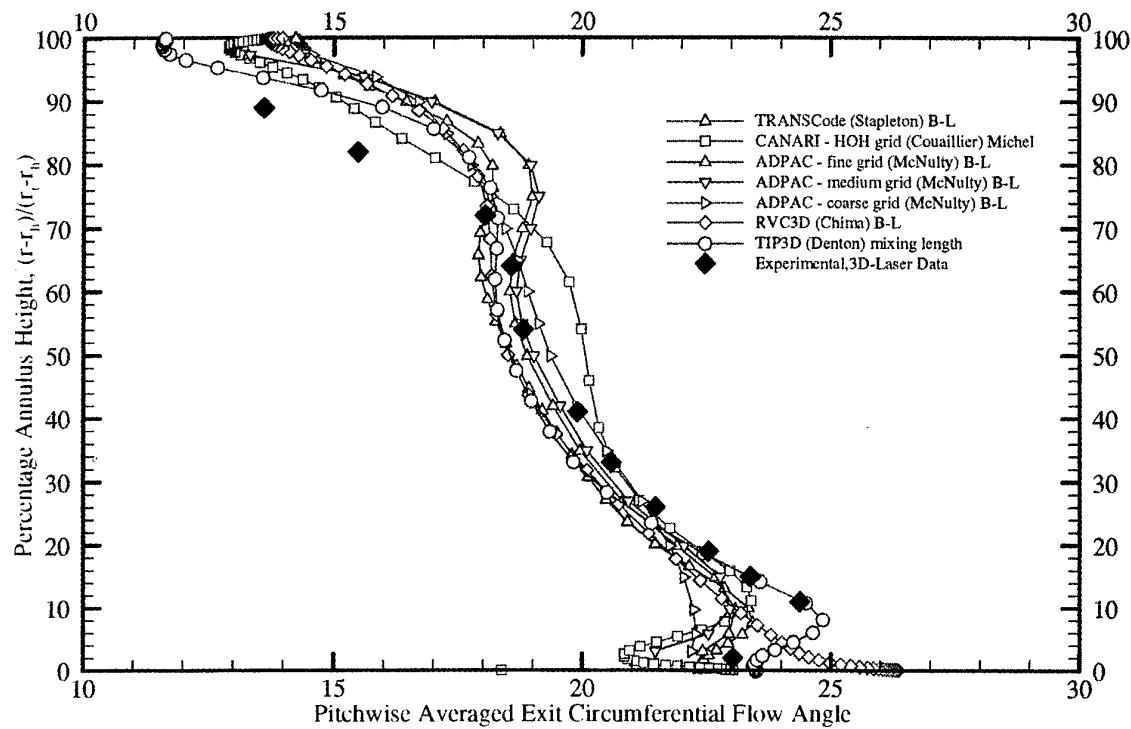


(a) algebraic / mixing length turbulence models

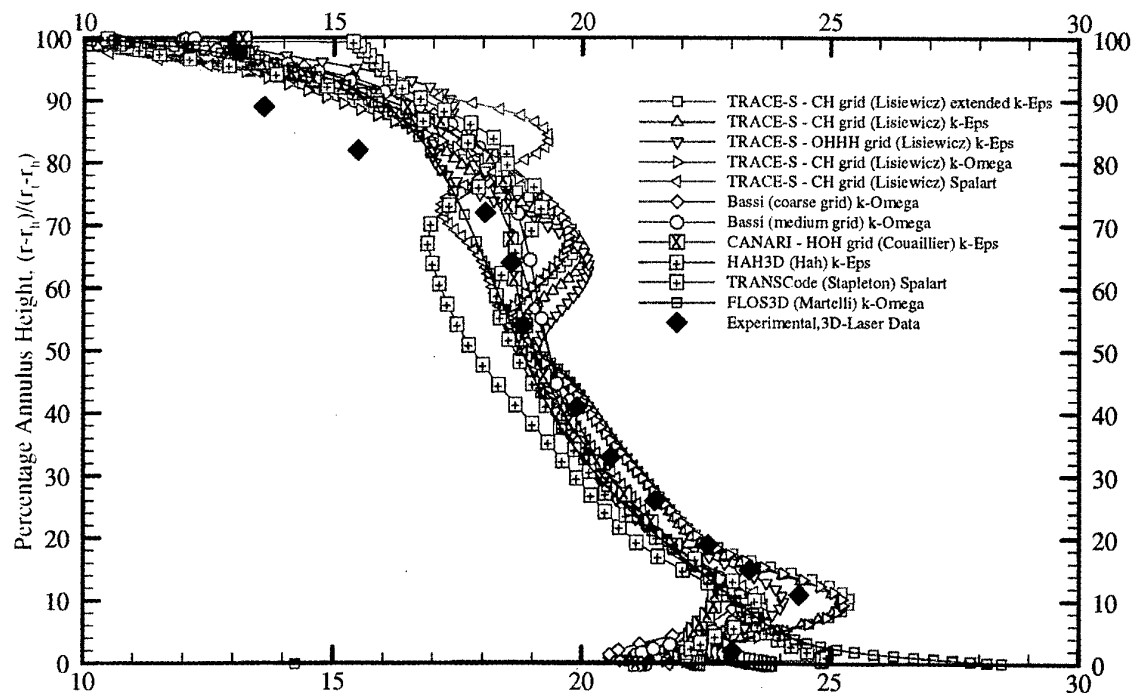


(b) turbulent transport models

Fig 3.26 DLR cascade: static pressure / reference total pressure



(a) algebraic / mixing length turbulence models



(b) turbulent transport models

Fig 3.27 DLR cascade: circumferential flow angle (measured from the tangential direction)

were the spanwise distributions of pitchwise-averaged static pressure, total pressure and flow angles, and the contours of the same quantities in the measuring plane. In addition, the isolines of Mach number and total pressure were requested in the blade-to-blade surfaces at 10%, 50% and 90% of the span. In order to assess the behaviour of the turbulence models, contributors had to provide isolines of the ratio of turbulent to laminar viscosity  $\mu_t/\mu$  in the above mentioned surfaces as well as a pitchwise Mach number traverse at midspan across the wake.

When averaging the computational results, pressures and velocity components were mass-averaged, and the angles derived from the averaged velocities. A specific check showed that when the measured angles were averaged in the same way (instead of area-averaged) the changes from the reported results were less than 0.1°.

Figs 3.24-27 compare the results of all the computations with the pitchwise-mean measurements.

### 3.3.2 Flow description

The following flow features can be deduced from the experimental data in the measuring plane (Figs 2.10-2.32):

- 1) The radial distribution of static pressure is in agreement with the tangential flow angles.
- 2) Moderate negative values of radial flow angle (i.e. flow directed toward the hub) can be found in the wake region, as expected in an annular stator cascade.
- 3) A core of total pressure loss, associated with the secondary flow vortices, is clearly visible near the hub. In the tip region the loss core is shifted toward the midspan and there is evidently a marked distortion of the wake.

### 3.3.3 Overall performance

Few contributors specified the computed values of mass flow rate and overall total pressure loss: the flow agrees with orifice-measured mass flow rate within 1%, but the loss varies very widely. The calculated spanwise distribution of total pressure loss is reported by all authors. From Fig 3.25, it can be argued that the overall loss prediction disagrees in some cases up to 40% with the measured value. It can also be seen that the local discrepancies at each spanwise position are on average much higher.

### 3.3.4 Radial plots

#### 3.3.4.1 Static pressure (Fig 3.26)

The slope predicted by the various calculations is in good agreement with the experiments. This means that the condition on the radial distribution of pressure imposed at the outlet boundary (usually a simplified form of radial equilibrium) does not impair the pressure distribution at the measuring station. Differences among the values at fixed radial positions are mainly due to the different values of pressure assumed by the contributors at the downstream reference radius. More surprising is the influence of turbulence model and of grid topology on the pressure distribution computed with the same flow solver (TRACE-S).

#### 3.3.4.2 Total pressure (Fig 3.25)

Most of the codes display total pressure radial distributions grouped within a reasonable band around the experimental values, but not one of them proved able to capture fairly well all of the significant features of the measurements. Generally the loss core at the hub is better captured than the one at the tip. Looking at the simulations characterized by a small number of points in the radial direction, it seems that predictions improve with a radial refinement of the grid.

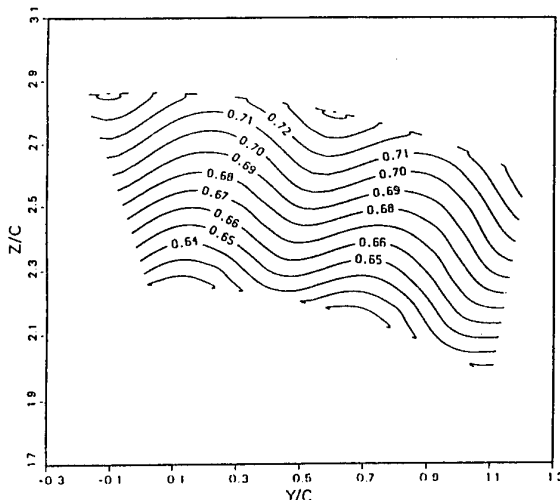


Fig 3.28 Static pressure at MP3 / reference total pressure (Bassi/Savini)

However, one of the best results (TRANSCode) does not employ a great number of points. Once again the influence of turbulence model and grid topology on the total pressure distribution predicted by TRACE-S is remarkable.

#### 3.3.4.3 Mach number (Fig 3.24)

These graphs are only a combination of the pressure and total pressure ones and their general trend is satisfactory, differences worth mentioning occurring only in the near wall regions.

#### 3.3.4.4 Circumferential flow angle (Fig 3.27)

The scatter in the computed solutions is 1-2° and the differences between measured and computed tangential flow angles near the endwalls are significant. All codes fail to reproduce the correct amount of overturning at the tip. Computations using the greatest number of points in the spanwise direction exhibit the best agreement and this observation suggests that it is necessary to use a large number of points to obtain a correct resolution of the vortical structures near the endwalls. Maybe an even greater number of points is needed to reach a truly grid-independent solution.

### 3.3.5 Contour plots in the measuring plane

#### 3.3.5.1 Static pressure

Every submitted plot, for example Fig 3.28, shows the same tangential wave-like oscillations of pressure displayed by the post-processing of the measured data. These are an outcome of the real 3D blade configuration and they are gradually damped moving downstream. Notice that the assumption of pitchwise uniform static pressure at the outlet boundary made by some contributors did not spoil the solution at the measuring plane.

#### 3.3.5.2 Total pressure (Fig 3.29)

The relevant feature of the comparison among the various authors and the experiments is the more or less pronounced distortion of the wake. Concerning this item, DLR's TRACE-S computations (performed with the greatest number of spanwise points) gave the best results (b). Nevertheless, approaching the tip, the computed results show a radial band

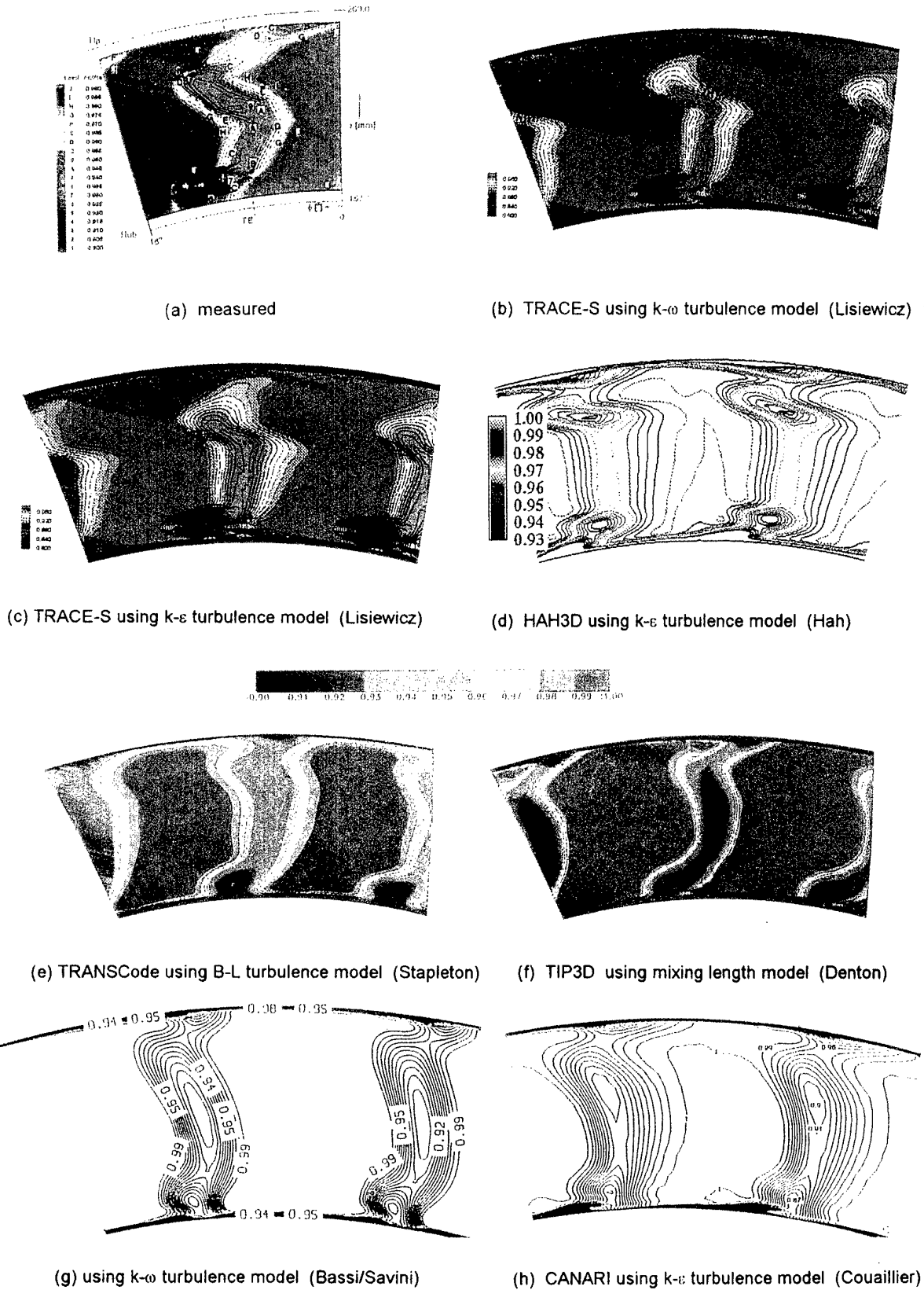


Fig 3.29 Contours of total pressure/reference total pressure at MP3

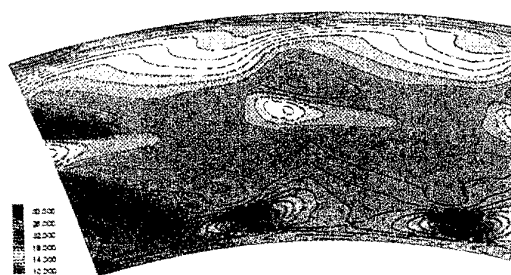
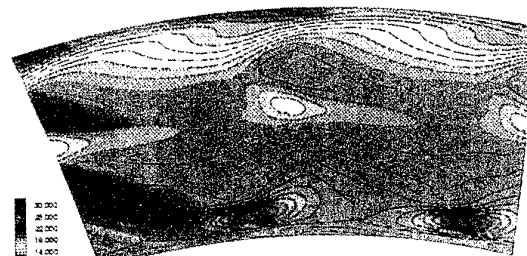
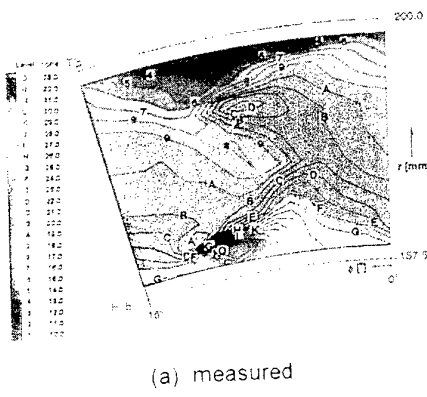
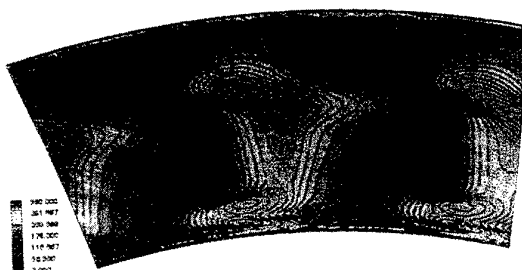
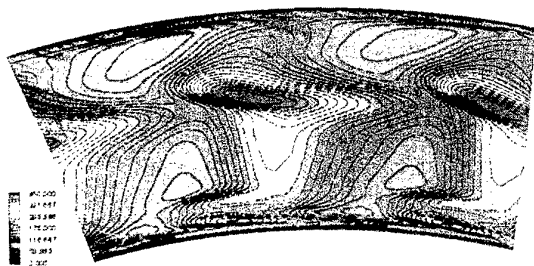
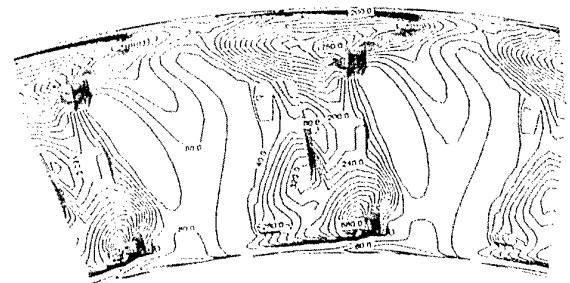
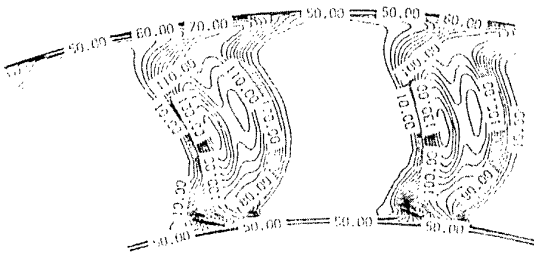


Fig 3.30 Contours of circumferential flow angle at MP3



(a) TRACE-S using  $k-\omega$  turbulence model (Lisiewicz)



(c) using  $k-\omega$  turbulence model (Bassi/Savini)

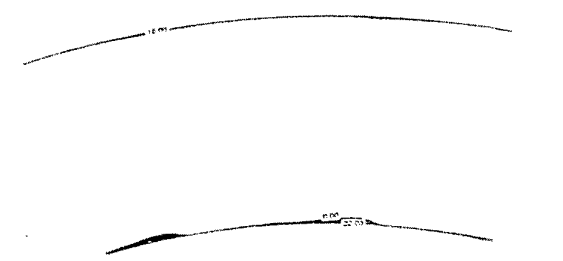


Fig 3.31 Contours of eddy viscosity ratio at MP3

with almost no losses. Good agreement with the experiments were also obtained by HAH3D and DRA codes (d, e) with a somewhat medium radial number of points. No grid refinement studies were reported for TRACE-S, so it is not clear whether 117 points in the radial direction are either necessary or sufficient. Grid refinement studies by Stapleton did not show significant changes for the DLR turbine for >330K points (49 radial). McNulty tried grids with 25 and 49 radial points, and his results clearly show that 25 radial points are insufficient, but not how many more are needed. Examining the influence of turbulence models, the TRACE-S results using the  $k-\omega$  and the extended  $k-\epsilon$  models are nearly equal (b, c). Moreover, Denton (mixing length), Bassi-Savini ( $k-\omega$ ) and Onera's CANARI ( $k-\epsilon$ ) (f, g, h) showed quite similar results, thereby suggesting that the turbulence model influences the mean total pressure field less than the grid radial spacing; but Stapleton found the reverse: a change in the turbulence model from Baldwin-Lomax to Spalart-Allmaras made a large difference.

### 3.3.5.3 Radial flow angle

No great differences were displayed and all codes predicted negative flow angles in the wake region and positive flow angles in the mainstream.

### 3.3.5.4 Circumferential flow angle (Fig 3.30)

The plots submitted by the various contributors support the observation that, in general, fine grids are necessary to resolve the details of the vortical structure near the hub. The TRACE-S computation performs well in resolving such details, but even finer grids would be advisable. The flow angle distribution in the relatively larger vortical structure near the tip region is better described, especially by the fine grid computations. The TRACE-S computations on the same grid with the extended  $k-\epsilon$  and the  $k-\omega$  turbulence models do not show significant differences in the circumferential flow angle.

### 3.3.5.5 $\mu_r/\mu$ (Fig 3.31)

These contour plots reveal many surprising facts. The TRACE-S turbulent viscosity computed with different two-equation models (a, b) differs by more than one order of magnitude (even in the mainstream region) and the same observation applies to the TRACE-S and Bassi-Savini results obtained with the same model ( $k-\omega$ ) (a, c). Also CANARI's and TRACE-S's  $k-\epsilon$  results are not similar (b, d), leading the former to much stronger gradients of turbulent viscosity in the wake. Finally, the use of the Michel algebraic model (CANARI) led to a complete disappearance of turbulent viscosity in the measuring plane apart from the endwalls (e). From these results it is hard to extract any meaningful comment on the turbulence models and it is felt that such strange behaviour is mainly due to numerical aspects of the codes employed. Further studies of the implementation of turbulence models in RANS codes seem to be needed.

### 3.3.6 Contour plots in the blade-to-blade planes

Contours of the TRACE-S solution on the O-H-H-H grid show unphysical behaviour at the downstream junctions of grid subdomains and approaching the outflow boundary; this is dramatic for the case of  $P_t$ , shown in Fig 3.32, and  $\mu_r/\mu$  isolines. This happens because the grid is very coarse and diffusive in that region. It illustrates the difficulties inherent in implementing complex grid schemes, and why some code writers avoid them.

All other solutions show results qualitatively similar to each

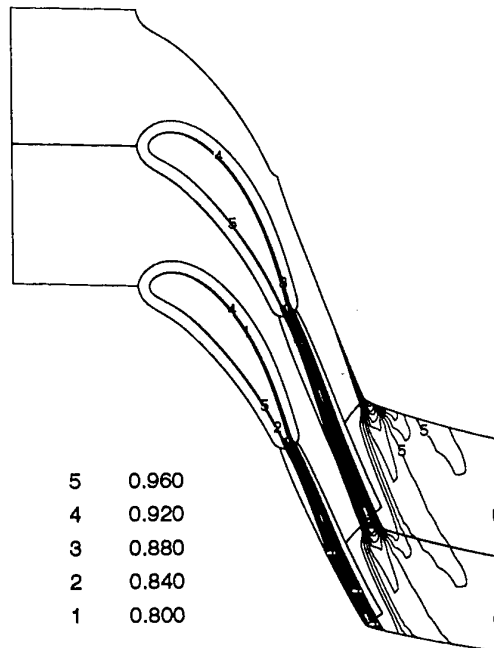


Fig 3.32 Total pressure ratio contours at mid-span:  
TRACE-S with O-H-H-H grid and  $k-\epsilon$  model (Lisiewicz)

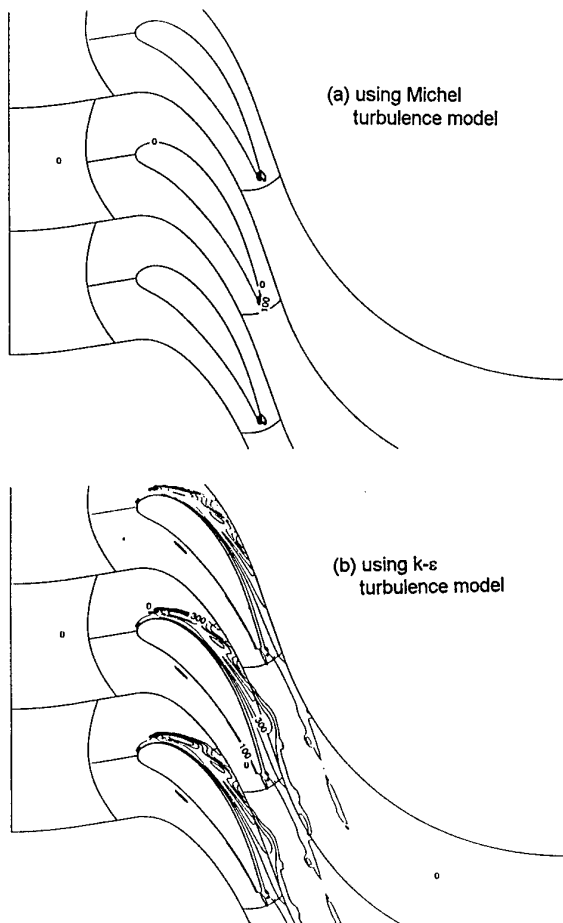


Fig 3.33 Viscosity ratio at mid-span: CANARI using two different turbulence models (Couaillier)

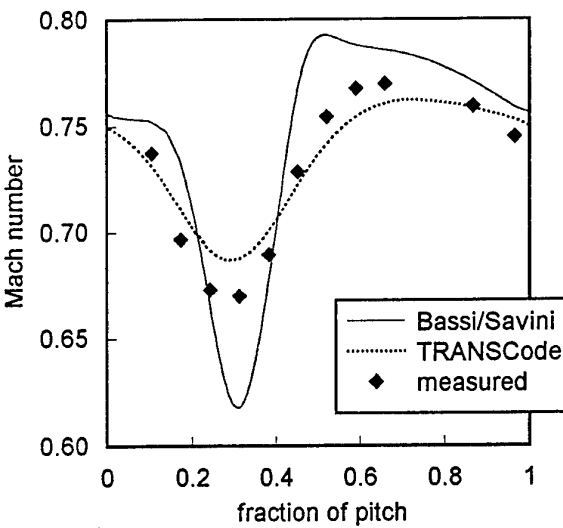


Fig 3.34 Mid-span circumferential Mach number traverses

other. No flow separation is evident on the blade rear suction surface and the highest losses occur in the near hub sections. This is obviously to be ascribed to the highest freestream velocities. Results concerning turbulence characteristics are similar to those discussed in the previous subsection. It is only worth noting how the turbulence model affects the turbulent viscosity in the blade channel obtained with CANARI code. Using the Michel model,  $\mu/\mu$  values are everywhere low (not exceeding 100 even close to the profile) (Fig 3.33a) whilst, using the k- $\epsilon$  model, values are greater (Fig 3.33b) and there is also a marked turbulence production in the suction side acceleration region.

The only two tangential midspan Mach traverses submitted present opposite characteristics: the extent of the wake, that can be associated with the region of deficit in the Mach number profile, covers the whole pitch in the TRANSCode solution and about 40% of the pitch in the Bassi-Savini solution (Fig 3.34); the peak value of deficit in the latter is twice as big as that in the former. (TRANSCode used 49 points across the pitch and Bassi-Savini 37 points.)

### 3.3.7 Assessment

1) The computations performed clearly pointed out the importance of an adequate radial resolution of the mesh. This is of great concern particularly *outside* the endwall boundary layers as they are normally well enough resolved. Moreover, the computations stressed the usefulness of a fully-3D numerical approach when simulating such a flow; it is felt that most of the relevant 3D characteristics cannot be simulated with any type of Quasi-3D model.

2) Global features are much better solved than local features, especially in the near endwall regions where the 3D effects induced by the secondary flows are significant. One way to reduce this shortcoming could be the use of solution-adaptive embedding. Anyway these computations, representative of the state of the art, suggest that nearly 500,000 grid points, adequately distributed, should be sufficient to solve the steady flow field in an annular turbine cascade.

3) Turbulence models are often considered to be the main source of discrepancy in the validation of CFD codes. This is not always true, as in the present case, when grid resolution

and boundary conditions also seem to play a major role. Big differences are still hidden in the numerics rather than in the physical models employed; the differences between the TRACE-S solutions with CH and OHHH grids suggest that difficulties with multiblock grids can occur.

4) The huge scatter in the predicted behaviour of turbulence quantities is surprising. This is believed to be actually more related to the practical implementation of the turbulence models (e.g. evaluation of source terms, clipping of maxima and minima, near-wall treatment, boundary conditions, etc.) than to the physical and mathematical aspects of the models themselves.

Notwithstanding these uncertainties, turbulence models seem to have, in this test case, a moderate influence on the aerodynamic mean flow quantities; however it can be argued that much stronger effects should be visible analysing the mixing process and the wall heat transfer coefficients.

## 3.4 ANALYSIS OF THE COMPUTATIONAL GRIDS

### 3.4.1 Introduction

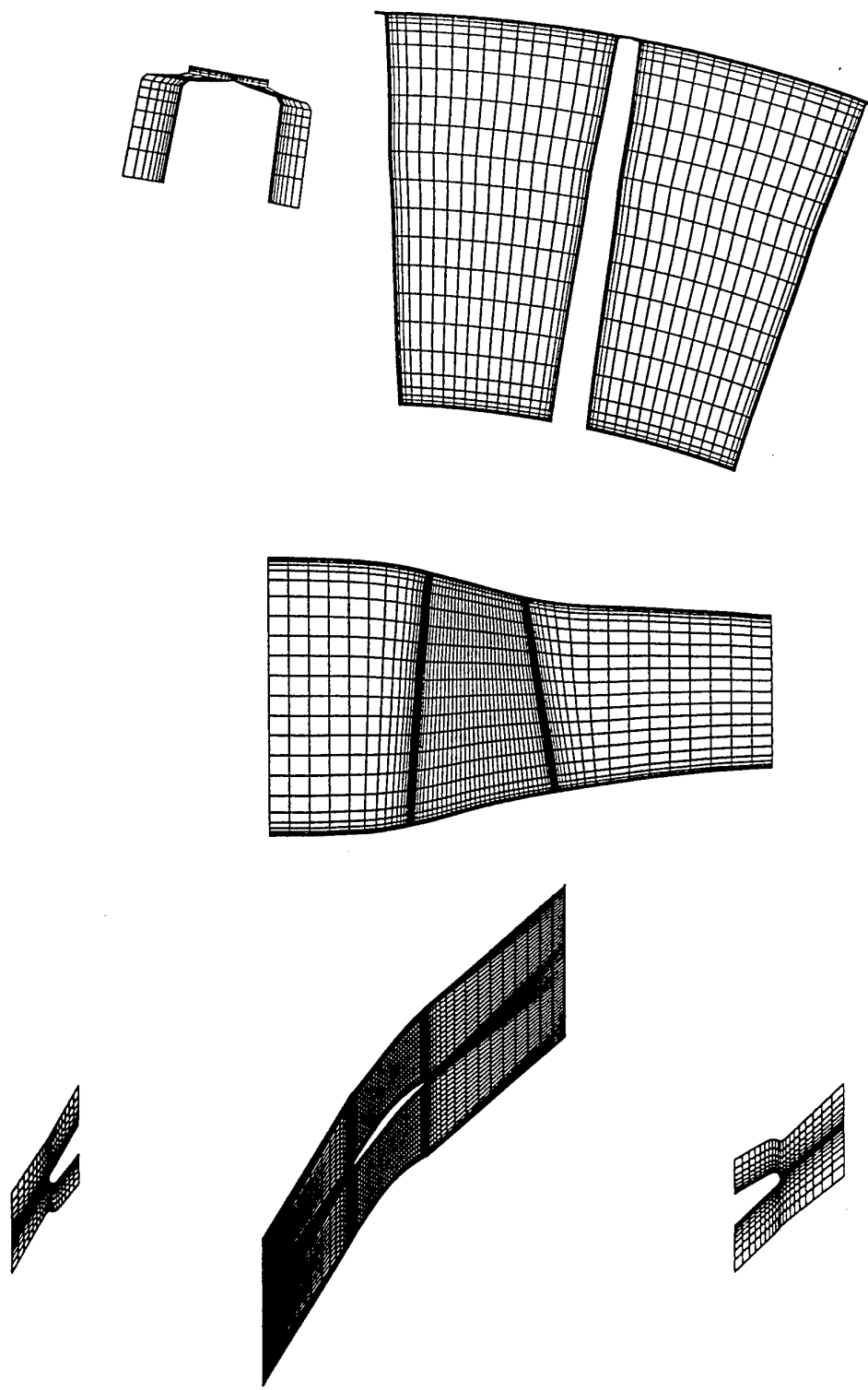
Turbomachinery CFD code developers have found that grid characteristics can have significant effects on the accuracy of a computation. Specifically, those grid characteristics known to have an impact on the solution are:

- grid type
- grid size
- near-wall characteristics, including normal spacing and cell aspect ratio
- grid distortion parameters, including stretching and skewness
- tip clearance treatment.

Discussions of these parameters, and observations of their impact on the accuracy of the simulations are provided in the sections that follow. Reference is made to Table 3.2 which summarizes the grid information for each of the simulations submitted by the WG 26 contributors for the Rotor 37 and DLR cascade test cases. The table presents the grid type, grid size,  $y^+$  normal to the wall spacing, minimum and maximum spacings in each of the coordinate directions, near-surface maximum cell-to-cell spacing ratios (clustering), numbers of leading and trailing edge points, points in the spanwise direction in the tip gap region, maximum cell aspect ratios, maximum skew, number of blocks and minimum and maximum values of the axial coordinate for the solution domain.

### 3.4.2 Grid Type

Brief descriptions of the grid systems used by the WG 26 contributors are given in the ensuing subsections. In all cases, the grids were of the non-adaptive structured type. They are denoted by type as H, I, C and O grids. Many contributors used composites of these grids which were coupled along contiguous boundaries and others used overset grid combinations. All of these 3-D grid systems were constructed by stacking 2-D grids generated on blade-to-blade surfaces of revolution with the hub and tip grids conforming to the flowpath boundaries. It should be noted that composite grids generally reduce the undesirable features associated with grids of a single grid type but that they introduce additional complexity in the flow solver along the component grid boundaries and can lead to non-physical features in the solutions in these areas.



The three main views only have every other line drawn

Fig 3.35 Rotor 37 H grid (Calvert)

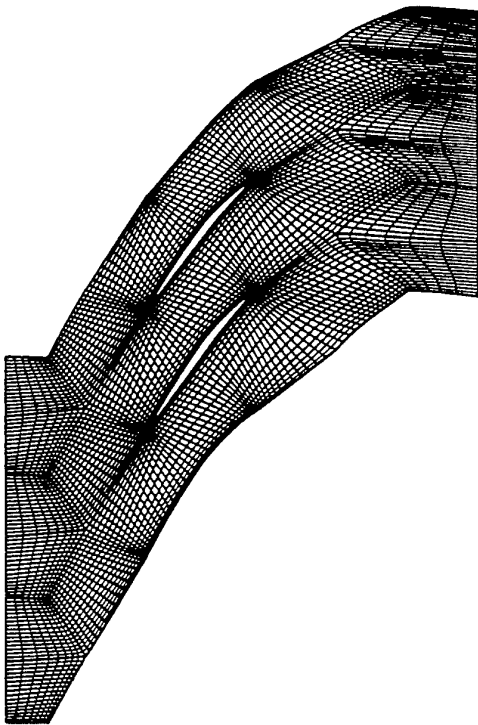


Fig 3.36 Rotor 37 H-I-H grid (Hildebrandt)

#### 3.4.2.1 *H* Grids

An *H* grid is the most widely used grid type for turbomachinery flow calculations and it is preferred by most researchers because of ease of construction. In its simplest form, it is generated with “straight” line segments along the  $x$ ,  $r$  and  $\theta$  coordinate lines using algebraic techniques. To resolve high gradient regions near the airfoil surfaces, hub and casing, and airfoil leading and trailing edges, clustering laws in the form of exponential functions are employed. Generalizations of the *H* grid with curved grid lines which reduce shear and increase airfoil leading and trailing edge resolution have been used by some researchers. The primary drawback with *H* grids is the high grid shear inherent with compressor airfoils at high setting angles and turbine airfoils with high turning. Another disadvantage is that grid independent solutions are difficult to achieve because as the grid is refined, the near-leading-edge and trailing-edge grid cells become more highly sheared which introduces large metric gradients and additional discretization errors into the solution. As a result of this leading- and trailing-edge behavior, highly accurate *H* grid simulations are generally only achieved by very experienced users who have extensive background in generating acceptable *H* grids. The *H* grid is generally better suited for compressor computations than turbine computations because the compressor airfoils are normally thinner and produce less shear around the airfoil leading and trailing edges. Calvert, Denton, Shabbir and Hutchinson used this grid type for Rotor 37 simulations and Stapleton and Denton used it as well for the DLR cascade test case. The Rotor 37 *H* grid employed by Calvert is shown in Fig 3.35.

#### 3.4.2.2 *I* Grids

*I* grids were introduced to reduce the undesirable grid shear inherent with *H* grids. They are normally constructed with algebraic techniques which align the blade-to-blade grid lines in the direction normal to the streamwise grid lines. *I* grids

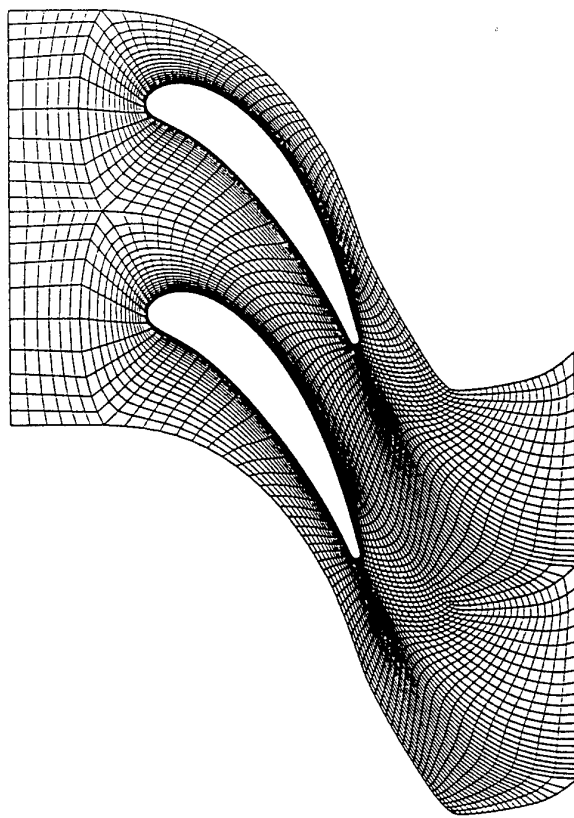


Fig 3.37 DLR cascade H-C grid (Lisiewicz)

substantially reduce grid shear but introduce complications for the flow solver along the grid periodic boundaries where the grid lines are generally not continuous and not periodic. An additional difficulty is introduced at the upstream and downstream boundaries in the specification of boundary conditions because those boundaries are skewed relative to the axial planes utilized with *H*-type grids. Hah employed *I* grids for his DLR cascade and Rotor 37 calculations. Hildebrandt devised a novel periodic composite *H-I-H* grid for Rotor 37, shown in Fig 3.36, which had none of the undesirable features normally associated with *I* grids, being periodic, continuous along the periodic boundaries and having axial grid planes at the upstream and downstream boundaries for ease of specification of inflow and outflow boundary conditions.

#### 3.4.2.3 *C* Grids

*C* grids wrap around the airfoil leading edge in a “C” pattern and have the desirable feature of providing a blade conforming orthogonal grid in that region for improved resolution of high leading edge flow gradients. Similar to *H* grids downstream, they align with the flow direction in that region for good wake definition. Disadvantages of *C* grids are: (1) they are limited in the distance which they can be extended upstream of the airfoil row, and (2) they become more sparse with distance upstream - which can be a concern for compressors operating at supersonic inlet conditions with respect to resolving shock strong waves propagating upstream. *C*-type grids are normally constructed with elliptic grid generation techniques. Periodic *C* grids were employed by Bassi/Savini, Dadone/DePalma, and Chima for the DLR cascade. Non-periodic *C* grids with non-contiguous points along the wake cut were used by McNulty for the DLR cascade and by Arnone for Rotor 37. The block composite

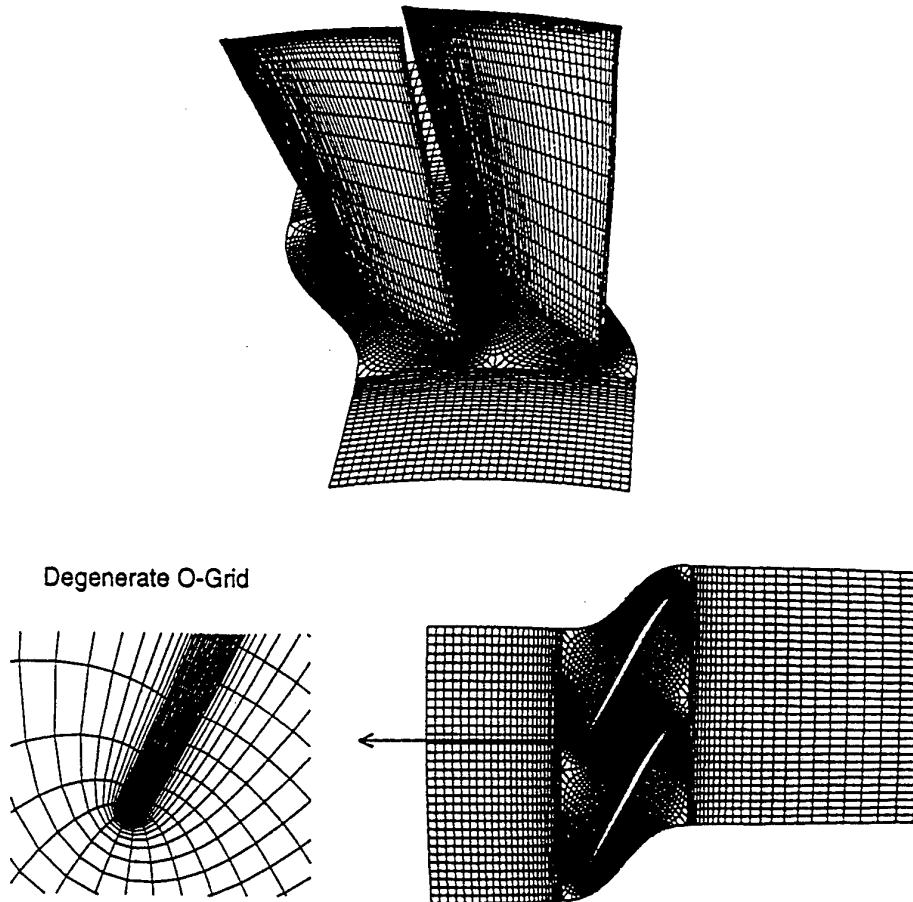


Fig 3.38 Rotor 37 H-O-H grid (McNulty)

periodic H-C grid shown in Fig 3.37 was used by Lisiewicz for the DLR cascade with an H grid extension upstream.

#### 3.4.2.4 O Grids

O grids wrap around the airfoil and have one family of grid lines conforming to the airfoil surface. With sufficient grid density, they can be used to provide high resolution of both leading- and trailing-edge flows. Typically, O grids are orthogonal or nearly orthogonal along the airfoil surface, thereby minimizing the undesirable grid shear inherent with H type grids. They share the same disadvantages of C grids in that they are limited in the distance they can be extended upstream and downstream and they become sparse with distance upstream and downstream. There is an additional concern with the latter feature downstream as it is desirable to maintain tight clustering in the wake region. Some researchers have tried to circumvent this problem by moving the O grid downstream boundary closer to the airfoil to maintain a high density mesh locally in the trailing edge region and adding a high density H grid downstream. Others have used O grids only in the local region of the airfoil and coupled separate H grids upstream, downstream and within the airfoil passage. Like C grids, O grids are normally constructed with elliptic grid generation schemes. It is generally accepted that O grids are best suited for turbine

airfoils because they can be used to define large trailing edges accurately as is needed to predict the airfoil base pressure. Couaillier used non-periodic H-O-H grids for the Rotor 37 and DLR test cases and for Rotor 37 he also investigated a local O grid coupled with a background H grid along a contiguous patched grid boundary. McNulty employed the H-O-H grid and the degenerate O grid in the tip clearance shown in Fig 3.38 for Rotor 37. Lisiewicz performed a calculation of the DLR cascade with a novel periodic O-H-H-H grid consisting of 4 separate grids coupled along patch boundaries. Weber used an overset O-H grid, shown in Fig 3.39, which did not suffer from the undesirable O-grid "corners" in patched O-H grid systems. With this system, the grid cell sizes in the O and H grids in the overset region are maintained approximately the same to ensure accurate transfer of boundary data between the grids by interpolation.

#### 3.4.2.5 Conclusions on Grid Type

In the computations for Rotor 37 and the DLR cascade undertaken for WG26, no single grid type stood out as being superior to the others. In general, the O and C grids provided the best definition of the airfoil leading edge and gave the best resolution of the leading edge flow gradients and the bow shock structure for Rotor 37. One exception to this

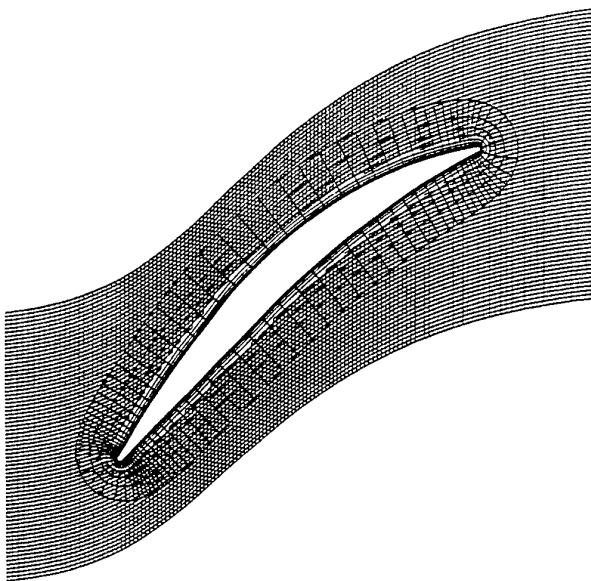


Fig 3.39 Rotor 37 overset O-H grid (Weber)

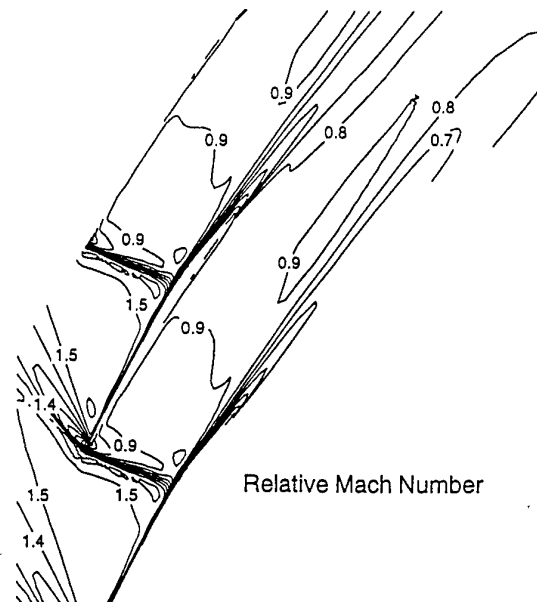


Fig 3.40 TRACE-S Rotor 37 relative Mach contours at 90% span and 98% choke flow (Hildebrandt)

generalization was the Rotor 37 simulation of Hildebrandt performed on the H-I-H grid shown in Fig 3.36 with only 4 points defining the leading edge. In this case, excellent shock resolution, shown in Fig 3.40, was achieved by aligning the grid lines in the blade-to-blade surfaces along and normal to the mean flow directions, thereby aligning the grid lines parallel and normal to the passage/bow shock system. With the exception of the near hub region, Hildebrandt's prediction showed remarkably good agreement with the experimental spanwise profiles of total pressure, total temperature and adiabatic efficiency. His overall total pressure predictions also showed good agreement with the measurements over the entire speed line. It should be noted, however, that the excellent results achieved in this case were likely the result of aligning the grid lines with the dominant shock features and, therefore, that it may be difficult to achieve comparable levels of accuracy for all airfoil shapes and flow conditions with this grid system.

In a related investigation on leading edge flow resolution, Arnone performed a Q3D study of the effect of leading edge definition for Rotor 37 with a C grid in which he varied the number of points around the leading-edge circle from 4 to 40. He determined that the predicted total pressure rise characteristic changed monotonically with increased resolution and converged to a single characteristic with 20 points around the leading edge. However, the necessary number of points must surely depend on the type of leading edge flow, the transition assumption and the turbulence model used.

Unfortunately, neither the Rotor 37 nor the DLR cascade test cases provided airfoil surface data needed to determine the effect of leading edge definition on the airfoil surface flow conditions properly. It is well known that any errors incurred at the leading edge show up as entropy increases which convect back onto the airfoil surfaces and adversely affect the quality of the solution over the entire surface. Additionally, any errors on the pressure and suction surfaces generated at the leading edge combine downstream to affect the wake prediction. Because of the potential significance of the leading edge flow modeling on the accuracy of the cascade

flow simulations, further experimental/computational studies are recommended. For these investigations, 2-D cascade experiments and computations are recommended in order to eliminate any 3-D effects which could mask leading edge effects.

Weber's remarkably good results for Rotor 37 may be attributable, at least in part, to the use of the overset O-H grid system shown in Fig 3.39. This grid does not suffer from the undesirable sharp O-grid "corners" inherent with patched O-H grid systems where metrics gradients are large and the grids are sparse. With the overset O-H grid system, the grid cell sizes in the O and H grids in the overset region are maintained at nearly the same levels for good interpolation data transfer between grids and the metric variations in both grids are smooth throughout. Also on the endwall, the use of the "background" H grid in the overset O-H grid system ensures smooth development of the endwall boundary layers entering the bladed region, which may be a significant factor with respect to predicting the hub suction surface separation observed with Rotor 37. The primary drawback for the use of the overset O-H system is that the flow solver is non-conservative as a result of the required interpolation procedures used to transfer data between the grids. For the Rotor 37 test case, however, these procedures appeared to result in no appreciable negative impact on the solution.

Regarding the airfoil trailing edge flow and the wake structure, the C, I and H grids that align with the wake generally provided the best wake definition. These grids have one family of grid lines aligned with the wake and have a large number of points across the wake. The O grid solutions, on the other hand, provide high resolution of the local trailing edge wake structure but rapidly diffuse the gradients as the grid opens up downstream of the trailing edge. For turbines, the "best" grid for trailing edge flow and wake resolution is considered by some WG 26 members to be the H-O-H grid which can be used to provide sufficient local trailing edge definition to predict the airfoil base pressure and H-grid alignment with the wake downstream to resolve the wake structure, though that conclusion is not based on the results of the DLR cascade case.

### 3.4.3 Grid Size

A number of investigators studied the effect of grid size or grid fineness on solution accuracy. In general, these studies showed that a moderate grid of 200,000 points was needed to capture overall performance characteristics and that much finer grids with as many as 1,000,000 may be needed to isolate the detailed flow features such as endwall secondary flows and tip clearance flows. If wall functions are used, less grid points are needed near the walls, so less points are needed overall.

McNulty studied the effect of grid size for the DLR cascade test case. He employed three C grids with approximately 160,000, 300,000, and 1,200,000 points. The two variations from the baseline 160,000 point grid: (1) doubled the number of radial grid points, and then (2) doubled the number of normals along the airfoil surface and C contour grid lines, respectively. McNulty determined that at least 49 grid points, which he used in the radial direction with the finer meshes, were needed to represent the endwall secondary flows near the hub and casing. This study also showed that even more points were needed in the radial direction to fully capture the endwall secondary flow vortices. The DLR cascade solutions by Lisiewicz on C-H and O-H-H grids, both with 117 points in the radial direction, confirmed this finding and suggested that even finer grids in the radial direction may be needed to match the data.

Stapleton studied the effect of grid size for the DLR cascade with H grids. He used a baseline 135x49x49 grid with approximately 325,000 points and variants with: (1) more than twice the number of points (117) in the radial direction, and (2) 24% more in the axial and 49% more in the circumferential and radial directions. He found that all grids produced nearly the same pitchwise-average performance and that the total pressure contours for all of the solutions qualitatively matched the measured contours, but that the fine radial grid solutions gave slightly better definition of the near endwall secondary flow structure.

McNulty also looked at the effect of grid size on solution accuracy for Rotor 37 using H-O-H grids with degenerate O grids in the tip clearance region. Three grids with approximately 200,000, 400,000 and 350,000 points were studied to look at the effect of first marginally increasing (20%-40%) the grid size in each direction and then doubling the number of points only in the radial direction from the baseline 200,000 point grid. In each case, nine points were used in the radial direction in the tip clearance region. All of these solutions gave remarkably similar pitchwise-average performance predictions.

### 3.4.4 Near-Wall Characteristics

Those grid properties locally affecting solution accuracy in the region of the wall shear layers are the spacing normal to the wall and the cell aspect ratio. A general normal-to-the-wall grid spacing guideline for calculations that solve down to the wall and enforce no-slip wall boundary conditions is to maintain a normal spacing,  $y^+$ , of less than 1.0, which ensures that the first point off the wall lies within the viscous sublayer of the boundary layer. However, it depends on the turbulence model used. None of the contributors who solved down to the wall reported  $y^+$  values less than 1 throughout, and only a few maintained  $y^+$  levels less than 10 at every wall point.

For those computations employing wall functions without solving down to the wall, the accepted guideline is to place the first point off the wall within the fully turbulent inner

region of the boundary layer with  $y^+$  values of the order of 50. Most contributors employing wall functions adhered to this guideline and reported  $y^+$  values between 20 and 60.

Cell aspect ratios near the airfoil and endwall surfaces can become extremely large as points are clustered in those regions. This is especially true with those solvers that do not employ wall functions, but rather solve down to the wall. Typical maximum cell aspect ratios reported from those contributors not employing wall functions ranged from approximately 200 to 800. In general, for those contributors employing wall functions, the reported maximum cell aspect ratios were less than 100.

### 3.4.5 Grid Distortion Parameters

Grid distortion, which can have an adverse effect on solution accuracy, can be characterized by the degree of grid stretching in any coordinate direction and the degree of grid skewness or shear between any two coordinates.

Normally, turbomachinery grids are clustered toward the walls to resolve the endwall and airfoil surface boundary layers without incurring the large CPU times required for calculating the flow on a uniformly distributed dense mesh. All of the WG 26 contributors utilized grid stretching to cluster points near those surfaces. This approach is acceptable for small mesh stretching ratios (cell-to-cell size ratio); however, it does introduce error into the solution that is proportional to the degree of stretching for a given code. In general, it is accepted that the cell-to-cell size ratio should not exceed a value of 1.3. Most contributors who reported grid clustering information stayed within this guideline.

Grid skewness is known to have adverse effects on the accuracy and stability of a numerical solution. That is, as the skewness or shear increases, the accuracy decreases and the solution becomes less stable. For the purpose of this study, maximum skew, as reported in Table 3.2, is defined as the minimum angle between the surface and the grid line extending away from the surface. In all cases, it was assumed that the maximum skewness occurred on the airfoil surface. In general, the H- and C-type grids produced the most grid shear with it occurring at or near the trailing edge of the airfoil. Stapleton reported a minimum skew angle of about 4° for his H-grid DLR cascade solutions and Calvert 21° for his H-grid Rotor 37 solution. Likewise, Chima reported low skew angles of 18 and 30° for his C-grid DLR cascade and Rotor 37 solutions, respectively. I grids employed for Rotor 37 computations by Hah and Hildebrandt produced much less shear with reported skew angles of about 60° for each. The O grid employed by Lisiewicz for the DLR cascade had no shear with a reported minimum skew angle of 90°.

Grid distortion tolerance probably depends partly on the code; for example cell vertex methods may be more tolerant than cell centred schemes.

### 3.4.6 Tip Clearance Treatment

A number of different treatments have been employed to model the flow through the tip clearance region in rotors. These range from the simplest so-called "pinched-tip" model to more elaborate fully gridded models. The pinched grid model treatments reduce the airfoil tip to zero thickness in one mesh spacing and employ just a few points in the clearance region. The rationale for this very simple model is the fact that the tip clearance flow is dominated by inviscid effects and can be approximately computed knowing the pressure difference across the blade tip. These models are easily implemented with H grids where the grid lines on the

pressure and suction surfaces are aligned in the circumferential direction. Normally the computational tip gap is not the same as the actual gap size but is determined by numerical experimentation in order to allow for the vena contracta. Rotor 37 computations by Calvert, Denton and Shabbir employed the pinched-tip model. Hutchinson performed two calculations using the pinched-tip treatment with 4 and 6 nodes in the tip gap.

The fully gridded tip treatments attempt to model the actual airfoil tip shape and the clearance region. McNulty and Couaillier employed degenerate O grids in the tip clearance for Rotor 37 that were patched along the airfoil surface to the passage O grids along contiguous patch grid interfaces. In these cases, about 10 grid points were used in the radial direction. Hildebrandt studied the effect of number of points in a fully gridded H grid treatment in the tip gap for Rotor 37 and performed calculations with 4 and 7 points in the radial direction.

A study by Chima (1996b) showed relatively little difference between simple and sophisticated approaches to the grid in the tip clearance region.

Because of the lack of detailed flow measurements and computational results in the tip clearance region for Rotor 37, it was not possible to determine the precise impact of the tip clearance modeling on the flow solutions. It was generally felt by the Working Group members that the fully gridded models provided a better basis for predicting the tip clearance flow than the "pinched tip" models, especially for predicting the tip clearance losses. However, in some cases, the predictions with the "pinched tip" models produced better agreement with the experimental spanwise profiles of total pressure and efficiency than the fully gridded models. Additional experiments and supporting computations are needed to determine the impact of the tip clearance model on the global simulation more clearly.

### 3.5 ANALYSIS OF THE ALGORITHMS

In Chapter 1, the various algorithms used for turbomachinery computations were reviewed. They fall into two classes: time marching and pressure correction. Within the time marching class, used by most contributors, there are many variations. The turbomachinery CFD specialists have generally adopted algorithms proposed by external aerodynamics research workers, and unlike the recent Fluid Dynamics Panel meeting (AGARD, 1995) turbomachinery CFD meetings have rarely discussed this aspect of their work.

Initially, the time marching algorithms were only applicable to compressible flows with Mach number above about 0.3, and that limitation applies to many of the codes employed for the WG, while the pressure correction codes were limited to subsonic flow. More recently, these limitations have been overcome, but that has not made specialists switch their chosen approach.

The choice of algorithm is made to achieve fast and rapidly convergent computations, and the present WG has focused on accuracy rather than speed or stability. It is generally believed that the choice of algorithm has little influence on accuracy, all solutions of the same equations converging - if they converge at all - to the same results, within engineering accuracy.

The question of computational speed is difficult to judge in a study of this kind, because of the wide variety of computer

hardware used. The codes were often run on a network, so that the true running time is not known. The WG has made no attempt, therefore, to rate relative speeds.

From the contributions made to WG 26, there is no basis for assessing the relative merits of the schemes used in the various codes.

### 3.6 ANALYSIS OF THE TURBULENCE MODELS

It is quite difficult to compare the different turbulence models employed, since some of the differences between the various computations of the DLR cascade are believed to depend on the grids and flow solvers used rather than on the turbulence models. So the turbulence models are compared for that case only under the same conditions, i.e. when using the same code and grid.

#### 3.6.1 Mixing length models

Kang and Hirsch

Code	EURANUS/TURBO
Test case	Rotor 37
Model description	The Baldwin-Lomax (1978) algebraic turbulence model is used. All the constants of the model are the standard ones except $C_{wk}=1.0$ .
Model Implementation	In EURANUS/TURBO, $y_{max}$ is the value of $y$ corresponding to the maximum of $F$ .
Transition model	No transition model. Fully turbulent flow is assumed.

The pitchwise average total pressure and temperature and flow angle exhibit some of the experimental radial variations, particularly in the hub region. Other authors, using the same Baldwin-Lomax model, with similar quantity of mesh points have produced results with a linear variation in this hub region. According to the authors, these better simulations may be associated with the model implementation, and the  $y_{max}$  definition. They suggest that other similar codes take the  $y_{max}$  corresponding to the  $F$  maxima furthest away from a wall. The treatment of separated wall layers could be improved for this reason.

The radial distributions agree with the observations presented in paragraph 3.2.3. The ratio between the computed choked mass flow and the measured one is 0.993. The increase of the computed axial velocity at mid-span ( $R=0.22m$ ) at station 4 can be estimated with the following observations:

- The stagnation temperature is correct
- The absolute flow angle is underestimated by  $3^\circ$

The ratio of axial velocity is then  $V_z \text{simul}/V_z \text{exp} = 1.113$ . This means that a large amount of flow blockage is generated at the tip and hub walls as seen in Kang's plots of the efficiency and entropy. Note also that the mesh is coarse for station 4, so that some numerical dissipation exists between the blade trailing edge and station 4.

A large amount of entropy is generated along the line of interaction between the leakage flow and the primary flow. A second zone of high entropy is also observed on the suction side, after the passage shock. This is connected with a strong local aerodynamic blockage for  $V_z$ . It is remarkable that the turbulent viscosity has a medium value after the impact between the 3D leakage "vortex" and the passage shock ( $\mu_t$

$/\mu=150-250$ ). The largest value of the turbulent viscosity is observed further from the tip wall, near the suction side, as a probable consequence of the separated layer, and the strong radial migration towards the tip wall ( $\mu/\mu=700-940$ ).

Note also that preliminary results of the authors with  $C_{wk}=0.25$  (the originally proposed value of Baldwin-Lomax) generate a large separation on the blade suction side.

### Chima

Code	SWIFT - multiblock
Test case	Rotor 37
Model description	The simulation neglects the viscous terms in the streamwise direction, according to a thin layer approximation. The 3D results have been obtained with the Baldwin-Lomax model (1978). All the constants of the model are the standard ones except $C_{cp}=1.216$ and $C_{Kleb}=0.646$ which were shown to give a better agreement with the Cebeci-Smith model (Chima, Giel, and Boyle, 1993). The adapted model predicts the stall point better than the original implementation (Chima, 1996a). 2D results at 70%h have been obtained also with the k- $\omega$ Wilcox's turbulence model (1994).
Model Implementation	The turbulence model is adapted in the clearance region. The inner formulation is used near the blade tip and the casing. A constant outer turbulent viscosity is used across the rest of the gap. For the outer formulation, $F_{max}$ is taken as the maximum of the function F across the entire gap, and $Y_{max}$ is taken as the distance to the nearest of the tip or casing walls. In corners, the distance is computed with Buleev's formulation for the inner layer. For the outer layer, the classical distance is used.
Boundary conditions	Integration down to the wall.
Transition model	The hub and casing walls are assumed fully turbulent. The blade boundary layers are allowed to undergo transition using the model proposed by Baldwin-Lomax. The turbulence is activated if $\mu/\mu>14$ .
Special wake treatment	The wake model of Baldwin-Lomax is used.

At mid-span, for 98% of the choked mass-flow, the radial plots in station 4 show an overestimate of the stagnation temperature, while the absolute flow angle is correct. This suggests that the predicted axial flow velocity is too high. This is consistent with a large amount of loss near the tip wall, that produces a low efficiency.

The gradients of stagnation pressure are smoothed out in the lower 50% of the span. The good overall efficiency results from a balance between an overestimate by 2% at mid-span, while the losses are too high near the tip wall. The increase

of mesh density in the radial direction from 63 to 96 lines improves the stagnation pressure and temperature gradients in the 40-85% region.

The blade-to-blade plot of  $M_{rel}$  shows a passage shock which is too strong.

The 2D simulations of the blade-to-blade section at 70% height with the k- $\omega$  and Baldwin-Lomax turbulence models do not show significant differences in the wake profiles. However, the  $\mu$  contours obtained with Wilcox's model are smoother than with Baldwin-Lomax's model; the non-zero  $\mu$  values are also concentrated in the wakes.

### Chima

Code	RVC3CD
Test case	DLR cascade
Model description	Baldwin-Lomax model with $C_{cp}=1.216$ , $C_{Kleb}=0.646$
Transition model	as for SWIFT

### Arnone and Marconcini

Code	TRAF3D
Test case	Rotor 37
Model description	Baldwin-Lomax's model, with $C_{wk}=1.0$ Chima, Giel, Boyle's (1993) model, Cebeci-Smith's model
Transition model	No transition model

The three turbulence models (Baldwin-Lomax, Chima-Giel-Boyle, Cebeci-Smith) give the same overall pressure ratio. The absolute flow angle is correct from 10 to 80% of the blade span. In this region, the stagnation pressure and temperature are too high in the prediction. This suggests an excess of the axial velocity component, induced by too many losses near the tip wall, as shown by the efficiency distribution.

The wake deficit is also too high at mid-span in station 3. However, because of the excess of work input, the efficiency is correctly predicted in this region.

### Dadone & De Palma

Code	
Test case	DLR cascade
Model description	Baldwin-Lomax's model + Degani-Schiff modification

### McNulty

Code	ADPAC
Test case	Rotor 37 & DLR cascade
Model description	Baldwin-Lomax's model + wall functions
Transition model	No transition model

For Rotor 37, the radial plots at 98% of the choked mass flow include the relative velocity W and the relative flow angle  $\beta$ . There is a low value of W over the whole span, and simultaneously a low  $\beta$  value except at mid-span where the prediction is good. The blade-to-blade plots of relative Mach number show low predicted values downstream of the shock. This induces a high temperature, particularly near the end

walls. The axial velocity component must then be low all over the span. This reduction of the axial velocity is estimated at -3.8%. This is a surprisingly low value, that does not fit with the mass flow.

The radial plots at the near stall condition show a good agreement with the measured values, except for  $P_o$  under 30% of the blade height. The blade-to-blade plots of  $M_{rel}$  show a strong detached shock, behind which the predicted level of  $M_{rel}$  is correct.

Hall has presented good results in the hub region, by increasing the number of nodes in the radial direction from 49 to 97. The effect of an upstream cavity is observed only with this new fine grid, as a consequence of a strong corner stall.

#### Calvert and Stapleton

Code	TRANSCode
Test case	Rotor 37 & DLR cascade
Model description	Baldwin-Lomax's model, with $C_{wk}=1.0$
Model Implementation	Calculation is based on the nearest wall
Boundary conditions and implementation	Log-law is applied to the viscous forces on the wall cells for $y^+ > 5$
Transition model	The flow is assumed fully turbulent
Special wake treatment	The turbulent viscosity is assumed constant in the wake

A full description of the BL implementation is given in Chapter 1; in addition, the search for  $F_{max}$  is limited in order to avoid spurious values. The parameter  $C_{wk}$  was found to have a large effect on the solutions. For example, for a quasi-3D solution of the mid-span section of Rotor 37, the variation of  $C_{wk}$  from 0.25 to 1.0 produces a strong decrease of the exit Mach number and hence an increase in pressure ratio from 1.763 to 2.125, with a corresponding increase in efficiency from 82.3% to 86.3%. The value  $C_{wk} = 1.0$  was used for the 3D solutions and this produced some over-prediction of temperature ratio as well as pressure ratio. Owing to the high loss near the tip wall, the axial velocity is perhaps overestimated at mid-span.

The contour plots of the turbulent viscosity show a strong influence of the tip wall at 90% of the blade height, that is amplified at the near stall condition.

For both cases, calculations were also performed with the Spalart-Allmaras (SA) model (see Section 3.6.2). Looking at the radial profile of total pressure it seems that in the tip region the BL model does a better job, but the contours of total pressure in the measuring plane predicted by the SA model are closer to the experimental ones, with a more pronounced distortion of the wake. Moreover, the SA radial distribution of the tangential flow angle is in fairly good agreement with the experiment, even in the tip region. It is worth mentioning that, with the SA model, the code converged better (even if more slowly) without needing the damping in the  $\mu_t$  changes sometimes required by the BL model.

#### Shabbir

Code	VSTAGE
Test case	Rotor 37
Model description	Baldwin-Lomax algebraic turbulence model
Transition model	transition at 10% of suction surface; fully turbulent pressure surface

A full set of results is given in Shabbir, Zhu, and Celestina (1996). There is a good prediction of the radial variation of the absolute flow angle  $\alpha$ , while the temperature is slightly overestimated. This is consistent with a high axial velocity at mid-span, probably created by a flow blockage near the tip wall. See Section 3.2.3 for a comparison with two  $k-\epsilon$  models.

#### Couaillier

Code	CANARI
Test case	Rotor 37 & DLR cascade
Model description	Michel's model
Model Implementation	Definition of the boundary layer thickness in term of a specific amount of the vorticity. The distance to the wall is determined from Buleev's formulation.
Transition model	fully turbulent
Special wake treatment	no wake model

For Rotor 37, the turbulent viscosity disappears in the wake for the mesh points far from the casing. The losses generated near the casing are very large compared with other simulations.

For comments on the DLR cascade results, see Section 3.6.3.1.

### 3.6.2 One equation models

#### Calvert and Stapleton

Code	DRA TRANSCode
Test case	Rotor 37 & DLR cascade
Model description	Spalart-Allmaras' model

The same boundary conditions were used as for the Baldwin-Lomax model. The kinematic eddy viscosity is prescribed at the inlet according to a typical turbulent wall boundary layer, is extrapolated at the outlet, and the profile boundary layer is tripped to turbulence near the leading edge. The Rotor 37 results are changed significantly compared with the Baldwin-Lomax solution, with the pressure ratio now being underestimated, in a similar way to the CANARI results with this model. The reason seems to be that the interaction of the passage shock with the suction surface boundary layer is overestimated over the outer half of the span. The Spalart-Allmaras model has been used with success on a fundamental test case for 3D shock-boundary layer interaction (Delery), and so it is possible that the predicted pre-shock boundary layer is incorrect. The model does give some indication of the hole in the total pressure profile near the hub, suggesting a better prediction of the sensitivity of the flow in this region.

For discussion of the results on the DLR cascade, see Section 3.6.1

### Couaillier

<b>Code</b>	<b>CANARI</b>
<b>Test case</b>	Rotor 37
<b>Model description</b>	Spalart-Allmaras' model

The results have been obtained with the same grid as for the mixing length and k- $\epsilon$  models. Spalart's model does not show any improvement, compared with the other models, and does not perform better than the mixing length model.

### Weber

<b>Code</b>	<b>OVERFLOW</b>
<b>Test case</b>	Rotor 37
<b>Model description</b>	Spalart-Allmaras' model with a modification for the strong local rotation from Dacles and Mariani (1995)

The turbulence production term was calculated using  $P = S \cdot \text{MAX}(0, W \cdot S)$ , where  $S$  = strain rate tensor,  $W$  = vorticity. Although  $S$  and  $W$  are very close in thin shear layers (close to any solid wall, in general), using  $S$  in the production term produced a different solution from using  $W$  or this combination of the two.

Using an overset O-H grid, remarkably good predictions of the spanwise distributions of pressure and efficiency were obtained except near the tip, *without modelling the hub leakage flow*.

### 3.6.3 Two-equation models

#### 3.6.3.1 Low Reynolds number models

### Couaillier

<b>Code</b>	<b>CANARI</b>
<b>Test case</b>	Rotor 37, DLR cascade
<b>Model description</b>	k- $\epsilon$ of Jones-Launder
<b>Model Implementation</b>	Integration to the wall, cut-off for $k$ and $\epsilon$ (zero machine) and limitation of $\mu_t / \mu > 5000$
<b>Boundary conditions</b>	$k=0, \epsilon=0$ at the wall. $k$ and $\epsilon$ prescribed upstream. $k$ and $\epsilon$ extrapolated downstream
<b>Initialisation</b>	From the algebraic results, $k$ and $\epsilon$ are deduced from $\mu_t$ and Bradshaw's relations with a local equilibrium assumption.
<b>Solution strategy</b>	The k- $\epsilon$ equations are decoupled from the mean flow equations
<b>Transition model</b>	No
<b>Special wake treatment</b>	Included in the turbulent equations

For Rotor 37, the k- $\epsilon$  simulation provides better radial profiles of stagnation pressure and temperature than the Michel model (see Section 3.6.1, Couaillier). The level of stagnation temperature is however slightly too high, particularly above 60% of the blade span. This is also observed for the stagnation pressure which is slightly above the experimental values while the agreement is very good in between 30 and 60% of the blade height. The losses are however too high near the tip wall, although a large reduction

of the losses is observed with the use of the k- $\epsilon$  model compared with Michel's model.

The turbulent viscosity ratio reaches a high value in the wake at mid-span (1200), and a lower value near the casing on the pressure side (700). A small pocket of high turbulent viscosity occurs in the interaction of the leakage "vortex" and the passage shock.

Interestingly enough the k- $\epsilon$  field was decoupled from the mean flow field, computing it with the updated values of the mean flow at each time step. The same strategy was applied in the TRACE-S code and is probably done in order to relieve stability problems.

For the DLR cascade, the radial profile of circumferential flow angle seems better captured by the k- $\epsilon$  model; on the other hand it predicts a less satisfactory  $P_t$  profile, overestimating the losses. Peaks in the isolines are better defined with the algebraic model, particularly the loss core in the hub region; on the contrary, the shape of the wake is less satisfactory. Also in this case the huge difference in the turbulent viscosity (using the two-equation model it is much greater) does not produce a clear trend; for example using Michel's model the wake is a little thicker, but peaks in the contour lines are sharper.

### Hah

<b>Code</b>	<b>HAH3D</b>
<b>Test case</b>	Rotor 37 & DLR cascade
<b>Model description</b>	k- $\epsilon$ with Chien's low Reynolds number modification (1982)
<b>Model Implementation</b>	Integration to the wall when $y^+$ is less than 11. Wall functions are used when $y^+$ is greater than 11. No limitation or artificial cut-off for $k$ and $\epsilon$ .
<b>Boundary conditions</b>	$k=0, \epsilon=0$ at the wall $k$ and $\epsilon$ are prescribed upstream using data or local equilibrium conditions $k$ and $\epsilon$ are extrapolated downstream
<b>Initialisation</b>	Uniform distributions of $k$ and $\epsilon$
<b>Solution strategy</b>	Fully coupled
<b>Transition model</b>	Criteria based on low Reynolds number modification
<b>Special wake treatment</b>	None

For Rotor 37, the turbulence model used with the current numerical procedure calculates the hub-corner flow separation both at 98% and 99% choked mass flow. The numerical solution at 99% mass flow agrees very well with the measured data. The code strongly underpredicts the losses at mid span, and produces as a consequence too high a level of efficiency and pressure ratio.

### 3.6.3.2 Models with wall functions

#### Lisiewicz

<b>Code</b>	TRACE-S
<b>Test case</b>	DLR cascade
<b>Model description</b>	Two versions of k- $\epsilon$ model and one k- $\omega$ model
<b>Model Implementation</b>	see below
<b>Boundary conditions</b>	see below
<b>Transition model</b>	assumed fully turbulent
<b>Special wake treatment</b>	None

Three two-equation turbulence models were tested: the standard k- $\omega$  (Wilcox) and k- $\epsilon$  (Lauder and Spalding) models, and the Kato-Launder version of the latter. Both the k- $\epsilon$  and k- $\omega$  models use Spalding's law of the wall in the first computational cell; at the inflow  $k$  is prescribed from turbulence intensity whilst  $\epsilon$  and  $\omega$  are set specifying a characteristic turbulence length scale; at the outflow everything is extrapolated. The extended k- $\epsilon$  model and the k- $\omega$  model led to practically equal radial profiles. Notwithstanding this fact, the contours of  $P_t$  and tangential angle (the most significant quantities) are similar but not equal; the characteristic feature is that peaks are more smeared using the k- $\omega$  model, as a consequence of the much higher levels of turbulent viscosity. The equal values of the pitchwise integrals seem thus to indicate that there is a balance in the two models between profile losses and mixing losses, making the influence of  $\mu_t$  values somewhat small.

#### Bassi and Savini

<b>Code</b>	
<b>Test case</b>	DLR cascade
<b>Model description</b>	Wilcox standard k- $\omega$ model

#### Martelli

<b>Code</b>	FLOS3D
<b>Test case</b>	DLR cascade
<b>Model description</b>	Wilcox standard k- $\omega$ model

#### Shabbir, Zhu, and Celestina

<b>Code</b>	VSTAGE
<b>Test case</b>	Rotor 37
<b>Model description</b>	Two turbulence models are used: SKE (k- $\epsilon$ of Launder-Spalding, 1974), CKE (k- $\epsilon$ CMOTT of Shih et al., 1995) that avoids a local equilibrium assumption
<b>Boundary conditions and implementation</b>	Use of wall functions of Launder-Spalding (1974) if $y^+ > 25$ for the first mesh point. If $y^+ < 11$ , computation of the wall shear stress directly from the velocity profile, and use of wall functions of Shih and Lumley (1993).
<b>Transition model</b>	None
<b>Special wake treatment</b>	None

The radial distributions of  $P_o$ ,  $T_o$  and  $\alpha$  are greatly improved with the CKE model compared with the SKE model. The agreement with the experimental values is good between 10 and 70% of the blade span for the CKE model. The k- $\epsilon$  model produces an improved description of the wakes compared with Baldwin-Lomax's model. The two k- $\epsilon$  models give similar relative Mach number distributions in the wake for stations 3 and 4 at the three radial positions examined. The comparisons with the measurements are correct for station 4, but show the classical overprediction of the wake deficit in station 3. As the CKE model avoids the use of the local turbulent equilibrium, it could be assumed that it has some favourable effect on the prediction of the shock-boundary layer interaction. However, this modification has almost no effect on improving the tip leakage description. The losses are even higher in this region for the CKE model.

The two sets of boundary conditions do not show any modification of the results.

The SKE model is very sensitive to the upstream condition for  $\mu/\mu_t$ , while the CKE model shows almost no sensitivity to this parameter.

Shabbir et al. (1997) show a strong influence of the hub cavity on the blade suction side corner stall.

#### Ivanovic and Hutchinson

<b>Code</b>	TASCflow
<b>Test case</b>	Rotor 37
<b>Model description</b>	standard k- $\epsilon$ , with wall functions.
<b>Transition model</b>	None

The stagnation temperature shows a large decrease near the tip wall, with an increase of the efficiency. This behaviour is not shown by other contributors<sup>†</sup>.

#### Hildebrandt and Vogel

<b>Code</b>	TRACE-S, TASCflow
<b>Test case</b>	Rotor 37
<b>Model description</b>	standard k- $\epsilon$ , with wall functions
<b>Boundary conditions and implementation</b>	$20 < y^+ < 60$
<b>Solution strategy</b>	k- $\epsilon$ equations are uncoupled from the mean flow equations
<b>Transition model</b>	none

The higher wake dissipation observed in the simulation between stations 2 and 3 is certainly connected with the coarse mesh used in the downstream H zone.

From the blade-to-blade turbulent viscosity maps, high values of  $\mu/\mu_t$  are seen on the suction side wake ( $\approx 1200$ ) at mid-span. At 90% span, lower values are seen on the suction side ( $\approx 700$ ), but they increase on the pressure side near the trailing edge ( $\approx 300$ ). At mid-height near the trailing edge in station 3, the turbulent viscosity has a significant value only in the wake area. By contrast, at 90% span the flow feels the influence of the tip wall. The increase of the turbulent viscosity on the pressure side near the trailing edge may be the result of the accumulation of the tip leakage flow that crosses the blade passage from the suction side.

<sup>†</sup> but see footnote to Section 3.2.4.1

converged operating point as an initial guess for the next operating point. However, the approach largely eliminates dependence on the definition adopted for the residuals: for example, the effects of features such as the magnitude of the steps between iterations, residual smoothing and multigrids cancel out, though care is necessary if the solution is started on a coarse grid. Because of the differences between the definitions, it is not generally possible to compare absolute levels of convergence from different codes.

Targets for the drop in residuals are generally between 3 and 5 decades relative to the initial values for an arbitrary first guess. In addition, the iteration history of overall performance parameters such as inlet and exit mass flows and pressure ratio are usually monitored to ensure that the solution has reached a steady state, at least in engineering terms. This can be particularly important for compressor cases near stall, where the solution may be changing slowly but steadily.

### *3.7.1.1 Convergence Information For Contributed Solutions ADPAC (McNulty)*

- (a) Targets: Convergence is assessed by examining maximum and rms values of an unspecified residual. No target value has been quoted. In addition, the changes in inlet and exit mass flow and in either pressure ratio and efficiency (Rotor 37) or lift and loss coefficients and exit flow angle (DLR cascade) are monitored.
- (b) Rotor 37: The maximum and rms residuals dropped by about  $2\frac{1}{2}$  and 4 decades respectively after 400 iterations at the maximum efficiency condition for a solution started on a 4h grid (where h is the cell dimension for the finest grid). Plots of the iteration histories indicated that inlet and exit mass flows were constant and equal to plotting accuracy (about  $\pm 0.01\%$ ), and that pressure ratio and efficiency had changed by less than 0.002 and  $\pm 0.02\%$  respectively over the last 50 iterations. No convergence data were submitted for the near stall point.
- (c) DLR cascade: The maximum and rms residuals dropped by about  $2\frac{1}{2}$  and 4 decades respectively after 350 iterations for a solution started on a 4h grid. Plots of the iteration histories indicated that inlet and exit mass flows were equal to within about 0.1%; lift coefficient was constant to plotting accuracy, and loss coefficient and exit flow angle were dropping slowly at the rates of about 2% (of the current value) and  $0.1^\circ$  for 100 iterations.

### **Bassi/Savini**

- (a) Targets: A “stopping criterion” of 5 orders of magnitude decay for the rms of the time derivative of density is quoted, but Bassi and Savini (1992) suggest that three to four orders of magnitude is more typical.
- (b) DLR cascade: The convergence history was not recorded. It is stated that the first 3 orders of magnitude of residual decay was obtained using multigrid technique on the mean flow variables, then the code was run in single-grid mode.

### **CANARI (Couaillier)**

- (a) Targets: Convergence is assessed by examining maximum and rms residuals of each conservative variable. No target value has been quoted. In addition, the evolution of the mass flow rate at different axial sections of the computational domain, including the inlet and exit boundaries, is monitored.

- (b) Rotor 37: For the solution at the maximum efficiency condition using the mixing length turbulence model, the rms residuals for all five Navier-Stokes equations dropped by between 1.5 and 2 decades after 1500 iterations and then remained constant. Inlet and exit mass flow levels were constant after about 1000 iterations, but there was an increase in mass flow of about 0.5% between inlet and exit. No convergence data were submitted for the near stall point.

- (c) DLR cascade: For the solution using the mixing length turbulence model the rms residuals for all five Navier-Stokes equations dropped by between 2 and 2.5 decades after 1500 iterations and then remained constant. Inlet and exit mass flow levels were constant after about 1000 iterations, but there was an increase in mass flow of about 0.3% between inlet and exit.

### **Dadone/De Palma**

- (a) Targets: Convergence is assessed by examining the residual of the continuity equation. No target value has been quoted.
- (b) DLR cascade: It is stated that the residual of the continuity equation drops about 2 orders of magnitude in 12000 multigrid cycles. No plots of convergence history have been submitted.

### **EURANUS/TURBO (Kang and Hirsch)**

- (a) Targets: Convergence state is assessed by examining both density residuals and mass flow convergence histories. No target values are quoted.
- (b) Rotor 37: For the solution at the maximum efficiency condition, the density residual dropped by about 2 decades, and the inlet and exit mass flows were constant to within about 0.5% during the last quarter of the run. For the final solution there was a drop in mass flow of 0.39% between inlet and exit. No convergence data were submitted for the near stall point.

### **FLOS3D (Martelli)**

- (a) Targets: The residuals of all the equations, including the turbulence model if appropriate, are considered. Convergence is assumed when a drop in the residuals of 4 orders of magnitude is obtained relative to an arbitrary first guess with a linear pressure distribution between inlet and exit.
- (b) DLR Turbine: The residuals for all five flow equations dropped by between  $2\frac{1}{2}$  and 3 orders of magnitude within 1500 iterations and then remained constant.

### **HAH3D (Hah)**

- (a) Targets: The absolute values of the residuals of each finite difference equation are integrated over the entire computational domain. The solution is considered to be converged when the total integrated residuals of all the equations have been reduced by four orders of magnitude from the initial values, and the error in mass flow between inlet and exit is less than 0.01%.
- (b) Rotor 37: It is stated that the momentum equations and the turbulence transport equations reached the convergence criterion. No plots of convergence history have been submitted.
- (c) DLR cascade: It is stated that the momentum equations and the turbulence transport equations reached the convergence criterion. No plots of convergence history have been submitted.

**OVERFLOW** (Weber)

- (a) Targets: Convergence is assessed by considering the residuals for each grid, and also the histories of changes in mass flow, total pressure, total temperature and efficiency. A target of 3 decades drop is quoted for the residuals.
- (b) Rotor 37: The drop in residuals for the background H-grid did not quite reach 3 decades for the HO grid. This was attributed to the high number of interpolations for the hole boundary points around the embedded rotor blade and blade grid. A drop of about 3 decades was achieved for all grids in the H-O-H grid system.

**SWIFT/RVC3D** (Chima)

- (a) Targets: Convergence is assessed by examining maximum and rms values of the change in the variable for the continuity equation. A target of three decades drop is set. In addition, any changes in exit mass flow and total pressure and temperature should be only in the 4th digit, and the exit flow profiles should be converged to plotting accuracy.
- (b) Rotor 37: The maximum and rms residuals dropped by just under 2 and 2½ decades respectively at both the maximum efficiency and stall conditions. About 2000 iterations were needed for most operating points, but this increased to over 4000 near stall. Plots of the iteration histories of mean exit total pressure and temperature indicate constant conditions to plotting accuracy (about  $\pm 0.0005$  of the inlet values).
- (c) DLR cascade: The maximum and rms residuals dropped by about 3 and 3½ decades respectively after 2000 iterations. Plots of the iteration histories indicated that mass flow and total temperature were constant; mean exit total pressure was dropping slowly and reduced from 0.9792 to 0.9780 over the last 500 time steps (an increase of 5% in loss).

**TASCflow** (Hutchinson and Hildebrandt)

- (a) Targets: The time histories of the rms residuals of the U, V and P equations are considered. No target value has been quoted.
- (b) Rotor 37: For the solution with the 250K grid at 95% of the choke flow, the U residual drops by 2.2 decades, the V residual by 3.3 decades and the P residual by 3.7 decades. No histories of overall performance parameters have been submitted. No convergence data were submitted for the near stall point.
- (c) DLR cascade: No data currently submitted.

**TIP3D** (Denton)

- (a) Targets: The time histories of the rms residuals for the meridional momentum equation, the difference between inlet and exit mass flow, and the rms value of velocity are considered.
- (b) Rotor 37: For a solution at choked flow, the rms residuals drop by about 2.5 decades after 10000 steps and the maximum error in continuity is 0.5%.
- (c) DLR cascade: The rms residuals drop by about 2½ decades and the error in continuity is less than 0.1%.

**TRACE-S** (Lisiewicz, Vogel and Hildebrandt)

- (a) Targets: Convergence is assessed by examining the residual of the density (ie the change in the variable) and, for turbulent calculations, the residual of the square root of both turbulent quantities. The target for convergence is usually machine accuracy (ie maximum residual in density converged up to 6 magnitudes,

averaged residual converged up to 10 magnitudes, both relative to the maximum residual on time step zero).

- (b) Rotor 37: For the grid with 500K points, the maximum and rms density residuals dropped by about 5 decades in 3000 steps for the maximum flow point, when started from an initial guess with zero flow. The rms residuals for the k and ε equations in the turbulence model dropped by about 8 decades. Inlet and exit mass flows were essentially constant after 2000 steps and agreed to within 0.01%. No convergence data were submitted for the near stall point.
- (c) DLR cascade: The density residual appears to reach a limit of 4 decades drop after about 6500 time steps. Inlet and exit mass flows are constant and equal to within the plotting accuracy ( $\pm 0.02\%$ ) over the last 2500 time steps.

**TRAF3D** (Arnone and Marconcini)

- (a) Targets: Convergence is assessed by examining a residual defined as the vector sum of the changes in the five conservation variables, together with parameters such as inlet and exit absolute Mach number. For multigrid solutions the residual is based on the changes for the finest grid only. The target for convergence is stated as half an order above single precision machine accuracy.
- (b) Rotor 37: The rms residual dropped by just over 4 decades relative to the level after the first iteration in 300 multigrid cycles (including drops of about 0.5 decades when the grid was refined after 50 and 100 cycles). The maximum residual dropped by 3 decades, and the inlet and exit Mach numbers were constant to within about 0.001 over the last 100 cycles.

**TRANSCode** (Calvert and Stapleton)

- (a) Targets: Convergence is assessed by examining maximum and rms values of the imbalance in the axial momentum equation on the fine grid. A drop of two (and preferably three) decades is considered highly desirable. In addition, global flow quantities such as inlet mass flow and overall pressure ratio or loss should have reached steady values, and mass flow should be conserved to better than 0.5% at all quasi-orthogonal planes. Overall mass flow conservation (inlet to exit) should be better than 0.05%.
- (b) Rotor 37: At maximum efficiency, the maximum and rms residuals dropped by 3 and 3½ decades respectively, including a drop of about 1 decade due to applying heavy damping to the changes in turbulent viscosity and time step on the last 200 steps. Mass flow was conserved to 0.01% between inlet and exit, with a maximum error at any plane of 0.2%, and it was constant to within 0.005% over the last 200 steps. At the near stall operating condition, the drops in residuals were about 2½ decades, with similar values for the other parameters. No damping of turbulent viscosity was needed with the Spalart and Allmaras turbulence model.
- (c) DLR cascade: The maximum and rms residuals dropped by about 4 decades, including a drop of about 1 decade due to applying heavy damping to the changes in turbulent viscosity and time step on the last 500 steps. Mass flow was conserved to 0.002% between inlet and exit, with a maximum error at any plane of 0.03%, and it was constant to within 0.01% over the last 600 steps. No damping of turbulent viscosity was needed with the Spalart and Allmaras turbulence model.

### 3.6.4 Assessment of the models

The following conclusions may be derived about the influence of the turbulence model on the predicted results for the NASA 37 rotor:

- a) Most of the simulations that use Baldwin-Lomax's model produce very similar results (see Arnone's results), provided that enough nodes are used in the mesh.
- b) The mixing-length models can produce good results at mid-span. For Baldwin-Lomax's model, it is important to correct the original value of the constant  $C_{wk}$  from 0.25 to a value close to 1.0. This reduces the growth of an important separation zone on the suction side after the shock interaction.
- c) The mixing-length models give incorrect results for the tip leakage flow. This class of model has been derived for the description of wall boundary layers. The tip leakage flow is a configuration with many scales that are not directly linked to the local wall. The tip leakage flow is dominated by an almost inviscid supersonic jet, that meets the supersonic primary flow. At the boundary of the leakage jet, there is a shear layer that comes from the big difference of flow direction, starting at the suction side corner at the blade extremity. The scales that are associated with the leakage vortex ought to be linked with that shear layer.
- d) The turbulence models with two transport equations give improved results compared with the mixing length model. The improvement seems, however, to be rather marginal in a two-dimensional configuration, as shown by Chima with the  $k-\alpha$  model of Wilcox. This suggests that models with two equations are better able to deal with strongly three-dimensional turbulent wall flow.
- e) All simulations are unable to give a good prediction of the tip leakage flow area, although the  $k-\epsilon$  model performs a little better. It seems that the generation of loss is too high in this region, where there is a flow separation from the tip wall downstream of the passage shock. The value of the turbulent viscosity is also smaller than on the suction side at a lower radial position along the span. It may be that the interaction between the leakage vortex and the passage shock produces an incorrect reaction of the turbulence model. This is not surprising as most of the models have been calibrated for boundary layer flows, without strong three-dimensional effects of the leakage flow type.
- (f) The non-equilibrium  $k-\epsilon$  model (CMOTT), with wall law functions, and the low-Reynolds number  $k-\epsilon$  model give better results than the classical equilibrium model with wall law functions.
- g) It is difficult to deduce a firm conclusion from the results presented with the one-equation turbulence model (Spalart-Allmaras). Calvert and Couaillier obtained similar results, with the shock/boundary layer interaction being significantly over-estimated over the outer half of the span, leading to under-estimation of the pressure ratio and efficiency. Weber, with the model modified according to Dacles and Mariani (1995), achieved much better results using two different grid schemes. Both solutions match the test results closely between 40 and 90% span, and the solution on the overset O-H grid also matches the measurements nearer the hub.

For the DLR cascade, the conclusions are:

- a) Moving from algebraic to one-equation and two-equation models, the details of the flow field seem generally better captured, as they should be since more physics are included in the turbulence model, but sometimes the integral values computed with low level approximations are closer to the experimental data. As normally differential turbulence models require substantially more mass storage and CPU time than algebraic ones and lead to a more stiff system of equations, the question arises whether there is a pay-off for this increased complexity. The results presented here are far from giving a clear answer, but there is an impression that the good behaviour of a simple turbulence model in complex flows relies on the somehow lucky cancellation of opposing errors when an integration is performed.
- b) The surprising differences showed between computational results obtained with the same turbulence model can be reasonably ascribed mainly to their implementation and to the artificial smoothing properties of each solver associated with the grid construction. The conclusions that naturally stem are that the best way to analyze the relative performance of each model is to carry out extensive testing with a single type of code and/or computational mesh, and that detailed comparisons between the results from similar codes are an important aid to code developers.

## 3.7 CONVERGENCE CRITERIA

### 3.7.1 Convergence levels achieved

Convergence of a numerical scheme can mean either

- (i) that the solution to the finite difference equations approaches the true solution to the partial differential equations as the mesh is refined; or
- (ii) that the iterative process has been repeated until the magnitude of the difference between the function at the  $n+1$  and  $n$  iteration levels is as small as required at every grid point.

Definition (i) requires that the scheme is stable and consistent. The second definition is generally adopted when considering engineering applications of CFD and it is this "iteration convergence" which is considered here.

Ideally the criterion for convergence would be that the differences between successive iteration levels (usually termed residuals) should be reduced to the level implied by double precision machine accuracy, and it is highly desirable that codes are demonstrated to be capable of this for simple flows. However, this level of convergence is often not possible for more complex flows because of some local instability, which may be linked to a real physical phenomenon such as vortex shedding or due to a numerical feature. The "correct" response to such instabilities is to investigate them using a time-accurate method, but this is not practical with present computing resources.

Most practitioners therefore adopt more pragmatic measures to assess whether a solution is sufficiently converged to be useful. Typically, convergence is assumed to have occurred when the residuals have dropped to a given proportion of the levels at the start of the solution. This indicator has the disadvantage that it is dependent on the initial conditions assumed: an improvement to the accuracy of the first guess gives an apparent drop in the convergence level attained and this must be taken into account when using an already

**VSTAGE** (Shabbir/Zhu/Celestina)

- (a) Targets: Convergence is determined by monitoring the maximum and rms residuals of density. Typically a drop of two decades is needed. The global parameters, such as the mass flow at the inlet and exit planes, pressure ratio and efficiency, are also monitored to ensure that these have reached steady state values. The mass flow at the inlet and exit should match within 0.02%, and they should both remain constant to within 0.005% for the last few hundred iterations. Mass conservation at all planes is typically better than 0.5%.
- (b) Rotor 37: It is stated that the mass flow at the inlet and exit matched to within 0.017% and that both were constant to within 0.004% for the last 200 iterations at the high flow point ( $m/m_{\text{choke}} = 0.98$ ). No plots of convergence history have been submitted.

**3.7.2 Assessment of convergence parameters**

The convergence levels actually achieved for the WG 26 test cases did not reach the nominal targets for many of the solutions submitted (see Table 3.1). The levels achieved mainly ranged from 2 to 4 decades for both Rotor 37 and the DLR cascade. Little information was submitted for Rotor 37 at the near stall condition, but this tended to indicate slightly poorer levels of convergence than at points nearer choke. The iteration histories indicated that the solutions had, in most cases, reached sensibly constant conditions for the main overall performance parameters. A few of the contributors stated that they carried out additional investigations into whether more detailed aspects of the solution (such as the exit radial pressure and temperature profiles) were also constant, but no examples were submitted.

The best level of convergence submitted to the Working Group was for the TRACE-S solution of Rotor 37 at maximum flow (see Fig 3.41). This achieved drops of about 5 decades in the density residuals and of about 8 decades in the turbulence model equations for  $k$  and  $\epsilon$ . A more typical result is the TRANSCode solution for the DLR turbine cascade (Fig 3.42) where there is a drop of only about 2.5 decades, with a further improvement of one decade if heavy damping is applied to the values of turbulent viscosity calculated by the Baldwin-Lomax turbulence model. However, the overall performance parameters are completely steady and the maximum error in mass flow conservation at any plane is less than 0.03%.

To summarise, the convergence levels achieved for the WG 26 test cases generally fell short of the ideal. No time-accurate solutions were presented and it is not clear whether the limits reached were due to physical phenomena such as vortex shedding or to numerical features. However, most of the solutions were sensibly converged in terms of overall performance parameters, and they are probably typical of those generally produced for high-speed turbomachinery blade rows. Given this situation it is suggested that experienced operators are necessary for applying current CFD codes to turbomachinery and for assessing the adequacy of the results.

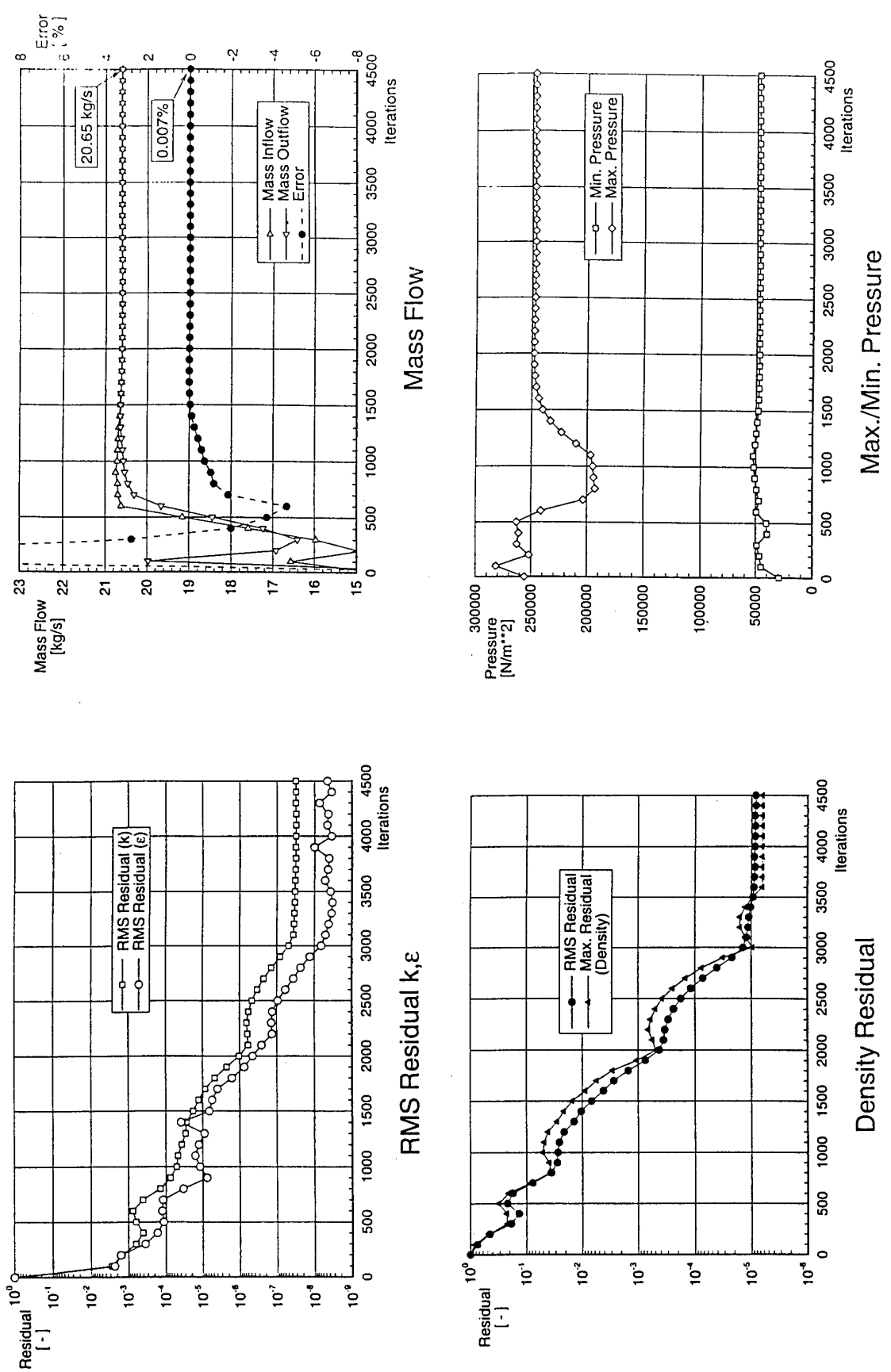


Fig 3.41 Convergence history for TRACE-S solution for Rotor 37 (Hildebrandt)

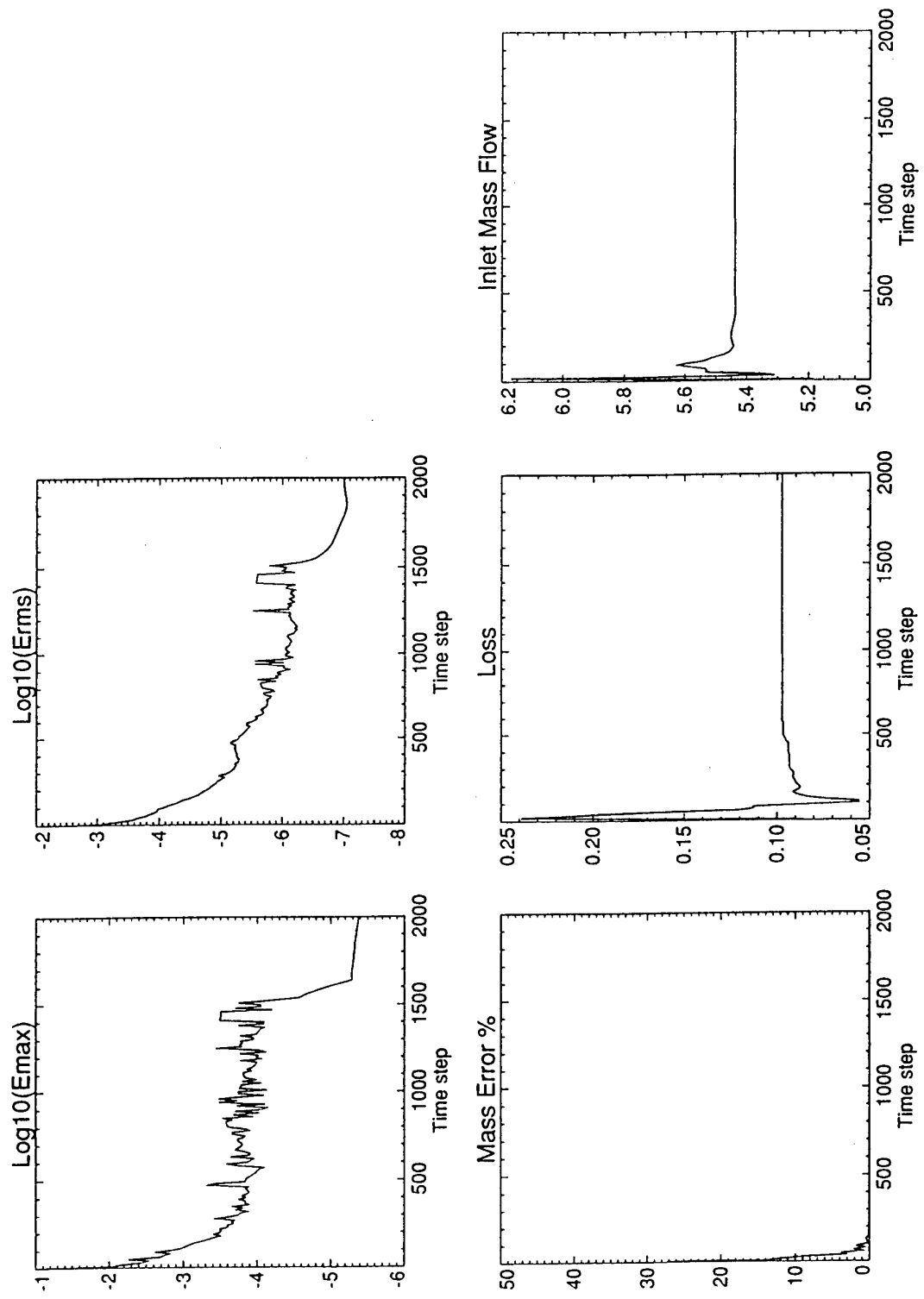


Fig 3.42 Convergence history for TRANSCODE solution for DLR cascade (Stapleton)

## Chapter 4

### CONCLUSIONS AND RECOMMENDATIONS

#### 4.1 CONCLUSIONS

Turbomachinery flows embody many complex physical phenomena, which Reynolds-averaged Navier-Stokes codes are able to predict to some extent. The key to improving the predictions is to understand the physical phenomena and the features of the codes which model them. Different aspects of the code are important, depending on the physical nature of the flows being predicted; it follows that what is best for predicting external flows around aircraft or for meteorological predictions may not be best for turbomachines. The two test cases studied in detail enabled the WG to assess the ability of CFD to predict several of the aerodynamic phenomena which dominate the performance of turbomachines. The Rotor 37 case included shock waves, corner stall, and tip clearance effects in a compressor rotor with supersonic inlet relative Mach number across the whole span. The DLR annular cascade showed the effect of spanwise pressure gradients on the complex secondary flow field. The test cases did not, on the other hand, include important transition effects, heat transfer, or high incidence conditions, nor of course the three-dimensional separations found within a centrifugal impeller. More importantly, the WG did not attempt to cover the difficult area of row-to-row interference due to unsteady flow.

In both cases, it proved difficult to clarify all the details of the flow from the measurements alone, but with the help of the CFD results a good understanding of all the flow fields was reached. The use of computer graphics to display streamlines in complex three dimensional flows was particularly helpful. The secondary flow in a turbine cascade has been well known for many years, but the complexities of the Rotor 37 flow have only now been illuminated by experiments and CFD studies conducted by NASA Lewis. This research was not specifically done for the WG, but the widespread international interest created by the ASME Turbomachinery Committee's exercise and now by the WG have spurred on NASA's research.

The overall performance of both test cases predicted by a wide range of CFD codes fell short of the accuracy engine designers need as a basis for decision-making. It is well known that designers "calibrate" the predictions of their current codes against the measured performance of their company's similar compressors and turbines; but CFD specialists obviously need to identify the reasons for the inaccuracies and so eliminate them.

#### 4.1.1 Rotor 37

The NASA Rotor 37 case was chosen by ASME in 1993 as a "blind" test case offered to the CFD community. Most codes predicted correctly the shape of the performance curves, but too high a pressure ratio, and too low an efficiency (Figs 3.1 and 3.2). The measurements suggest there is a corner stall which prevents the rotor achieving the predicted pressure ratio. The error in efficiency prediction, on the other hand, arises largely because the codes overestimate the tip clearance loss.

There is a shock wave at the rotor leading edge, and the predicted Mach number in the blade passage after it is

always too low. The ability to predict shock/boundary layer interaction correctly is the issue here. It has been shown that this result is sensitive to the local mass flow. Possibly, the local mass flow predicted by the codes and deduced from the experiments do not agree, either because the overall measured mass flow is wrong, or because inaccuracies in predicting the flow in the endwall regions has led to errors in the spanwise distribution of the flow, and hence an underestimate of the axial velocity around mid-span. A more detailed study of this question is suggested.

All the predictions supplied to ASME, although generally encouraging, failed to reproduce the hub corner stall suggested by the measurements, and nor did most of the more recent predictions supplied to the WG. This led NASA to make an important discovery: the flow in the hub region was seriously affected by the presence of a small axial gap (0.75 mm) in the hub annulus line just upstream of the rotor leading edge (because the hub wall ahead of that point did not rotate). Shabbir et al (1997) demonstrated by both measurements and computations that, although the gap led only to a blind cavity, air was pumped in and out of it as the rotor rotated. The presence of a shock wave even at the hub results in sufficiently large pitchwise static pressure changes to cause the pumping. Shabbir et al (1997) showed that CFD predictions in which the inflow-outflow was simulated predicted the corner stall, while the same code without the inflow-outflow did not. The important effect of the gap on the corner stall is a major discovery, but it came at a late stage of the WG's activities, and only one other member had time to try to model the gap-flow in his code. Only a few codes predicted a corner stall without modelling the flow in and out of the gap.

Fig 3.6 shows the corner stall, as predicted by one of the codes. It is evident that air is convected away from the hub in the separated region on the suction surface. The effect of the corner stall on the pitchwise-mean pressure distribution is a local depression in total pressure around 20% span, visible in Fig 3.3, a depression which most of the codes do not predict. Corner stall has been observed in many compressors, and there is no suggestion that it only arises when there is a gap or when the flow is transonic, although in this particular case the corner stall disappears at speeds below design speed (when the inlet relative velocity at the hub is subsonic). It has been postulated (Povinelli, 1997) that the interaction of the glancing shock wave from the rotor pressure surface with the hub boundary layer has some influence on the generation of secondary flow and the total pressure loss at the hub surface. This influence disappears at subsonic operating conditions.

One or two of the solutions supplied to the WG predicted the corner stall without simulating the gap. It is probably very sensitive to the mesh topology and/or the grid density as well as the turbulence model.

The flow pattern in the tip clearance region has been studied by Chima (1996b) and by Suder and Celestina (1996). They showed that the interaction between the overtip flow and the mainstream generated very high local shear, a region in which the axial velocity is reversed, and a region in which

the casing wall boundary layer is separated. This complex flow pattern proved too difficult for most turbulence models, which tended to predict too low a turbulent viscosity very near the wall, giving rise to the separation, and hence too high pressure losses in the outermost 5% of the span outside the casing boundary layer.

The blade wakes even in the quasi-two-dimensional region of the flow near mid-span are inaccurately predicted (Fig 3.15). Near the trailing edge they are too deep and narrow, but as they move downstream they dissipate too fast in some solutions, so that by the downstream traverse plane they are too shallow and too wide. This dissipation results from using too coarse a grid in that region, or a grid which is not aligned with the stream.

#### 4.1.2 DLR cascade

The overall pressure loss predicted by some of the codes was as much as 40% in error. The measurements of total pressure show that the secondary loss region near the hub is confined close to the wall by the spanwise static pressure gradient, and that the location of the peak loss is generally well predicted, though its magnitude varies very widely between the codes. The secondary loss region at the casing, on the other hand, is convected well away from the wall, the measured loss peak being at 55% span at the measurement plane (40% chord downstream). Most codes were unable to predict the location and magnitude of this peak. So it is clear that the codes are unable to predict correctly the highly three-dimensional secondary flow and the resulting migration of low energy fluid. Nevertheless, the solutions implementing turbulent transport models were generally closer to the experimental results than solutions implementing algebraic turbulence models, provided fine grids were used in the radial direction.

One code (TRACE-S) was run with the same turbulence model ( $k-\epsilon$ ) but two different grid topologies. Both the pressure losses and the flow angles changed appreciably, and exposed the difficulties introduced at the interface between an O-grid and an H-grid just behind the trailing edge.

#### 4.1.3 Choice of algorithms

The algorithms used for the WG were mostly of the time-marching type, but pressure correction methods were also represented. While the details of the algorithm must surely control the stability and convergence of the code as well as its running time, the WG has no evidence to suggest that it has any effect on the accuracy of the converged result.

#### 4.1.4 Grid construction

The desirable features of a computational grid are well known: it should be fine, have approximately square cells, and be aligned with the stream. Since these properties are impossible to achieve simultaneously in a turbomachine context, the choice of grid always represents a compromise between the various desirable properties of the grid and the complications introduced into the algorithms when complex mixed grid schemes are chosen. It is also known that the choice cannot be dissociated from the algorithm and the turbulence model. Nevertheless, some general conclusions are possible in the case of a structured grid. No unstructured grid solutions were offered to the WG.

In the present test cases, no single grid type stood out as being superior to the others. In general, the O- and C-grids proved better in the leading edge region, although the

present test cases, being at nearly zero incidence, were relatively insensitive to the leading edge region. In neither test case was it possible to measure the surface boundary layers, so the influence of the grid construction on profile loss could not be quantified.

At the trailing edge, the C-, I-, and H-grids that aligned with the wake provided the best wake definition. The O-grid solutions provided high resolution of the flow near the trailing edge but diffused the wake too rapidly as the grid opened up further downstream.

The most successful grids used by contributors were an H-I-H grid (because it aligned with the shock waves) (Fig 3.36) and an overset O-H grid (Fig 3.39), which avoids some of the problems which have been identified in other configurations. Both were applied to Rotor 37.

The grid lines must be clustered progressively near solid surfaces, and ought to be clustered in any regions of strong shear. All the solutions submitted used grids well clustered near surfaces. The total number of cells varied widely, with several contributors conducting grid refinement studies to establish how many cells were needed to make the solution grid-independent to engineering accuracy. The minimum number of cells must depend on the flow being computed, and the algorithm and turbulence model, so it is difficult to generalise. For examining localised flow features, such as leading edge separation bubbles, the grid must be locally refined. However, it became clear that in the cases used by the WG at least 50 grid lines hub-to-tip, around 50 blade-to-blade (if wall functions are used), and around 300,000 cells in all are needed if the pitchwise-mean performance is to be resolved. If wall functions are not used, a finer grid is needed near the walls. To capture the three-dimensional detail of the secondary flow vortices in the DLR cascade, more than 100 grid lines hub-to-tip may be needed. For overall performance and for blade surface pressure distributions, on the other hand, a grid of around 200,000 cells may be adequate.

However, the WG believes that having a large number of grid points (perhaps one million per row) is not necessarily sufficient to obtain an accurate solution. The turbulence model must also be adequate.

The “pinched tip” model of the tip clearance region chosen by some contributors is unsatisfactory, in that the actual clearance is not used; some empirical “effective” clearance is chosen instead, which may be dependent on the turbulence model. From the fully-gridded solutions submitted, which were in this Rotor 37 case just as inaccurate as the pinched tip solutions, the WG was unable to recommend a minimum number of cells within the clearance region. Some WG members suggested about ten, on the basis of other experience.

#### 4.1.5 Turbulence model

Turbulence models can broadly be divided into mixing length types (including the popular Baldwin-Lomax model) and turbulent convection types (including  $k-\epsilon$  models and one-equation models). Most of the Rotor 37 solutions contributed to the WG using the Baldwin-Lomax model produced very similar results, and they were generally inferior to the predictions obtained using turbulent convection models in those regions where the flow is separated or highly three-dimensional. It is logical that any turbulence model requiring a “distance to the nearest wall”

as a way of defining the shape of the whole boundary layer, and tuned to predict two-dimensional turbulent boundary layers, must encounter serious difficulties in such a region. Some turbulent transport models also use the "distance from the wall", but only to adjust the calculation within the laminar sub-layer, so that objection is no longer valid. The WG confirmed that the turbulent convection models used in the present study tended to give better solutions in separated flow regions than the mixing length models.

For flows which are subsonic and nearly two-dimensional, and where the viscous phenomena are primarily of the nature of a boundary layer, any of the well-known turbulence models are adequate, since they were set up for boundary layers. But the grid needs to be adequately fine near the walls. It is generally considered that for algebraic models a  $y^+$  value less than 5 is advisable unless wall functions are used; for codes in which the calculation extends fully to the wall using a low Reynolds number turbulence model a  $y^+$  value less than 1 is needed (and as low as 0.1 for heat transfer calculations), though no contributor used as low a value as that. In codes using wall functions,  $y^+ = 50$  seems adequate.

Massive differences were noted between the values of eddy viscosity predicted by different turbulence models. These differences, together with locally coarse grids in some solutions, led to differences in loss prediction which took some of the losses outside an acceptable range of accuracy. Some of the difference may result not from the modelling concept but from the way it is implemented within the particular code. Although most of the Baldwin-Lomax solutions for Rotor 37 were similar, this was not so for the DLR cascade solutions; and more generally solutions using nominally the same turbulence model did not always agree with each other.

The WG was unable to identify any one turbulence model which always gave good loss predictions. It is well known that this is an area of continuing vigorous research, and it needs to be.

Transition predictions were not thought to be important for the test cases chosen by the WG, but it is well known that many current CFD codes cannot predict transition or re-attachment satisfactorily. Predictions of the flow downstream of a leading edge separation bubble are in some applications critical to aerodynamic loss prediction. Transition prediction is also the key to good heat transfer prediction.

#### 4.1.6 Convergence

Code developers generally aim to reduce chosen residuals by around five decades, but in general the solutions contributed to the WG only achieved between two and three decades. Users also check that overall performance parameters have stabilised. It is not clear whether the inability of the codes to converge better is due to numerical problems (induced by the mesh topology near to the wall and in specific regions such as the leading and trailing edges) or whether it is the result of inadequate flow modelling (such as a turbulence model or the forcing of a steady solution to a flow field which is known to contain unsteady shed vortices). So experienced code users are needed to assess the adequacy of results.

#### 4.1.7 Working Group procedures

The key activity of the WG was to analyse and interpret the results of the computations. The full result of each

computation was several million numbers, far too large a data file to be circulated as a floppy disc or an e-mail. The WG therefore chose to start by examining the pitchwise-mean solutions at the traverse planes at which the measurements had been made. Those solutions were sent to one member, who plotted them together. However, the WG members who undertook the detailed analyses found that they needed selective plots of parameters, at other planes too. In retrospect, the establishment of a general data base of the selected results, which all members could access (using e-mail or perhaps by Internet) would have helped the WG.

#### 4.1.8 Closing remarks

The aim of the WG was to understand why current CFD codes are sometimes unable to predict the measurements made even on isolated turbomachine stages, and to clarify the role of the grids and turbulence models used in achieving good predictions. These are not simple questions to which a final answer could be expected, but the Group did throw light on several aspects of turbomachinery CFD, which may point research workers in the right direction for the future. The WG members most deeply involved in the analysis agreed how valuable the study had been to them. The improvement in the quality of the Rotor 37 predictions resulting from the ASME exercise, the subsequent NASA research and the WG activities is obvious. The experience of the WG has also provided a timely reminder that good quality detailed experimental measurements are essential to the continuing development of CFD.

### 4.2 RECOMMENDATIONS FOR RESEARCH

These recommendations apply both to code developers and code users.

1. Turbomachinery CFD should turn away from mixing length turbulence models and develop the use of turbulent transport models.
2. If losses are to be predicted, around 300,000 well-chosen grid points are needed per blade row, refined in regions of high aerodynamic shear.
3. If no wall function scheme is used, a finer grid is essential near the walls, and hence many more grid points.
4. If fuller details of the three-dimensional flow pattern are needed, a finer radial grid and hence 500,000 or more points in all are needed, depending on the turbulence model.
5. Some intensive research should be focused on tip clearance effects.
6. Computations allowing for full geometric details, leakage flows and annulus wall gaps should be more widely developed.
7. More use should be made of computer graphics to visualise complex three dimensional flows.
8. There is still a need for detailed experimental measurements as a basis for future developments in turbomachinery CFD, especially on multiple blade rows.

### 4.3 RECOMMENDATIONS TO PEP

1. Detailed experiments to provide test cases are very expensive. PEP should encourage international collaboration in devising and undertaking suitable experiments.
2. Similar studies should be undertaken, specifically on heat transfer predictions in turbomachines and later on combustor flows. Full use should be made

- of electronic data transfer facilities for conducting those studies.
3. In about five years' time, a Working Group should be set up to return to the turbomachinery CFD area, this time choosing test cases with more than one row, and focusing attention on the way steady codes can represent unsteady interference effects. By then, sufficient unsteady computations will be available.

## Appendix - List of Working Group members and contributors

<b>Panel members</b>		<b>Contributors of computations</b>	
Dr Georges Meauzé (chairman)	Fr	A.Arnone & A.Marconcini	R37
Prof Mike Bardon	Can	F.Bassi & M.Savini	DLR
Prof Charles Hirsch	Be	W.J.Calvert	R37
Keith Garwood	UK	M.Celestina	R37
Prof Francis Leboeuf	Fr	R.V.Chima	R37 DLR
Prof Jose J.Salva Monfort	Sp	V.Couaillier, G.Billonnet, C.Toussaint	R37 DLR
Prof Walter F.O'Brien	US	S.Dadone & P.de Palma	DLR
Dr.Eng.P.Psaroudakis	It	J.D.Denton	R37 DLR
Prof Giovanni Torella	It	C.Hah	R37 DLR
Prof Dr-Ing Heinrich Weyer	Ge	E.J.Hall	R37
		T.Hildebrandt	R37
<b>non-Panel members</b>		B.Hutchinson	R37
Prof Francesco Bassi	It	S.Kang & C.Hirsch	R37
W.John Calvert	UK	S.Lisiewicz	DLR
Dr Vincent Couaillier	Fr	F.Martelli	DLR
Dr Bob Delaney	US	S.McNulty	R37 DLR
Dr John Dunham (editor)	UK	A.Shabbir	R37
Prof W.G.Habashi	Ca	A.W.Stapleton	DLR
Prof Francesco Martelli	It	D.T.Vogel	R37
Dr Lou Povinelli	US	K.F.Weber	R37
Prof George K.Serovy	US		
Prof Ahmet S.Ücer	Tu		

### Authors of this Report

Preface, abstract, introduction	J.Dunham, G.Meauzé
Chapter 1	V.Couaillier, C.Hirsch, F.Leboeuf
Chapter 2	G.K.Serovy
Chapter 3	J.Dunham
Section 3.1	F.Leboeuf
Section 3.2	F.Bassi
Section 3.3	R.A.Delaney, L.A.Povinelli
Section 3.4	J.Dunham
Section 3.5	F.Leboeuf
Section 3.6	W.J.Calvert
Section 3.7	J.J.Salva
Table 3.1	R.A.Delaney
Table 3.2	W.F.O'Brien
Figs 3.1-5, 24-27	J.Dunham
Chapter 4	

### Addresses

Prof M. Bardon Royal Military College of Canada, Dept. of Mechanical Engineering, Kingston, Ontario K7K 5LO, Canada	Dr R.A.Delaney, E.J.Hall & K.F.Weber Advanced Turbomachinery Dept, Allison Engine Co., Speed Code T14A, P.O.Box 420, Indianapolis, Indiana 46206, USA
Prof F.Bassi Universitá di Ancona, Dipartimento di Energetica, Via Brecce Bianche, 60100 Ancona Italy	Prof J.D.Denton Whittle Laboratory, Cambridge University Engineering Dept., Madingley Rd, Cambridge CB3 0DY, England
Mr W.J.Calvert & Mr A.W.Stapleton DERA, Propulsion Dept., Pyestock, Farnborough, Hants, GU14 0LS, England	Dr P De Palma & Dr S.Dadone Istituto di Macchine ed Energetica, Politecnico di Bari, Via Re David 200, 70125 Bari, Italy
	Dr J.Dunham c/o DERA (see Calvert)

Mr K.R.Garwood  
 Rolls-Royce Ltd, Whittle House - WH23,  
 PO Box 3, Filton, Bristol BS12 7QE,  
 England

Prof W.G.Habashi  
 CFD Laboratory, Dept.of Mech.Engg., Concordia Univ.,  
 1455 de Maisonneuve Blvd.W., ER301, Montreal,  
 Quebec H3G 1M8,  
 Canada

Dr T.Hildebrandt  
 Universität der Bundeswehr München, Institut für  
 Strahltriebe, Werner Heisenberg-Weg 39,  
 D-85579 Neubiberg,  
 Germany

Prof Ch.Hirsch & Dr S.Kang  
 Vrije Universiteit Brussel, Dienst Stromingsmechanica,  
 Pleinlaan 2, 1050 Brussel,  
 Belgium

Dr B.R.Hutchinson  
 AEA Technology, Advanced Scientific Computing,  
 554 Parkside Drive,  
 Unit 4, Waterloo, Ontario,  
 Canada N2L 5Z4

Prof F.Leboeuf  
 Directeur Scientifique, Ecole Centrale de Lyon,  
 36 Avenue Guy de Collongue, 69131 Ecully Cedex,  
 France

Dr Eng F.Martelli & Prof A.Arnone  
 Universita degli Studi di Firenze, Dipartimento di Energetica,  
 via di Santa Marta 3, 60139 Firenze,  
 Italy

Mr S.McNulty (contributed calculations  
 done at Allison Engine Co.)  
 GE Aircraft Engines, One Neumann Way, MD A-411,  
 Cincinnati, OH 45215-1988,  
 USA

Dr G.Meauzé, Dr V. Couaillier, G. Billonnet, C. Toussaint  
 ONERA, BP 72, 92322 Chatillon Cedex,  
 France

Prof W.F.O'Brien  
 Dept of Mechanical Engineering, Virginia Polytechnic  
 Institute and State University, Room 100S, Randolph Hall,  
 Blacksburg, VA 24061,  
 USA

Dr L.A.Povinelli, Dr R.V.Chima, Dr C. Hah,  
 Dr J.J.Adamczyk, Dr M.Celestina, Dr M.Shabbir, & Dr J.Zhu  
 NASA Lewis Research Center, MS 5-3,  
 21000 Brookpark Rd, Cleveland, Ohio 44135,  
 USA

Dr.Eng P.Psaroudakis  
 Energetic Dept, University of Pisa, via Diotisalvi, 2, Pisa,  
 Italy

Prof J.J.Salva Monfort  
 Dpt. de Motopropulsion y, Termofluidodinamica ETSIA,  
 Plaza Cardenal Cisneros, 28040 Madrid,  
 Spain

Prof M.Savini  
 Università di Bergamo, Dalmine (BG)  
 Italy

Prof G.K.Serovy  
 2025 Black Engineering Building, Iowa State University,  
 Ames, Iowa 50011,  
 USA

Prof G.Torella  
 Accademia Aeronautica, Dipartimento di Scienze Applicate al  
 Volo, 80078 Pozzuoli (Napoli),  
 Italy

Prof A.S.Üçer  
 Dept of Mechanical Engineering, Middle East Technical  
 University, 06531 Ankara,  
 Turkey

Prof Dr-Ing H. Weyer & S.Lisiewicz & D.T.Vogel  
 Institut für Antriebstechnik, DLR, Postfach 90 60 58,  
 D-51140 Köln,  
 Germany

## References

- Adamczyk, J.J., Celestina, M., and Greitzer, E.M., 1993, "The role of tip clearance in high-speed fan stall", *Trans ASME, J. Turbomachinery*, Vol.115, p.28
- AGARD, 1976, "Through-flow calculations in axial turbomachinery", AGARD-CP-195
- AGARD, 1991, "CFD for propulsion applications", AGARD-CP-510
- AGARD, 1995, "Progress and challenges in CFD methods and algorithms", AGARD-CP-578
- Allmaras, S., 1992, "Contamination of laminar boundary layers by artificial dissipation in Navier-Stokes solutions", *Proc. Conf. on Numerical Methods in Fluid Dynamics*, ed. W.K. Morton, Reading, UK.
- Arnone, A., Liou, M., and Povinelli, L., 1993, "Multigrid calculations of three-dimensional viscous cascade flows", *J. Propulsion and Power*, vol. 9, p.605
- Arnone, A., 1994, "Viscous analysis of three-dimensional flows using a multigrid method", *J. Turbomachinery*, vol. 116, p.435
- Baldwin, B.S. and Lomax, H., 1978, "Thin-layer approximation and algebraic model for separated turbulent flows", AIAA Paper 78-257
- Bassi, F., Rebay, S., and Savini, M., 1991, "Transonic and supersonic inviscid computations in cascades using adaptative unstructured meshes", ASME Paper 91-GT-312
- Bassi,F. and Savini, M., 1992, "Secondary flows in a transonic cascade: validation of a 3D Navier-Stokes code", ASME Paper 92-GT-62
- Beam, R.M. and Warming, R.F., 1978, "An implicit factored scheme for the compressible Navier-Stokes equations", AIAA Jnl, vol. 16, p. 393
- Benetschik, H. and Gallus, H.E., 1992, "Inviscid and viscous transonic flows in cascades using an implicit upwind algorithm", *J. Propulsion and Power*, vol. 8, no 2
- Biswas, D. and Fukuyama, Y., 1994, "Calculation of transitional boundary layers with an improved low-Reynolds number version of the k- $\epsilon$  turbulence model", *J. Turbomachinery*, vol. 116, p.765
- Cahen, J., Couaillier, V., Delery, J., and Pot, Th., 1993, "Validation of a Navier-Stokes code using a k- $\epsilon$  turbulence model applied to a three-dimensional transonic channel", AIAA Paper 93-0293
- Calvert, W.J., Stapleton, A.W., Emmerson, P.R., Buchanan, C.R., and Nott, C.M., 1997, "Evaluation of a 3D viscous code for turbomachinery", ASME Paper 97-GT-78
- Cambier, L., Couaillier, V., and Veuillot, J.P., 1988, "Numerical solution of the Navier-Stokes equations by a multigrid method", *La Recherche Aérospatiale*, no. 1998-2, French and English Edition
- Cebeci, T. and Smith, A.M.O., 1974, "Analysis of turbulent boundary layers", Academic Press, New York
- Chen, G.T., Greitzer, E., Tan, C.S., and Marble, F.E., 1991, "Similarity analysis of compressor tip clearance flow structure", *ASME J. Turbomachinery*, vol 113, p.260
- Chen, J.P. and Whitfield, D.L., 1993, "Navier-Stokes calculations of the unsteady flowfield of turbomachinery", AIAA Paper 93-0676
- Chien, K.Y., 1982, "Predictions of channel and boundary layer flows with a low Reynolds number turbulence model", *AIAA Journal*, vol. 20, no.1, p33
- Chima, R.V., 1991, "Viscous three-dimensional calculations of transonic fan performance", AGARD-CP-510, Paper 21
- Chima, R.V., Giel, P.W. and Boyle, R.J., 1993, "An algebraic turbulence model for three-dimensional viscous flows", in *Engineering Turbulence Modelling and Experiments 2*, Rodi, W. and Martelli, F. (eds), Elsevier Pub., N.Y., p.775 [Also NASA TM-105931]
- Chima, R.V., 1996a, "A k- $\omega$  turbulence model for quasi-three-dimensional turbomachinery flow", NASA TM 107051
- Chima, R.V., 1996b, "Calculation of tip clearance effects in a transonic compressor rotor", ASME Paper 96-GT-114, accepted for publication in ASME Transactions
- Choi, D., 1993, "A Navier-Stokes analysis of film cooling in a turbine blade", AIAA Paper 93-0158
- Coakley, T.J., 1983, "Turbulence modeling methods for the compressible Navier-Stokes equations", AIAA Paper 83-1693
- Couaillier, V., Veysseire, Ph., and Vuillot, A.M., 1991, "3-D Navier-Stokes computations in transonic compressor bladings", *Proc. Xth ISABE Symposium*, ed. F.S. Billig, AIAA, Washington D.C.
- Couaillier, V., 1995, "CFD in turbomachinery for compressible flows. A state of the art review", First European Turbomachinery Conference, Erlangen
- Dacles-Mariani, J., Zilliac, G.G., Chow, J.S., and Bradshaw, P., 1995, "Numerical /Experimental study of a wingtip vortex in the near field", AIAA Jnl, vol.33, no.9
- Dailey, L.D., Jennions, I.K., and Orkwis, P.D., 1994, "Simulating laminar-turbulent transition with a low Reynolds number k- $\epsilon$  Navier-Stokes flow solver", AIAA Paper 94-0189
- Davis, R.L., Ni, R.H., and Carter, J.E., 1987, "Cascade viscous flow analysis using the Navier-Stokes equations", *Jnl Propulsion*, vol. 3, no.5, p.406
- Dawes, W.N., 1986, "A numerical method for the analysis of 3D viscous compressible flow in turbine cascades; application to secondary flow development in a cascade with and without dihedral", ASME Paper 86-GT-145
- Dawes, W.N., 1992, "The simulation of three-dimensional viscous flow in turbomachinery geometries using a solution-adaptative unstructured mesh methodology", *J. Turbomachinery*, vol.114, p.528
- Dawes, W.N., 1993, "The extension of a solution-adaptative three-dimensional Navier-Stokes solver toward geometries of arbitrary complexity", *J. Turbomachinery*, vol.115, p.283
- Denton, J.D., 1982, "An improved time marching method for turbomachinery flow calculations", in *Numerical Methods in Aeronautical Fluid Dynamics*, ed. P.L. Roe, Academic Press, London
- Denton, J.D., 1996, "Lessons from Rotor 37", 3rd ISAIF Meeting, Beijing

- Dorney, D. and Davis, R., 1991, "Navier-Stokes analysis of turbine blade heat transfer and performance", AGARD CP 510, [also Trans ASME, J. Turbomachinery, vol.114, p.795]
- Duchêne,C., 1995, "Etude numérique du refroidissement par film: phénomènes de base et application aux aubes de turbine", PhD Thesis, ISITEM, Nantes
- Engel, K. and Eulitz, F., 1994, "Numerical investigation of the rotor-stator interaction in a transonic compressor stage", AIAA Paper 94-2834
- ETMA, 1994, Proceedings of the Workshop on Turbulence Modeling for Compressible Flow Arising in Aeronautics, UMIST, Manchester, UK, to be published
- Fottner, L.(ed.), 1990, "Test cases for computation of internal flows in aero engine components", AGARD-AR-275
- Fougères, J.M. and Heider, R., 1994, "Three-dimensional Navier-Stokes prediction of heat transfer with film cooling", ASME Paper 94-GT-14
- Fourmaux, A. and Le Meur, A., 1987, "Computation of unsteady phenomena in transonic turbines and compressors", ONERA Report TP 131, ONERA, France
- Fourmaux, A., Billonnet, G., and Petot, B., 1993, "3D and 2.5D viscous flow computations for axial flow turbine blades", Proc. XIth ISABE Symposium, ed. F.S. Billig , AIAA, Washington D.C.
- Furukawa, M., Nakano, T., and Inoue, M., 1992, "Unsteady Navier-Stokes simulation of transonic cascade flow using an unfactored implicit upwind relaxation scheme with inner iterations", J. Turbomachinery, vol.114, p.599
- Gallus, H.E. and Bohn, D., 1976, "Multi-parameter approximation of calibrating values for multi-hole probes", Proc. Symposium on Measuring Techniques in Transonic and Supersonic Cascades and Turbomachines, Lausanne, p.31
- Giles, M.B., 1988, "Stator/rotor interaction in a transonic turbine", AIAA Paper 88-3093
- Gleize, V., 1994, "Calculation of a two dimensional transonic bump with a multiple-scale turbulence model", Proc. ETMA Worshop, UMIST, to be published
- Granville, P.S., 1987, "Baldwin-Lomax factors for turbulent boundary layers in pressure gradients", AIAA Jnl, vol.25, p.1624-1627
- Gregory-Smith, D.G. and Cleak, J.G.E., 1992, "Secondary flow measurements in a turbine cascade with high inlet turbulence", ASME J. Turbomachinery, vol.114, p.173
- Gregory-Smith, D.G., 1993, "The ERCOFTAC seminar and workshop on 3D turbomachinery flow prediction, December 1992", ASME Paper 93-GT-423
- Haase, W. *et al* (eds), 1993, *EUROVAL-A European initiative on validation of CFD Codes, notes on numerical fluid dynamics*, vol. 42, Vieweg Verlag
- Hah, C., 1984, "A Navier-Stokes analysis of three-dimensional turbulent flows inside turbine blade rows at design and off-design conditions", Trans ASME, J. Engineering for Gas Turbines and Power, vol.106, p.421
- Hah C., 1989, "Numerical study of three-dimensional flow and heat transfer near the endwall of a turbine blade row", AIAA Paper 89-1689
- Hah, C., and Reid, L., 1992, "A viscous flow study of shock-boundary layer interaction, radial transport, and wake development in a transonic compressor", J. Turbomachinery, vol.114, p.538
- Hah, C. and Loellbach, J., 1997, "Development of hub corner stall and its influence on the performance of axial compressor blade rows", ASME Paper 97-GT-42
- Harten, A., 1983, "High resolution schemes for hyperbolic conservation laws", J. Computational Physics, vol.49, p.357
- Hathaway, M.D., Chriss, R.M., Wood, J.R., and Strazisar, A.J., 1993, "Experimental and computational investigation of the nasa low-speed centrifugal compressor flow field", ASME J. Turbomachinery, vol.115, no.3, p.527
- Heider, R., Duboue, J.M., Petot, B., Couaillier, V., Liamis, N., and Billonnet, G., 1993, "Three-dimensional analysis of turbine rotor flow including tip clearance", ASME Paper 93-GT-111
- Hirsch, Ch. and Denton, J.D.(eds.), 1981, "Through flow calculations in axial turbomachines", AGARD-AR-175
- Hirsch, Ch., 1988, *Numerical Computation of Internal and External Flows, Vol. 1: Fundamentals of Numerical Discretization*, J. Wyley & Sons, Chichester
- Hirsch, Ch., 1990, *Numerical Computation of Internal and External Flows, Vol. 2: Computational Methods for Inviscid and Viscous Flows*, J. Wyley & Sons, Chichester
- Hirsch, Ch., 1994, "CFD methodology and validation for turbomachinery flows", AGARD-LS-195
- Holmes, D.G., Lamson, S.H., and Connell, 1988, "Quasi-3D solutions for transonic, inviscid flows by adaptative triangulation", ASME Paper 88-GT-83
- Horton, G.C., Harasgama, S.K., and Chana, K.S., 1991, "Prediction and measurements of 3d viscous flows in a transonic turbine nozzle guide vane row", AGARD-CP-510
- Ivanov, M.J., Kostoge, V.K., Krupa, V.G., and Nigmatullin, R.Z., 1993, "Design of high-load aviation turbomachines using modern 3D computational methods", Proc. XIth ISABE Symposium, ed. F.S. Billig, AIAA, Washington D.C.
- Jameson, A., Schmidt, W., and Turkel, E., 1981, "Numerical simulation of the Euler equations by finite volume method using Runge-Kutta time stepping schmes", AIAA Paper 81-1259
- Jameson, A., 1985, "Multigrid algorithms for compressible flow calculations", Lecture Notes in Mathematics, Proc. 2nd European Conf. on Multigrid Methods, Cologne, vol.1228, p.166
- Jennions, I.K. and Turner, M.G., 1993, "Three-dimensional Navier-Stokes computations of transonic fan flow using an explicit flow solver and an implicit k- $\epsilon$  solver", ASME J. Turbomachinery, vol.115, p.261
- Jones, W.P. and Launder, B.E., 1973, "The calculation of low-Reynolds-number phenomena with a two-equation model of turbulence", J. Heat and Mass Transfer, vol.16, p.1119
- Kang, S. and Hirsch, Ch., 1993, "Tip leakage flow in a linear compressor cascade", ASME Paper 93-GT-303
- Kunz, R.F. and Lakshminarayana, B., 1992, "Three-dimensional Navier-Stokes computation of turbomachinery flows using an explicit numerical procedure and a coupled k- $\epsilon$  model", ASME J. Turbomachinery, vol.114, p.627

- Kwon, O.J. and Hah, C., 1993, "Three-dimensional unstructured grid Euler method applied to turbine blades", AIAA Paper 93-0196
- Launder, B.E. and Spalding, D.B., 1974, "The numerical computation of turbulent flows", Comp. Math. Appl. Mech. Eng., Vol.3, p.269
- Lax, P.D. and Wendroff, B., 1964, "Difference schemes for hyperbolic equations with high order of accuracy", Comm. on Pure and Applied Mathematics, vol.17, p.381
- Lerat, A., 1979, "Une classe de schémas aux différences pour les systèmes hyperboliques de lois de conservation", Comptes rendus Acad. Sciences, Paris, Vol. A288, p.1033
- Lerat, A., Sidès, J., and Daru, V., 1982, "An implicit finite-volume method for solving the Euler equations", *Lecture Notes in Physics* 170, p.343
- Lerat, A. and Sidès, J., 1988, "Efficient solution of the steady Euler equations with a centered implicit method", in *Num. Meth. Fluid Dyn. III*, ed. K.W. Morton and M.J. Baines, Clarendon Press, Oxford, p.65
- Liamis, N. and Couaillier, V., 1994, "Unsteady Euler and Navier-Stokes flow simulations with an implicit Runge-Kutta method", Proc. 2nd European Comput. Fluid Dynamics Conf., Stuttgart, John Wiley & Sons
- Lien, F.S. and Leschziner, M.A., 1993, "Modelling shock/turbulent-boundary-layer interaction with second-moment closure within a pressure-velocity strategy", *Lecture Notes in Physics*, 414, ed. M.Napolitano and F. Sabetta, Springer-Verlag
- Liu, J.S., Sockol, P.M., and Prahl, J.M., 1988, "Navier-Stokes cascade analysis with a stiff k- $\epsilon$  turbulence solver", AIAA Paper 88-0594
- Liu, J.S. and Bozzola, R., 1993, "Three-dimensional Navier-Stokes analysis of the tip clearance flow in linear turbine cascades", AIAA Paper 93-0391
- MacCormack, R.W., 1969, "The effect of viscosity in hypervelocity impact cratering", AIAA Paper 69-354
- Madavan, N.K., Rai, M.M., and Gavali, S., 1989, "Grid refinement studies of turbine rotor-stator interaction", AIAA Paper 89-0325
- Madavan, N.K., Rai, M.M., and Gavali, S., 1993, "Multipassage three-dimensional Navier-Stokes simulation of turbine rotor-stator interaction", J. Propulsion and Power, vol.9, no.3, p.389
- Mathur, S.R., Madavan, R.N., and Rajagopalan, R.G., 1993, "A hybrid structured-unstructured method for unsteady turbomachinery flow computations", AIAA Paper 93-0387
- Matsuo, Y., 1991, "Computations of three-dimensional viscous flows flows in turbomachinery cascades", AIAA Paper 91-2237
- Mayle, R.E. Dullenkopf, K., and Schultz, A., 1997, "The turbulence that matters", ASME Paper 97-GT-274
- McNulty, G.S., Hall, E.J. and Delaney, R.A., 1994, "Preliminary findings in certification of ADPAC", AIAA Paper 94-2240
- Meauzé, G. (ed.), 1985, "3-D computation techniques applied to internal flows in propulsion systems", AGARD-LS-140
- Michel, R., Quémard, C., and Durant, R., 1969, "Application d'un schéma longueur de mélange à l'étude de couches limites turbulentes d'équilibre", ONERA NT no.154
- Moore, R.D. and Reid, L., 1980, "Performance of single-stage axial flow transonic compressor with rotor and stator aspect ratios of 1.19 and 1.26, respectively, and with design pressure ratio of 2.05", NASA TP 1659
- Moore, J. and Moore, J.G., 1991, "A computational study of tip leakage flow and losses in a linear turbine cascade", AGARD CP 510
- Nakahashi, K., Nozaki, O., Kikuchi, K., and Tamura, A., 1987, "Navier-Stokes computations of two- and three-dimensional cascade flow fields", AIAA Paper 87-1315
- Ni, R.H., 1982, "A multiple grid scheme for solving the Euler equations", AIAA Jnl, vol.20, p.1565
- Nozaki, O., Yamamoto, K., Kikuchi, K., Saito, Y., Sugahara, N., and Tamura, A., 1993, "Navier-Stokes computation of the three-dimensional flow-field through a transonic fan blade row", Proc. Xth ISABE Symposium, ed. F.S.Billig, AIAA, Washington D.C.
- Osher, S., 1982, "Shock modelling in aeronautics", in *Numerical Methods for Fluid Dynamics*, ed. K.W. Morton and M.J. Baines, Academic Press, London, p.179
- Patankar, S.V. and Spalding, D.B., 1972, "A calculation procedure for heat, mass and momentum transfer in three-dimensional parabolic flows", Int. Jnl Heat Mass Transfer, vol.15, p.1787
- Patel, V.C., Rodi, W., and Scheuerer, G., 1984, "Turbulence models for near-wall and low Reynolds number flows: a review", AIAA Jnl, vol.23, no.9, p.1308
- Perrin, G., Leboeuf, F. and Dawes, W.N., 1992, "Analysis of three-dimensional viscous flow in a supersonic axial flow compressor rotor, with emphasis on tip leakage flow", ASME Paper 92-GT-388
- Povinelli, L.A., 1997, "Current Lewis turbomachinery research: building on our legacy of excellence", Proc 13th ISABE Conference, Chattanooga
- Rai, M.M., 1989, "Three-dimensional Navier-Stokes simulations of turbine rotor-stator interaction; part i - methodology", J. Propulsion, vol.5, no.3, p.305
- Reid, L. and Moore, R.D., 1978, "Design and overall performance of four highly loaded, high-speed inlet stages for an advanced high-pressure-ratio core compressor", NASA TP 1337
- Roe, P.L., 1981, "Approximate Riemann solvers, parameter vectors and difference schemes", Jnl Computational Physics, vol.43, p.357
- Savill, M., 1993, "Further progress in the turbulence modelling of by-pass transition", in *Engineering Turbulence Modelling and Experiments*, ed. W. Rodi and F. Martelli, Elsevier Publ., p.583
- Scott, J.N. and Hankey, W.L., Jr, 1986, "Navier-Stokes solutions of unsteady flow in a compressor rotor", ASME J. Turbomachinery, vol. 108
- Schlechtriem, S. and Lötzerich, M., 1997, "Breakdown of tip leakage vortices in compressors at flow conditions close to stall", ASME Paper 97-GT-41
- Schödl, R., 1989, "Laser two-focus techniques", VKI Lecture Series 1989-05

- Serovsky, G.K.(ed.), 1976, "Modern prediction methods for turbomachine performance", AGARD-LS-83
- Shabbir, A., Zhu, J., and Celestina, M., 1996, "Assessment of three turbulence models in a compressor rotor", ASME Paper 96-GT-198
- Shabbir, A., Celestina, M.L., Adamczyk, J.J., and Strazisar, A.J., 1997, "The effect of hub leakage flow on two high speed axial flow compressor rotors", ASME Paper 97-GT-346
- Shih, T.H. and Lumley, J.L., 1993, "Kolmogorov behaviour of near-wall turbulence and its application in turbulence modelling", *Comp. Fluid Dyn.*, vol.1, p.43
- Shih, T.H., Liou, W.W., Shabbir, A., Zhu, J., and Yang, Z., 1995, "A new k- $\epsilon$  eddy viscosity model for high Reynolds number turbulent flows", *Computer Fluids*, vol. 24, 3, p.227
- Spalart, P.R. and Allmaras, S.R., 1992, "A one equation turbulence model for aerodynamic flows", AIAA Paper 92-0439
- Spalart, P.R. and Allmaras, S.R., 1994, "A one-equation turbulence model for aerodynamic flows", *La Recherche Aerospatiale*, 1994 no.1, p.5
- Steger, J.L. and Warming, R.F., 1981, "Flux vector splitting of the inviscid gas-dynamic equations with applications to finite difference methods", *J. Computational Physics*, vol.40, p.263
- Suder, K.L. and Celestina, M.L., 1996, "Experimental and computational investigation of the tip clearance flow in a transonic axial compressor rotor", ASME Paper 94-GT-365 [also ASME J. Turbomachinery, vol.118, no.2, p.218, 1996]
- Suder, K. L., Chima, R. V., Strazisar, A. J., and Roberts, W. B., 1995, "The effect of adding roughness and thickness to a transonic axial compressor rotor", *ASME J. Turbomachinery*, vol.117, no.4, p.491
- Suder, K.L., 1996, "Experimental investigation of the flow field in a transonic axial flow compressor with respect to the development of blockage and loss", NASA TM 107310
- Tran, L.T. and Taulbee, D.B., 1992, "Prediction of unsteady rotor-surface pressure and heat transfer from wake passings", *ASME J. Turbomachinery*, vol.114, p.807
- Trépanier, J.Y., Paraschivoiu, M., and Reggio, M., 1993, "euler computations of rotor-stator interaction in turbomachinery cascades using adaptative triangular meshes", AIAA Paper 93-0386
- Van Leer, B., 1982, "Flux vector splitting for the Euler Equations", Proc. 8th Conf. on Numerical Methods in Fluid Dynamics; *Lecture Notes in Physics*, vol.170, p.507, Springer Verlag.
- Veuillot, J.P. and Meauzé, G., 1985, "A 3D Euler method for internal transonic flow computations with a multi-domain approach", AGARD-LS-140
- Veuillot, J.P. and Cambier, L., 1990, "Computation techniques for the simulation of turbomachinery compressible flows", *Lecture Notes in Physics*, 371, ed. K.W. Morton, Springer-Verlag
- Vuillot, A.M., Couaillier, V., and Liamis, N., 1993, "3D turbomachinery Euler and Navier-Stokes calculations with multidomain cell-centered approach", AIAA Paper 93-2576
- Wegener, D., Le Meur, A., Billonnet, G., Escande, B., and Jourdren, C., 1992, "Comparison between two 3D-NS-codes and experiment on a turbine stator", AIAA Paper 92-3042
- Wilcox, D.C. and Rubesin, M.W., 1980, "Progress in turbulence modeling for complex flow fields including effects of compressibility", NASA Technical Paper 1517
- Wilcox, D.C., 1991, "Turbulence Modelling for CFD", DCW Industries Inc., La Cañada, California
- Wilcox, D.C., 1994, "Simulation of transition with a two-equation turbulence model", AIAA Jnl, vol.32, no.2, p.247
- Wisler, D.C., 1993, "CFD code assessment in turbomachinery - author's information package", unpublished ASME note
- Yee, H.C., 1987, "Construction of explicit and implicit symmetric tvd schemes and their applications", *J. Computational Physics*, vol.68, p.151
- York, B. and Knight, D., 1985, "Calculation of two-dimensional turbulent boundary layers using the Baldwin-Lomax model", AIAA Jnl, vol.23, p.1849
- Zimmermann, H., 1992, "Calculation of three-dimensional transonic turbine cascade flow", *J. Propulsion and Power*, vol.8, no.2, p.382

REPORT DOCUMENTATION PAGE				
<b>1. Recipient's Reference</b>	<b>2. Originator's Reference</b>	<b>3. Further Reference</b>	<b>4. Security Classification of Document</b>	
	AGARD-AR-355	ISBN 92-836-1075-X	UNCLASSIFIED/ UNLIMITED	
<b>5. Originator</b>	Advisory Group for Aerospace Research and Development North Atlantic Treaty Organization 7 rue Ancelle, 92200 Neuilly-sur-Seine, France			
<b>6. Title</b>	CFD Validation for Propulsion System Components			
<b>7. Presented at/sponsored by</b>	The PEP Working Group 26			
<b>8. Author(s)/Editor(s)</b>	Multiple		<b>9. Date</b>	May 1998
<b>10. Author's/Editor's Address</b>	Multiple		<b>11. Pages</b>	96
<b>12. Distribution Statement</b>	There are no restrictions on the distribution of this document. Information about the availability of this and other AGARD unclassified publications is given on the back cover.			
<b>13. Keywords/Descriptors</b>	Aircraft engines Gas turbine engines Design Computerized simulation Performance Reliability Gas flow Computational fluid dynamics Coding Navier-Stokes equations Validity Turbomachinery Computation Turbulence Mathematical models Predictions Aerodynamics Axial flow compressors Axial flow turbines			
<b>14. Abstract</b>	<p>Computer codes which solve the Reynolds-averaged Navier-Stokes equations are now used by manufacturers to design turbomachines, but there is no consensus about which grids and which turbulence models are good enough to provide a reliable basis for design decisions. The AGARD Propulsion and Energetics Panel set up Working Group 26 to help to clarify these issues, by analysing predictions (using as wide a range of codes as possible) of two representative but difficult single blade row test cases: NASA Rotor 37 and an annular turbine cascade tested by DLR. This report presents the Group's results and conclusions.</p> <p>Recommendations are made about the type and density of grid, which depend on many factors. Mixing-length turbulence models are unsuitable for turbomachines with their complex endwall flows; some kind of turbulent transport model is essential. No turbulence model was found which always gave good loss predictions.</p>			

**AGARD**



7 RUE ANCELLE • 92200 NEUILLY-SUR-SEINE

FRANCE

Télécopie 0(1)55.61.22.99 • Télex 610 176

## DIFFUSION DES PUBLICATIONS

### AGARD NON CLASSIFIEES

L'AGARD détient un stock limité de certaines de ses publications récentes. Celles-ci pourront éventuellement être obtenus sous forme de copie papier. Pour de plus amples renseignements concernant l'achat de ces ouvrages, adressez-vous à l'AGARD par lettre ou par télecopie à l'adresse indiquée ci-dessus. *Veuillez ne pas téléphoner.*

Des exemplaires supplémentaires peuvent parfois être obtenus auprès des centres de diffusion nationaux indiqués ci-dessous. Si vous souhaitez recevoir toutes les publications de l'AGARD, ou simplement celles qui concernent certains Panels, vous pouvez demander d'être inclus sur la liste d'envoi de l'un de ces centres.

Les publications de l'AGARD sont en vente auprès des agences de vente indiquées ci-dessous, sous forme de photocopie ou de microfiche. Certains originaux peuvent également être obtenus auprès de CASI.

## CENTRES DE DIFFUSION NATIONAUX

### ALLEMAGNE

Fachinformationszentrum Karlsruhe  
D-76344 Eggenstein-Leopoldshafen 2

### BELGIQUE

Coordonnateur AGARD - VSL  
Etat-major de la Force aérienne  
Quartier Reine Elisabeth  
Rue d'Evere, B-1140 Bruxelles

### CANADA

Directeur - Gestion de l'information  
(Recherche et développement) - DRDG 3  
Ministère de la Défense nationale  
Ottawa, Ontario K1A 0K2

### DANEMARK

Danish Defence Research Establishment  
Ryvangs Allé 1  
P.O. Box 2715  
DK-2100 Copenhagen Ø

### ESPAGNE

INTA (AGARD Publications)  
Carretera de Torrejón a Ajalvir, Pk.4  
28850 Torrejón de Ardoz - Madrid

### ETATS-UNIS

NASA Center for AeroSpace Information (CASI)  
Parkway Center, 7121 Standard Drive  
Hanover, MD 21076

### FRANCE

O.N.E.R.A. (Direction)  
29, Avenue de la Division Leclerc  
92322 Châtillon Cedex

### GRECE

Hellenic Air Force  
Air War College  
Scientific and Technical Library  
Dekelia Air Force Base  
Dekelia, Athens TGA 1010

### ISLANDE

Director of Aviation  
c/o Flugrad  
Reykjavik

### ITALIE

Aeronautica Militare  
Ufficio Stralcio AGARD  
Aeroporto Pratica di Mare  
00040 Pomezia (Roma)

### LUXEMBOURG

Voir Belgique

### NORVEGE

Norwegian Defence Research Establishment  
Attn: Biblioteket  
P.O. Box 25  
N-2007 Kjeller

### PAYS-BAS

Netherlands Delegation to AGARD  
National Aerospace Laboratory NLR  
P.O. Box 90502  
1006 BM Amsterdam

### PORTRUGAL

Estado Maior da Força Aérea  
SDFA - Centro de Documentação  
Alfragide  
P-2720 Amadora

### ROYAUME-UNI

Defence Research Information Centre  
Kentigern House  
65 Brown Street  
Glasgow G2 8EX

### TURQUIE

Millî Savunma Başkanlığı (MSB)  
ARGE Dairesi Başkanlığı (MSB)  
06650 Bakanlıklar - Ankara

## AGENCES DE VENTE

### NASA Center for AeroSpace Information (CASI)

Parkway Center, 7121 Standard Drive  
Hanover, MD 21076  
Etats-Unis

### The British Library Document Supply Division

Boston Spa, Wetherby  
West Yorkshire LS23 7BQ  
Royaume-Uni

Les demandes de microfiches ou de photocopies de documents AGARD (y compris les demandes faites auprès du CASI) doivent comporter la dénomination AGARD, ainsi que le numéro de série d'AGARD (par exemple AGARD-AG-315). Des informations analogues, telles que le titre et la date de publication sont souhaitables. Veuillez noter qu'il y a lieu de spécifier AGARD-R-nnn et AGARD-AR-nnn lors de la commande des rapports AGARD et des rapports consultatifs AGARD respectivement. Des références bibliographiques complètes ainsi que des résumés des publications AGARD figurent dans les journaux suivants:

### Scientific and Technical Aerospace Reports (STAR)

STAR peut être consulté en ligne au localisateur de ressources uniformes (URL) suivant:  
<http://www.sti.nasa.gov/Pubs/star/Star.html>  
STAR est édité par CASI dans le cadre du programme NASA d'information scientifique et technique (STI)  
STI Program Office, MS 157A  
NASA Langley Research Center  
Hampton, Virginia 23681-0001  
Etats-Unis

### Government Reports Announcements & Index (GRA&I)

publié par le National Technical Information Service  
Springfield  
Virginia 2216  
Etats-Unis  
(accessible également en mode interactif dans la base de données bibliographiques en ligne du NTIS, et sur CD-ROM)



Imprimé par le Groupe Communication Canada Inc.

(membre de la Corporation St-Joseph)

45, boul. Sacré-Cœur, Hull (Québec), Canada K1A 0S7

**AGARD**

NATO OTAN

7 RUE ANCELLE • 92200 NEUILLY-SUR-SEINE

FRANCE

Telefax 0(1)55.61.22.99 • Telex 610 176

AGARD holds limited quantities of some of its recent publications, and these may be available for purchase in hard copy form. For more information, write or send a telefax to the address given above. *Please do not telephone.*

Further copies are sometimes available from the National Distribution Centres listed below. If you wish to receive all AGARD publications, or just those relating to one or more specific AGARD Panels, they may be willing to include you (or your organisation) in their distribution.

AGARD publications may be purchased from the Sales Agencies listed below, in photocopy or microfiche form. Original copies of some publications may be available from CASI.

## DISTRIBUTION OF UNCLASSIFIED

### AGARD PUBLICATIONS

#### NATIONAL DISTRIBUTION CENTRES

##### BELGIUM

Coordonnateur AGARD - VSL  
Etat-major de la Force aérienne  
Quartier Reine Elisabeth  
Rue d'Evere, B-1140 Bruxelles

##### CANADA

Director Research & Development  
Information Management - DRDIM 3  
Dept of National Defence  
Ottawa, Ontario K1A 0K2

##### DENMARK

Danish Defence Research Establishment  
Ryvangs Allé 1  
P.O. Box 2715  
DK-2100 Copenhagen Ø

##### FRANCE

O.N.E.R.A. (Direction)  
29 Avenue de la Division Leclerc  
92322 Châtillon Cedex

##### GERMANY

Fachinformationszentrum Karlsruhe  
D-76344 Eggenstein-Leopoldshafen 2

##### GREECE

Hellenic Air Force  
Air War College  
Scientific and Technical Library  
Dekelia Air Force Base  
Dekelia, Athens TGA 1010

##### ICELAND

Director of Aviation  
c/o Flugrad  
Reykjavik

##### ITALY

Aeronautica Militare  
Ufficio Stralcio AGARD  
Aeroporto Pratica di Mare  
00040 Pomezia (Roma)

##### LUXEMBOURG

See Belgium

##### NETHERLANDS

Netherlands Delegation to AGARD  
National Aerospace Laboratory, NLR  
P.O. Box 90502  
1006 BM Amsterdam

##### NORWAY

Norwegian Defence Research Establishment  
Attn: Biblioteket  
P.O. Box 25  
N-2007 Kjeller

##### PORUGAL

Estado Maior da Força Aérea  
SDFA - Centro de Documentação  
Alfragide  
P-2720 Amadora

##### SPAIN

INTA (AGARD Publications)  
Carretera de Torrejón a Ajalvir, Pk.4  
28850 Torrejón de Ardoz - Madrid

##### TURKEY

Millî Savunma Başkanlığı (MSB)  
ARGE Dairesi Başkanlığı (MSB)  
06650 Bakanlıklar - Ankara

##### UNITED KINGDOM

Defence Research Information Centre  
Kentigern House  
65 Brown Street  
Glasgow G2 8EX

##### UNITED STATES

NASA Center for AeroSpace Information (CASI)  
Parkway Center, 7121 Standard Drive  
Hanover, MD 21076

#### SALES AGENCIES

##### NASA Center for AeroSpace Information (CASI)

Parkway Center, 7121 Standard Drive  
Hanover, MD 21076  
United States

##### The British Library Document Supply Centre

Boston Spa, Wetherby  
West Yorkshire LS23 7BQ  
United Kingdom

Requests for microfiches or photocopies of AGARD documents (including requests to CASI) should include the word 'AGARD' and the AGARD serial number (for example AGARD-AG-315). Collateral information such as title and publication date is desirable. Note that AGARD Reports and Advisory Reports should be specified as AGARD-R-nnn and AGARD-AR-nnn, respectively. Full bibliographical references and abstracts of AGARD publications are given in the following journals:

##### Scientific and Technical Aerospace Reports (STAR)

STAR is available on-line at the following uniform resource locator:

<http://www.sti.nasa.gov/Pubs/star/Star.html>

STAR is published by CASI for the NASA Scientific and Technical Information (STI) Program

STI Program Office, MS 157A

NASA Langley Research Center  
Hampton, Virginia 23681-0001

United States

##### Government Reports Announcements & Index (GRA&I)

published by the National Technical Information Service  
Springfield  
Virginia 22161  
United States  
(also available online in the NTIS Bibliographic Database or on CD-ROM)



Printed by Canada Communication Group Inc.

(A St. Joseph Corporation Company)

45 Sacré-Cœur Blvd., Hull (Québec), Canada K1A 0S7